



Habilitation Thesis

**Optical Methods
in Experimental Mechanics of Solids**

Prof.dr.ing. Mircea Cristian DUDESCU
Faculty of Mechanical Engineering
The Technical University of Cluj-Napoca

2015

Acknowledgments

This research work has been carried out during the years 2001–2015 mostly in the Department of Mechanical Engineering (former Chair of Strength of Materials) of the Technical University of Cluj-Napoca, where I work as member of the academic staff. An important part was achieved abroad while the two fellowships in Germany lasting almost four years in the university and industrial environment.

This work is dedicated to my mentor and PhD tutor, the regretted Professor Ioan PASTRAV who passed away this year. Professor PASTRAV was a dedicated promoter of the optical methods of experimental solid mechanics and the founder of the Optical Methods in Experimental Mechanics Laboratory at the TUC-N. Thanks to him I have discovered the fascinating world of experimental mechanics and I still continue to dedicate my research activity to this interesting field.

Without the competence and passion of some outstanding professors and specialists from the industry, from whom I decoded and learned the “secrets” of this field, this work would not have existed. I want to thank to all of these. Especially, I want to express my gratitude to Prof.Dr.-Ing. Jochen Naumann, PD.Dr.-Ing. Martin Stockmann from the Chemnitz University of Technology and Dr. Hans-Reinhard Schubach from Dr. Ettemeyer GmbH (timely Dantec Dynamics GmbH) from Germany, who made my entrance into the world of new experimental techniques and optical methods of electronic speckle pattern interferometry in particularly possible by their trust and professionalism.

I would like to thank to all the colleagues from the formerly Chair of Strength of Materials (actually part of Department of Mechanical Engineering) for their long time support, collaboration and friendship.

Last but not least, I would like to thank to my family for their support and understanding.

Cluj-Napoca, May 2015

Table of Contents

a. ABSTRACT	3
b. ACHIEVEMENTS AND DEVELOPMENT PLANS	7
b-i. RESEARCH ACHIEVEMENTS.....	7
1. RESEARCH DIRECTIONS AND COMPETENCES.....	7
2. OPTICAL METHODS IN EXPERIMENTAL MECHANICS	13
2.1. Context of experimental mechanics	13
2.2. Photoelasticity	16
2.2.1. Introduction.....	16
2.2.2. Application of photoelasticity to thin-wall structures	20
2.3. Moiré methods	25
2.3.2. Introduction.....	25
2.3.2. Shadow moiré principle.....	26
2.3.3. Shadow moiré by phase shifting method.....	29
2.3.4. Membranes analysis by shadow moiré technique	32
2.3.5. Study by shadow moiré method of prismatic bars subjected to torsion	34
2.4. Electronic Speckle Pattern Interferometry (ESPI)	37
2.4.1. Introduction.....	37
2.4.2. Electronic Speckle Pattern Interferometry principle	39
2.4.3. Phase shifting technique. Quantitative evaluation of interferograms	41
2.4.4. Contour measurement.....	43
2.4.5. Applications of ESPI in material characterization.....	44
2.5. Digital Image Correlation.....	67
2.5.1. Introduction.....	67
2.5.2. Two-dimensional Digital Image Correlation principle.....	68
2.5.3. Three-dimensional DIC	71
2.5.4. Applications of DIC in material characterization.....	75
2.6. Matlab Scientific Toolbox for Strain-Stress Analysis.....	93
2.6.1. Introduction.....	93
2.6.2. MATLAB Graphical User Interface.....	94
2.6.3. Toolbox modules and computation algorithms	97
2.6.4. Applications in experimental mechanics.....	101
b-ii. DIDACTIC SKILLS AND PROFESSIONAL ACHIEVEMENTS.....	109
b-iii. FUTURE SCIENTIFIC, PROFESSIONAL AND ACADEMIC DEVELOPMENT PLAN	111
b-iv. REFERENCES.....	113

a. ABSTRACT

The habilitation thesis presents the scientific achievements of the author, undertaken in the period of 2001 and 2015 in the field of optical methods in experimental mechanics of solids. During the above mentioned period, the research and professional interests of the author of this thesis, have been focused mainly on implementation of new applications and improving of experimental techniques in mechanics of materials and other connected fields. The researches include near experimental techniques and also numerous validations by analytical and numerical (Finite Element) methods.

Beginning with the PhD thesis (1996-2000) and continuing more than one decade the research and also the didactic activities required to apply and deeply understand the numerous experimental techniques such as: strain gages, photoelasticity, geometric moiré, interferometric moiré, electronic speckle pattern interferometry (ESPI), optical metrology, digital image correlation (DIC), thermoelasticity, non-destructive testing (NDT) and microindentation. All these methods are interdisciplinary and interact with topics like physics, optics, image processing, materials, fabrication processes, etc. The possibilities of direct measure are nowadays extremely rare and to measure implies besides manipulation of complex measuring systems, understanding of measurand and limit of application of measurement method.

Stress analysis has been considered for some time as a distinct professional branch of engineering, the main objective to determine and improve the mechanical strength of elements, structures and machines. Experimental stress analysis strives to achieve these aims by experimental means. In the investigation of problems of mechanical strength, many factors make the experimental approach indispensable, and often the only means of access. In addition to this, theoretical considerations are usually based on simplifying assumptions which imply certain deviations from reality, and it can be established only by experimentation whether such idealization do not produce an undue distortion of the problem. Using experimental stress analysis is required especially if the analysis is done under real service conditions, where there are all the influential factors such properties of the employed materials, the methods of manufacture and the operation conditions. A special place among the experimental techniques is occupied by optical methods. Among their numerous possible applications, they can help the researcher to characterize the materials' behaviour, to give access to the time-evolution of fields of data at different scales and maybe, the most important advantage, they are non-contact and provide full-field data that are naturally suitable for direct comparison with numerical solutions.

The habilitation thesis is structured in three sections, one presents the main achievements in the field of optical methods of experimental mechanics, and the second one provides aspects regarding didactic skills and professional achievements and the last one sketches the proposed future scientific, professional and academic development plan.

The first section, *Achievements and development plan*, details briefly the research directions and mentions the main articles indexed in Web of Science, Scopus and Google Scholar databases. The author's research activities can be fitted in the following four main fields: experimental methods in solid mechanics, material testing and characterization, structural analysis and numerical simulation of MEMS and biomedical engineering. Only the contributions

connected with the field of optical methods are presented in the thesis even though the other research directions have also relevant articles and achievements.

Optical methods of experimental mechanics of solids described in this thesis are the most applied in the research and industry. The thesis presents in the first chapter 2.1 the general context of experimental techniques, trends and future perspectives.

Second chapter 2.2 is dedicated to *photoelasticity* and presents besides a short introduction of the technique a study of flexible shells of revolution by three dimensional photoelasticity. Application of measurement method to thin wall structures was less presented in the literature, an important advantage of the method is displaying the full field stress distribution that can be directly compared with numerical simulations. Main results and limitations of the measurement method are presented through studies of bellows subjected to axial loading and influence of the model weight in case of photoelastic analysis.

Chapter 2.3 is dedicated to optical method of geometric moiré and its particular set-up called *shadow moiré*. The author applied the method to solve a research contract for young researchers (type AT - CNCSIS) which has investigated large deformations of pressurized membranes by analytical, numerical and experimental methods. The sensitivity of standard shadow moiré method used for contour determination of the objects is relatively reduced and it is mainly influenced by the pitch of the master grid. The chapter presents application of the phase shifting procedure that brings a significant improvement of the measurement precision and sensitivity, the method's accuracy comparatively with the classical shadow moiré will increase up to ten times. Successful implementation of the methods led also to solution of torsion problem of bars with arbitrarily cross sections using membrane analogy.

Chapter 2.4 presents the method of *electronic speckle pattern interferometry* (ESPI). ESPI is an optical measuring technique that allows rapid and highly accurate measurement of deformations. In comparison with other techniques for strain measurement or calculation, the ESPI enjoys the advantages of being non-contact, full-field, has a high spatial resolution, high sensitivity, delivers accurate displacement data and does not require any calibration or costly surface preparation. The method has been employed by the author over many years spent mostly abroad, starting within a Marie-Curie research fellowship (2001-2003) in a German company that produces optical measurements systems based on ESPI and followed at Chemnitz University of Technology, Germany, Department of Experimental Mechanics (2005-2006) as an Alexander von Humboldt Foundation fellow. Since then there were published one book and several papers in the proceedings of international conferences or journals, among them being the most cited paper of the author. As the main contributions there are presented applications of ESPI in material characterization namely characterization of thermal expansion coefficient of isotropic and anisotropic materials and investigation of non-linear springback for high strength steel sheets. Both studies provide practical importance and contain new measurement concepts and methodologies.

Chapter 2.5 presents an optical method that has had a major impact in the field of mechanics of solids and structures and it is still undergoing very interesting developments, called *digital image correlation* (DIC). A specific advantage of this tool is that it exploits numerical images that are usually acquired by optical means. Comparatively with other optical techniques to measure displacements where light modulation produces fringe patterns and these patterns contain phase information that can be decoded, in DIC displacements there are directly obtained from point trajectories. The chapter analyses the concepts of two and three-dimensional DIC and presents numerous applications: measurement of flexural modulus of wood beams, materials curves and constants determination, investigation of polymers

mechanical behaviour and with insights of the non-uniform strain behaviour of these materials in the yield and post-yield regimes, measurement methodology and accuracy of coefficient of thermal expansion determination using a 3D digital image correlation system for plastics and analysis of thermal sensors at micro and micro-scale.

Chapter 2.6 presents the results achieved within a research grant (Marie-Curie European Reintegration Grant FP6) entitled *MATLAB Scientific Toolbox for Strain-Stress Analysis*. To complete a complex strain-stress investigation using optical methods sophisticated equipment controlled by dedicated computer software is needed. Interaction of the researcher in the measuring process or data manipulation is in most cases restricted and one low cost solution but with high impact and flexibility was developing of a specialized MATLAB Scientific Toolbox to calculate full-field strain and stress distribution in components based on measured values given by different full-field optical methods. Beside the development of the toolbox the chapter presents some applications realized by the author: determination of stress concentration in a tensile specimen, determination of strain-stress values in a clamped plate loaded by a central concentrated force and determination of shear stresses in bars subjected to torsion using membrane analogy and shadow moiré.

Second section of the thesis briefly reviews the *didactic skills and professional achievements* underlining the following aspects: courses, seminars and laboratories that author is responsible for, student scientific activities of the Faculty of Mechanical Engineering, implication in professional competitions in the field of strength of materials, introduction of modern teaching methods and seminar software, participation as official referent for doctoral theses, achievements in institutional development and participation in committees and commissions in the interest of education.

Third section presents the plans for *future scientific and academic development*. In the scientific field the above mentioned research directions will continue but the effort will increase in those directions which facilitate publications in top research journals or access to the research projects. Among the plans concerning the didactic field there are: ensurance the continuity of the activities of publishing teaching materials for the students, introduction of optional courses, participation in multidisciplinary master programs, participation in international programs for the exchange of students, participation in projects with educational purpose and the last but not least attracting and mentoring of young people able and willing to pursue a doctoral stage and at the end an university career in the field of mechanics of materials.

b. ACHIEVEMENTS AND DEVELOPMENT PLANS

b-i. RESEARCH ACHIEVEMENTS

1. RESEARCH DIRECTIONS AND COMPETENCES

The major research topics of the Strength of Materials group of disciplines to which I join from the beginning of my academic career were the development and implementation of various experimental methods in measuring of strain and stress, particularly in the use of optical methods of experimental mechanics. Following my mentor and PhD tutor, the regretted Professor Ioan PASTRAV, who was a dedicated promoter of the optical methods of experimental mechanics and founder of the Optical Methods in Experimental Mechanics Laboratory, my research activity was mainly oriented to this area. In the field of experimental methods there are two main research directions, on the one hand the development/improvement of new techniques/equipment and on the other hand to solve specific applications required by the basic research and industrial environment. If the first direction was highly required and encountered a significant progress 15 years ago, the second one is more appreciated today when mechanics of materials has to be applied to composites, bone-like materials, biological tissues, micro-structures, etc. These two developments should be synergic and offer the possibility to publish in top journals or to access research projects.

Research that I carried out so far was based on solving research grants both at national and international level. Through competition at European level I have won scholarships/research grants funded by the European Commission through FP5 programme (Speckle interferometry for industrial needs - strain-stress calculation and link to finite element analysis, Marie-Curie Fellowship, 2001-2003) or from prestigious foundation Alexander von Humboldt (Analysis of elastic-plastic characteristics by Electronic Speckle Pattern Interferometry, 2005-2006). Within these scholarships/research grants I solved complex problems in the field of optical methods of solid mechanics with application in industrial research - at the company Dantec-Ettemeyer GmbH, Germany (the world leader in measuring systems based on speckle interferometry) and in academia - at the Technical University of Chemnitz, Department of Experimental Mechanics. Characterisations and the certificates that were awarded at the completion of these research internships abroad have shown a very positive feedback, reflecting the quality and quantity of performed activities. I also held the position of a researcher in a comprehensive research grant at the Technical University of Chemnitz Germany with funds from the German Ministry of Research (Deutsche Forschungsgemeinschaft). Within project I realized over a period of seven months (2005) a comprehensive study of thermal stresses in composite materials by speckle interferometry.

Knowledge and skills gained during the periods spent abroad, both in terms of the methodology and management of research projects have been a real help in obtaining future funding. Within the framework of the Technical University of Cluj-Napoca I was the project manager at two grants, one financed by the European Community Sixth Framework Programme (FP6), Directorate-General for Research, Human Resources and Mobility (MATLAB Scientific Toolbox for Strain-Stress Analysis, Marie Curie European Reintegration Grants, 2004-2005) and the Hertie Stiftung & Alexander von Humboldt Stiftung Germany (Analysis of the strain gauge

properties applied on wood, 2007-2008). As a project manager I have successfully completed also a national research grant for young scientists over a period of two years (2004-2005). The research project was focused on introducing modern experimental methods of analysis of the deformations and stresses in elastic membranes.

The transfer of knowledge to the industrial environment has been continuously achieved by applying research projects with Romanian or international companies. Throughout this period I have cooperated very well with various research groups on seven national research projects and two international ones.

Since 2011 I have joined the new formed Laboratory for Micro and Nano-Systems (MiNaS) as an experienced researcher. The fruitful collaboration within this research team leads to numerous publication in ISI indexed journals and at prestigious international conferences, all as a result of the implementation of four national and international projects.

The research activities, given by the most relevant publications, can be defined, at this moment, in four main directions:

1) Experimental methods in solid mechanics

In this field I have the most cited papers, and this is the reason why the habilitation thesis is dedicated to this topic. Beside the articles published in the last 15 years, a part of research activity was condensed in one monograph and one laboratory work. The monograph is from my knowledge the only one dedicated to Electronic Speckle Pattern Interferometry written in Romania and represents the theoretic and practic experience over many years in this field. The significant publications in this field have been published in Strain (official Journal of the European Association of Experimental Mechanics – EURASEM, IF 0.916) or at international conferences and there are partly mentioned in the following list.

Books

1. **Mircea Cristian Dudescu**, (2010): *Introducere în interferometria electronică granulară*. Editura Risoprint, Cluj-Napoca, ISBN 978-973-53-0291-7, 164 pag.
2. Ioan Păstrav, **Mircea Cristian Dudescu** (2009): *Lucrări de laborator de metode optice de analiză a tensiunilor*. Editura U.T.Pres, Cluj-Napoca, ISBN 978-973-662-452-0, 92 pag.

Relevant articles (indexed by ISI Web of Science, Scopus)

1. Chiorean, R., **Dudescu, C.**, Pustan, M., Hărdău, M. (2014): *V-beam Thermal Actuator's Performance Analysis Using Digital Image Correlation*, Applied Mechanics and Materials Vol. 658 (2014) pp 173-176, DOI: [10.4028/www.scientific.net/AMM.658.173](https://doi.org/10.4028/www.scientific.net/AMM.658.173)
2. Chiorean, R., **Dudescu, C.**, Pustan, M., Hardau, M. (2014): *Deflection determination of V-beam thermal sensors using Digital Image Correlation*, Key Engineering Materials, vol. 601 (2014) pp. 41-44, DOI: [10.4028/www.scientific.net/KEM.601.41](https://doi.org/10.4028/www.scientific.net/KEM.601.41)
3. Cherecheș, A., **Dudescu, C.**, Lakatos, G., Vidican, I., Bejan, M. (2014): *State of stress determination in a water drinker by numerical and experimental methods*, Key Engineering Materials, vol. 601 (2014) pp. 45-49, DOI: [10.4028/www.scientific.net/KEM.601.45](https://doi.org/10.4028/www.scientific.net/KEM.601.45)
4. **Dudescu, M.C.**, Stockmann, M., Naumann, J. (2012): *Optical measurement of the strain-stress response during unloading of metal sheets undergoing large plastic deformations*. In: 11th IMEKO TC15 Youth Symposium on Experimental Solid Mechanics, 30th of May 2012 – 2nd of June 2012, Brasov, Romania, ISBN 978-606-19-0078-7, pp. 204-209. ([Scopus](#)).
5. **Dudescu, C.** (2011): *Measurement of materials properties by electronic speckle pattern interferometry*. In: 10th IMEKO TC15 Youth Symposium on Experimental Solid Mechanics,

- 25-28 May 2011, Chemnitz, Germany ([Keynote lecture](#)) ISBN 978-3-941003-34-7, pp.26-27. ([Scopus](#)).
6. **Dudescu, C.**, Naumann, J., Stockmann, M. and Steger H. (2011): *Investigation of Non-linear Springback for High Strength Steel Sheets by ESPI*. STRAIN - International Journal of Experimental Mechanics, Blackwell Publishing, UK, Vol. 47, Issue Suppl.2, pp. 8-18, DOI: [10.1111/j.1475-1305.2009.00729.x](https://doi.org/10.1111/j.1475-1305.2009.00729.x).
 7. **Dudescu, M.**, Naumann, J., Stockmann, M., Nebel, S., (2006): *Characterisation of Thermal Expansion Coefficient of Anisotropic Materials by ESPI*. STRAIN - International Journal of Experimental Mechanics, Blackwell Publishing, UK, Vol. 42, Issue 3, August 2006, pp. 197-206, DOI: [10.1111/j.1475-1305.2006.00271.x](https://doi.org/10.1111/j.1475-1305.2006.00271.x).
 8. **Dudescu, M.**, Botean, A., Hărdău, M. (2009): *Application of digital image correlation for measuring e-modulus of wood beam*. Annals of DAAAM for 2009 & Proceedings of 20th DAAAM International Symposium "Intelligent Manufacturing & Automation: Theory, Practice & Education", Vienna, Austria, 25-28th November 2009, pp.42-44, ISBN 978-3-901509-70-4 (WoS).
 9. **Dudescu, M.**, Păstrav, I., Şomotecan, M. (2008): *Aspects related application of the electrical strain gauges on wood*. 25th Danubia-Adria Symposium on Advances in Experimental Mechanics, Ceske Budejovice, CZECH REPUBLIC, Sep. 24-27, pp. 59-60 (WoS).

2) Material testing and characterization

In materials science characterization refers to the broad and general process by which a material's structure and properties are probed and measured. It is a fundamental process in this field, without which no scientific understanding of engineering materials could be ascertained. Researches in this field were performed on one hand due to the increased number of polymers and other materials or technologies used in the last decade in biomedical applications and on the other hand due to the increase interest in mechanical characterization of microstructures based on atomic force microscopy (AFM).

The most relevant publications reflecting this research activity can be found in following journals: International Journal of Materials Research (IF 0,675), Rapid Prototyping Journal (IF 1,156), Journal of Alloys and Compounds (IF 2,726), Advances in Materials Science and Engineering (IF 0,897), Materiale Plastice (IF 0,463) and Revista de Chimie (IF 0,677).

Relevant articles (indexed by ISI Web of Science, Scopus)

1. Miron-Borzan, C.S., **Dudescu, M.C.**, Khalid Abd Elghany, Ceclan, V., Berce P. (2015): *Analysis of Mechanical Properties of Selective Laser Sintered Polyamide Parts Obtained on Different Equipment*. Materiale Plastice, **52**(1), pp. 39-42.
2. Leordean, D., **Dudescu C.**, Marcu, T., Berce, P., Bâlc, N. (2015): *Aspects related to the application of the selective laser melting technology to customized Ti-6Al-7Nb implants*. Rapid Prototyping Journal, vol. 21 issue 1, pp. DOI: [10.1108/RPJ-11-2012-0107](https://doi.org/10.1108/RPJ-11-2012-0107)
3. Pop, S.I., **Dudescu, M.**, Bratu, D.C., Merie, V.V., Pacurar, M. (2015): *Effect of Esthetic Coating on the Load Deflection and Surface Characteristics of the NiTi Orthodontic Archwires*. Revista de Chimie, 66 (3), pp. 364-367.
4. **Dudescu, C.**, Botean, A., Hărdău, M., Bal, N. (2014): *Measurement of thermoplastics tensile properties using digital image correlation*, Key Engineering Materials, vol. 601 (2014) pp. 33-36, DOI:[10.4028/www.scientific.net/KEM.601.33](https://doi.org/10.4028/www.scientific.net/KEM.601.33).
5. Bere P., **Dudescu M.C.**, Balc N., Berce P., Iurian A.M., Nemes O. (2014): *Design and analysis of carbon/epoxy composite bicycle handlebar*, Materiale Plastice **51**(2), pp. 145-149.
6. Paşcalău, V., Popescu, V., Popescu, G., **Dudescu, M.C.**, Borodi, G., Dinescu, A., Moldovan, M. (2013): *Obtaining and Characterizing Alginate/k-Carrageenan Hydrogel Cross-Linked with*

- Adipic Dihydrazide*, Advances in Materials Science and Engineering, vol. 2013, Article ID 380716, 12 pages, DOI: [10.1155/2013/380716](https://doi.org/10.1155/2013/380716)
7. **Dudescu, C.**, Botean, A., Hardau, M. (2013): *Thermal expansion coefficient determination of polymeric materials using digital image correlation*, Materiale Plastice **50** (1) pp. 55-59.
 8. Pustan, M., **Dudescu, C.**, Birleanu, C., Rymuza, Z. (2013): *Nanomechanical studies and materials characterization of metal/polymer bilayer MEMS cantilevers*, International Journal of Materials Research, volume 12, pp. 1-7, DOI: [10.3139/146.110879](https://doi.org/10.3139/146.110879)
 9. Mager, V., Balc N., Leordean D., **Dudescu C.**, Fockele M. (2013): *Research on Producing Complex Metal Parts with Lattice Structure, by Selective Laser Melting*. Applied Mechanics and Materials, Vol. 371 (2013), pp. 280-284, Trans Tech Publications, Switzerland, DOI: [10.4028/www.scientific.net/AMM.371.280](https://doi.org/10.4028/www.scientific.net/AMM.371.280)
 10. Bere, P., Nemeş O., **Dudescu, C.**, Berce, P., Sabău, E. (2013): *Design and Analysis of Carbon/Epoxy Composite Tubular Parts*. Advanced Engineering Forum Vols. 8-9 (2013) pp. 207-214, Trans Tech Publications, Switzerland, DOI: [10.4028/www.scientific.net/AEF.8-9.207](https://doi.org/10.4028/www.scientific.net/AEF.8-9.207)
 11. Pop, S.I., **Dudescu, M.**, Bratu, D.C., Pop, R.V., Păcurar M., Petrişor, M. (2013): *Influence of the Chemical Composition on the Mechanical Properties of Orthodontic Archwires*, Revista de Chimie, 64, Issue 7, pp. 771-775.
 12. Bratu, D.C., Pop, S.I., Balan, R., **Dudescu, M.**, Petrescu, H.P., Popa, G. (2013): *Effect of Different Artificial Saliva on the Mechanical Properties of Orthodontic Elastomers Ligatures*. Materiale Plastice **50** (1), pp. 49-52.
 13. Pascalau, V., Popescu, V., Popescu, G.L., **Dudescu, M.C.**, Borodi, G., Dinescu, A., Perhaița, I., Paul, M. (2012): *The alginate/k-carrageenan ratio's influence on the properties of the cross-linked composite films*. Journal of Alloys and Compounds, Vol. 536, Suppl. 1, pag. S418-S423, DOI [10.1016/j.jallcom.2011.12.026](https://doi.org/10.1016/j.jallcom.2011.12.026).

3) Structural analysis and numerical simulation of MEMS

Micro-Electro-Mechanical Systems, or MEMS, is a technology that in its most general form can be defined as miniaturized mechanical and electro-mechanical elements that are made using the techniques of microfabrication. Types of MEMS devices can vary from relatively simple structures having no moving elements, to extremely complex electromechanical systems with multiple moving elements under the control of integrated microelectronics. The one main criterion of MEMS is that there are at least some elements having some sort of mechanical functionality whether or not these elements can move. While the functional elements of MEMS are miniaturized structures, sensors, actuators, and microelectronics, the most notable and interesting elements are the microsensors and microactuators.

The most relevant publications reflecting this research activity performed as experience researcher of MiNaS Laboratory (www.minas.utcluj.ro) can be found in form a book chapter and several journals: Analog Integrated Circuits and Signal Processing (IF 0,401), Sensor Letters (IF 0.558) and Microsystems Technologies (IF 0.952).

Book Chapter

1. Pustan, M., Birleanu, C., **Dudescu C.**, Golinval, J.C. (2013): *Smart sensors and MEMS: Intelligent devices and microsystems for industrial applications*, Woodhead Publishing Limited, Cambridge, UK, ISBN 0-85709-502-1, Chapter 12 "Dynamical behavior of smart MEMS in industrial applications", pp. 349-365, DOI: [10.1533/9780857099297.2.349](https://doi.org/10.1533/9780857099297.2.349)

Relevant articles (indexed by ISI Web of Science, Scopus)

1. Pustan, M., **Dudescu, C.**, Birleanu, C. (2015): *The effect of sensing area position on the mechanical response of mass - detecting cantilever sensor*. Microsystems Technologies, article in press, DOI: [10.1007/s00542-015-2536-1](https://doi.org/10.1007/s00542-015-2536-1)
2. Baracu, A., Voicu, R., Müller, R., Avram, A., Pustan, M., Chiorean, R., Birleanu, C., **Dudescu, C.** (2015): *Design and fabrication of a MEMS chevron-type thermal actuator*. AIP Conference Proceedings, 1646, pp.25-30, DOI: [10.1063/1.4908578](https://doi.org/10.1063/1.4908578)
3. Pustan, M., **Dudescu, C.**, Birleanu, C. (2015): *Nanomechanical and nanotribological characterization of a MEMS micromembrane supported by two folded hinges*. Analog Integrated Circuits and Signal Processing, 82 (3), pp. 627-635, DOI: [10.1007/s10470-014-0482-y](https://doi.org/10.1007/s10470-014-0482-y)
4. Pustan, M., **Dudescu, C.**, Birleanu, C. (2014): *Reliability Design Based on Experimental Investigations of Paddle MEMS Cantilevers Used in Mass Sensing Applications*. Sensor Letters, 12 (11), pp. 1600-1606(7), DOI: [10.1166/sl.2014.3371](https://doi.org/10.1166/sl.2014.3371)
5. Pustan, M., Birleanu, C., Rusu, F., **Dudescu, C.**, Belcin, O. (2014): *Size effect on the microbridges quality factor tested in free air space*, 15th IEEE International Conference on Thermal, Mechanical and Multi-Physics Simulation and Experiments in Microelectronics and Microsystems (EuroSimE 2014), 7-9 April 2014 Gent, Belgium, p. 1/6 - 6/6, ISBN 978-1-4799-4791-1, DOI: [10.1109/EuroSimE.2013.6529890](https://doi.org/10.1109/EuroSimE.2013.6529890).
6. Chiorean, R., **Dudescu, C.**, Pustan, M., Hardau, M. (2014): *Analytical and Numerical Study on the Maximum Force Developed by a V-beam Thermal Actuator*, Procedia Technology, vol. 12, pp. 359–363, DOI: [10.1016/j.protcy.2013.12.499](https://doi.org/10.1016/j.protcy.2013.12.499)
7. Pustan, M., Birleanu, C., **Dudescu, C.** (2013): *Simulation and experimental analysis of thermo-mechanical behavior of microresonators under dynamic loading*, Microsystems Technologies, vol. 19, Issue 6, pp. 915-922, DOI: [10.1007/s00542-012-1728-1](https://doi.org/10.1007/s00542-012-1728-1).
8. Pustan, M., **Dudescu, C.**, Birleanu, C. (2013): *The effect of sensing area position on the mechanical response of mass - detecting cantilever sensor*. Symposium on Design, Test, Integration and Packaging of MEMS/MOEMS (DTIP 2013), 16-18 April 2013 Barcelona, Spain, p. 173-179, ISBN: 978-2-35500-025-6, [IEEE Xplore](https://doi.org/10.1109/DTIP.2013.6529890).
9. Pustan, M., Birleanu, C., **Dudescu, C.**, Belcin, O. (2013): *Temperature Effect on Tribological and Mechanical Properties of MEMS*. 14th IEEE International Conference on Thermal, Mechanical and Multi-Physics Simulation and Experiments in Microelectronics and Microsystems (EuroSimE 2013), 15-17 April 2013 Warsaw, Poland, p.1/6 - 6/6, ISBN 978-1-4673-6139-2, IEEE Catalog number CFP13566-CDR, DOI: [10.1109/EuroSimE.2013.6529890](https://doi.org/10.1109/EuroSimE.2013.6529890)
10. Pustan, M., Birleanu, C., **Dudescu, C.** (2012): *Simulation and experimental analysis of thermo-mechanical behavior of microresonators under dynamic loading*. Symposium on Design, Test, Integration and Packaging of MEMS/MOEMS (DTIP 2012), 25-27 April 2012 Cannes, France, p. 87-92, ISBN: 978-2-35500-020-1, [IEEE Xplore](https://doi.org/10.1109/DTIP.2012.6191802).
11. Pustan, M., Birleanu, C., **Dudescu, C.**, Belcin, O., (2012): *Mechanical and tribological characterizations for reliability design of micromembranes*. 13th IEEE International Conference on Thermal, Mechanical and Multi-Physics Simulation and Experiments in Microelectronics and Microsystems (EuroSimE), Portugal, p. 1/6 - 6/6. DOI: [10.1109/ESimE.2012.6191802](https://doi.org/10.1109/ESimE.2012.6191802).

4) Biomedical engineering

Biomedical Engineering is an emerging interdisciplinary field that combines engineering with life sciences. This field closes the gap between engineering and medicine and combines the design and problem solving skills of engineering with medical and biological sciences to advance health care treatment, diagnosis and monitoring. Biomedical engineering has only recently emerged as a new study, much of the work in biomedical engineering consists of

research and development of biocompatible prostheses, various diagnostic and therapeutic medical devices ranging from clinical equipment to micro-implants, common imaging equipment such as MRIs and EEGs, regenerative tissue growth, etc.

The most relevant publications reflecting this research activity can be found in following journals: American Journal of Neuroradiology (IF 3,680) and Neuropediatrics (IF 1.104). There are also some relevant publications that can be mentioned as a result of a collaboration with a group of researchers working in oral medicine:

Relevant articles (indexed by ISI Web of Science, Scopus):

1. Ilea, A., Cristea, A., **Dudescu, C.**, Hurubeanu, L., Vâjâean, C., Albu, S., Câmpian, R. (2015): *Lip Forces and Chewing Efficiency in Children with Peripheral Facial Paralysis*. Neuropediatrics, article in press, DOI: [10.1055/s-0035-1550146](https://doi.org/10.1055/s-0035-1550146)
2. Ilea, A., Butnaru, A., Sfrângeu, S., **Dudescu, M. C.**, Câmpian, R. S., Tombitaş, V. E., Albu, S. (2015): *The Use of Bone-Like Materials in Skull Base Traumatology*. Key Engineering Materials, Vol 638, pp. 274-279, DOI: [10.4028/www.scientific.net/KEM.638.274](https://doi.org/10.4028/www.scientific.net/KEM.638.274)
3. Takacs, I., **Dudescu, C.**, Hărdău, M., Botean, A. (2014): *Experimental Validation of a Finite Element Model of an Osteoporotic Human Femoral Bone Using Strain Gauge Measurement*, Applied Mechanics and Materials Vol. 658 (2014) pp 513-519, DOI: [10.4028/www.scientific.net/AMM.658.513](https://doi.org/10.4028/www.scientific.net/AMM.658.513)
4. Chiorean, R., **Dudescu, C.**, Pustan, M., Hărdău, M. (2014): *Micro-tweezers Based on V-Beam Thermal Actuator*, International Conference on Advancements of Medicine and Health Care through Technology; 5th – 7th June 2014, Cluj-Napoca, Romania, IFMBE Proceedings, vol. 44, pp.159-162, DOI: [10.1007/978-3-319-07653-9_32](https://doi.org/10.1007/978-3-319-07653-9_32).
5. Ilea, A., Butnaru, A., Sfrângeu, S.A., Hedeşiu, M., **Dudescu, C.M.**, Berce, P., Chezan, H., Hurubeanu, L., Trombitaş, V.E., Câmpian, R.S., Albu, S. (2014): *Role of Mastoid Pneumatization in Temporal Bone Fractures*, American Journal of Neuroradiology, DOI: [10.3174/ajnr.A3887](https://doi.org/10.3174/ajnr.A3887)
6. **Dudescu, M.**, Mândru, D. (2011): *Analysis of a Dexterous Instrument for Minimally Invasive Procedures, Based on Bellows Actuators*. In: International conference on advancements of medicine and health care through technology, Cluj-Napoca, Romania. IFMBE Proceedings, 2011, vol. 36, Part 2, pp.176-179, DOI: [10.1007/978-3-642-22586-4_38](https://doi.org/10.1007/978-3-642-22586-4_38).

2. OPTICAL METHODS IN EXPERIMENTAL MECHANICS

2.1. Context of experimental mechanics

Experimental Mechanics is an interdisciplinary topic including mechanics of materials, physics and mathematics with the scope to increase the knowledge of physical phenomena, further the understanding of the behavior of materials, structures and systems and to provide the necessary physical basis and verification for analytical and computational approaches to the development of engineering solutions [1].

Stress analysis has been considered for some time as a distinct professional branch of engineering, the main objective to determine and improve the mechanical strength of elements, structures and machines. Experimental stress analysis strives to achieve these aims by experimental means. In the investigation of problems of mechanical strength, many factors make the experimental approach indispensable, and often the only means of access. In addition to this, theoretical considerations are usually based on simplifying assumptions which imply certain deviations from reality, and it can be established only by experimentation whether such idealization do not produce an undue distortion of the essential features of the problem. Using experimental stress analysis is required especially if the analysis is done under real service conditions, where all the factors due to the properties of the employed materials, the methods of manufacture, and the conditions of operation are fully represented. From the point of view of the average practicing engineer, whose mathematical preparation is not likely to enable him to deal theoretically with some of the complex strength problems, experimental methods constitute a recourse that is more readily accessible and that, with proper knowledge and equipment, is most likely to provide the needed information [2]. As stated by Prof. Kobayashi, recognized for his many fundamental contributions to the fields of experimental stress analysis and fracture mechanics [1] "One of the frustration of experimental stress analyst is the lack of universal experimental procedure that solves all the problems".

Numerous methods of experimental mechanics of solids has been employed from the beginning of mechanics of materials. Some methods may have been overshadowed by newer more handy and more powerful methods but all the experimental methods remain always valid. The progress of computers changed our daily life and had an incredible impact on the optical methods of experimental mechanics[3]. Digital photoelasticity taking advantage of computer technology and digital image processing techniques emerged in the eighties. Moiré techniques have also substantially benefited. The specimen grating could be transferred to the computer screen and can be superimposed with the reference grating, a task performed previously directly on the specimen. Of high impact on experimental methods was the development of the digital image correlation (DIC) method for measurement of displacements. The advantage of the method is that it can be used in structures covering the macro-micro and nano-scale levels. It has been commercialized and it is relatively easy for the novice experimentalist to set up the optical arrangement, use the software and obtain results [3].

The following methods are considered as being an integrated part of Experimental Mechanics and most of them are included in the curriculum of an experimental mechanics course in engineering education[3]:

(1) **Strain gages:** Although more than 70 years old, strain gages constitute the most convenient and widely used method of strain measurement in laboratory and field applications. They are inexpensive and require minimum instrumentation.

(2) **Photoelasticity**: Constitutes the most powerful and widely used method in stress analysis. There is no need for special precautions during the test, with just a set of polarizing filters one can have a direct full-field image of the residual stresses in a plastic.

(3) **Geometric moiré**: The moiré phenomenon appears in our everyday life. The method is simple, easy to apply and needs minimum instrumentation. It constitutes a full field method, like photoelasticity but it is limited by the minimum deformation that can be measured.

(4) **Interferometric moiré**: Extends the limits of applicability of geometric moiré in measuring smaller displacements. However, special precautions should be taken during the test.

(5) **Interferometry**: Can be used to measure displacements of the order of the wavelength of light. It can easily be applied and needs minimum instrumentation.

(6) **Holography**: Both the amplitude and phase on a wave can be reconstructed. It can be used in combination with photoelasticity and interferometry. It requires special precautions during the test.

(7) **Speckle methods**: The speckle pattern of a specimen carries necessary information for the determination of displacements. The method can be used in combination with photography and interferometry.

(8) **Optical metrology**: It constitutes an important component of all optical methods. Images of an object are digitized and stored in a computer. They can be analysed and processed at a later time.

(9) **Digital image correlation (DIC)**: It is the most widely used optical method of our times. Most laboratories are equipped with cameras and software. Student can use it as black box for displacement measurements.

(10) **Optical fibres**: They are widely used in structural applications for in-situ measurement of stresses.

(11) **Thermoelasticity**: It is used for the measurement of the sum of the principal stresses. It needs an infrared detector for measuring small temperature changes.

(12) **Nanoindentation**: Constitutes a powerful method for measuring the mechanical properties and fracture toughness of materials at the macro- micro- and nano-scale levels. The method has precursors, the Brinell and Vickers tests, used to measure the hardness of materials since the beginning of the twentieth century.

(13) **Non-destructive testing (NDT)**: Radiography, ultrasonics and acoustic emission are widely used for non-destructive interrogation of structures. Radiography uses X- or γ -rays, while in ultrasonics ultrasonic waves are transmitted through the specimen. In acoustic emission sensing transducers and sophisticated electronic equipment is used to detect sounds and stress waves emitted inside the material by defects.

Today's experimentalist armed with a strong background in numerical methods and computer techniques and deep understanding of the basic experimental methods as outlined above, should have the tools necessary to solve problems of structural behavior and material characterization at the nano-, micro- and macro-scale levels. Emmanuel E. Gdoutos former president of Society for Experimental Mechanics (SEM) said that "the most valuable virtues of an experimentalists are not his/her technical skills, but honesty and integrity. Experimental results should be presented as obtained from the tests, unbiased of any relations with analytical solutions, in case they exist. This most valuable virtue should be cultivated in classrooms and laboratories"[3].

A special place among the experimental techniques is occupied by optical methods. It is now well established that optical methods of experimental mechanics greatly benefited from the important developments in computing performance and in digital vision [4, 5]. Since the

1990's, noncontact imaging measurements obtained from various types of sensors have been widely used in different researches. This activity led to the emergence of a new research field in Mechanics of Materials, namely 'Photo-Mechanics'[6]. For instance, the first conference dedicated to the so-called "Photo-Mechanics" techniques was launched in France at the beginning of the 1990's, and there are now systematically full sessions dedicated to these techniques in the most important congresses worldwide. The Photo-Mechanic's techniques can be used for different purposes [7]. In a first approach, they can give access to different variables of interest (radiance, density, displacement, etc.) or to state variables such as the temperature or the deformation. Among their numerous possible applications, they can help the experimentalist to characterize the mechanisms governing the materials' behavior. They can also be used for material parameters identification or for data completion. As these techniques give access to the time-evolution of fields of data at different scales, they are naturally suitable for comparison with analytical or numerical solutions, and consequently, they tend to be more and more integrated with numerical methods.

These techniques have several features in common: they are non-contact, they provide full-field data and they require complex acquisition chains and data-processing procedures to extract the information at the relevant (spatial and temporal) scale from the recorded images. Therefore, they necessitate a good knowledge in complementary fields such as theoretical, numerical and experimental optics, mechanics and thermal sciences and also material sciences, and signal and image processing. During the last decades, many improvements have been made on the hardware, mainly with the significant improvements in performance of imaging devices. These progresses were associated with a considerable development of numerical data-processing methods, and with the development of specific software/libraries allowing different post processing strategies of raw data in order to have various full-field measurements. Depending on the volume and surface properties of the studied material, the emitted, reflected or transmitted radiations can be processed to obtain surface (external) or volume (internal) measurements.

The optical experimental techniques and the associated data or image processing are often organized in the following and non-exhaustive classification [6]: tomographic measurements (X-Ray tomography, optical coherence tomography, etc.), kinematic measurements (surface or volume Digital Image Correlation, Moiré interferometry, Grid method, Electronic Speckle Pattern Interferometry, etc.), thermal and calorimetric measurements (Infrared Thermography). Should be also mentioned the wide range of their applications (bio-mechanics, thermo-hygro-mechanical couplings, fatigue, fracture mechanics, identification of fields of material properties) and the multiplicity of possible loadings (quasi-static/dynamic, mechanical/hydromechanical/hydrothermal, uniaxial/biaxial tensile tests, indentation, etc.)[6].

The future of optical methods is essentially dependent on the needs and expectations of experimental mechanics. Now, there are many signs that the demand is strongly up. All major branches of experimental mechanics – material properties, structural analysis, non-destructive testing – are facing challenges of unprecedented complexity. As exemplified by civil or aeronautical engineering, the trends are towards ever more streamlined constructions, having to bear record loadings, while under increasingly severe environmental constraints and security levels. Testing of complex micro-systems (MEMS) in static / dynamic regime is another field with an increase demand in the last years. Modelling tasks need to be more and more accurate and computer simulations must be checked carefully.

2.2. Photoelasticity

2.2.1. Introduction

Photoelasticity is a whole-field optical experimental technique that is based on the principle of stress induced birefringence [8]. It directly gives information about principal stress difference (isochromatics) and principal stress direction (isoclinics) in the form of fringe contours. Photoelasticity is useful as a design tool, to understand complex phenomenological issues, and it is an excellent teaching aid for stress analysis. Many experimental analysis techniques were then developed for both research and industrial purposes. It can be used to study models made of transparent plastics (transmission photoelasticity), prototypes made of different materials, and also directly on end products such as glass components (reflection photoelasticity).

In the early stages of its development, quantitative isochromatic data were obtained easily only at the fringe contours and compensation techniques were required to evaluate them at other places. Since the advent of computer software, the use of photoelasticity in industrial design has become less prominent. Extensive use of digital computers coupled with cost-effective image processing systems have significantly revolutionized photoelastic analysis and open the way for a new branch of photoelasticity, known as digital photoelasticity [9, 10]. With developments in rapid proto-typing and novel methods for fringe plotting from finite element results, the technique is ideally suited for hybrid analysis of complex problems [2].

Photoelasticity is based on the phenomenon of birefringence that may appear on optically isotropic materials such as glass or certain polymers (epoxy, polycarbonate, etc.) that have the property of becoming birefringent when subjected to stress. Initially, the material that is considered optically isotropic is characterized by a refractive index n for all directions. Under stress this medium is characterized by an ellipsoid of refractive indices. This phenomenon was discovered by Brewster in 1816. The ellipsoid of refractive indices is such that its principal directions coincide with the principal directions of stresses. In the 19th Century, was determined the laws linking the principal optical indices to the principal stresses (stress-optic law).

Study of photoelastic model is made in polarized light using a polariscope. Arrangement and optical elements forming a polariscope can lead to so called plane polariscope set-up or circular polariscope set-up.

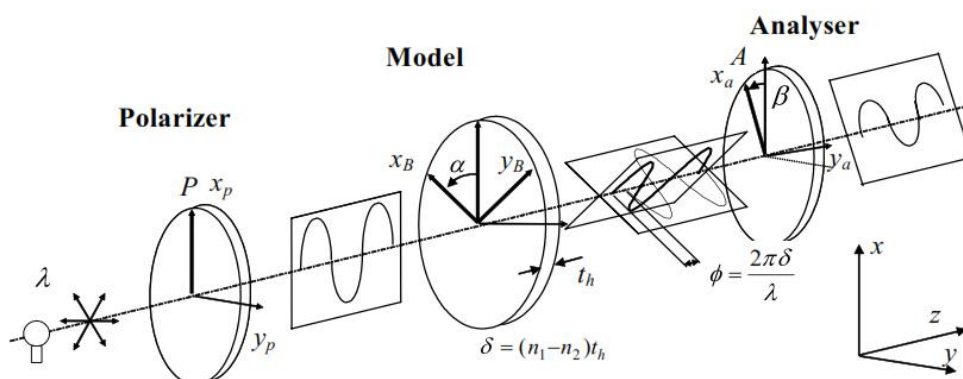


Fig. 2.2.1. Principle of plane polariscope

In figure 2.2.1 [8] is presented an experimental set-up of a plane polariscope formed by a light source giving a plane wave, two polarizers (the one closest to the light source being the polarizer and the one nearest the observer being the analyser), a measuring device

(photomultiplier, photographic film, eye, digital camera) and the model to be analysed. Ox_B and Oy_B are the principal directions of stress in the loaded model.

The light intensity recorded by a measurement device is given by:

$$I = I_0 \left(\cos^2 \beta - \sin 2\alpha \sin 2(\alpha - \beta) \sin^2 \frac{\phi}{2} \right) \quad (2.2.1)$$

where $I_0=A^2$ as the intensity of the background.

By varying angle β , we find the expressions of light obtained by a parallel arrangement plane polariscope ($\beta = 0$) or by a crossed arrangement plane polariscope ($\beta = \pi/2$). The example shown in Figure 2.2.1 shows the image obtained through a plane polariscope with a crossed arrangement for an epoxy disk subjected to diametric compression. The analysis of light zones (called white fringes) and dark zones (called black fringes) provides knowledge of the principal differences in stress[8].

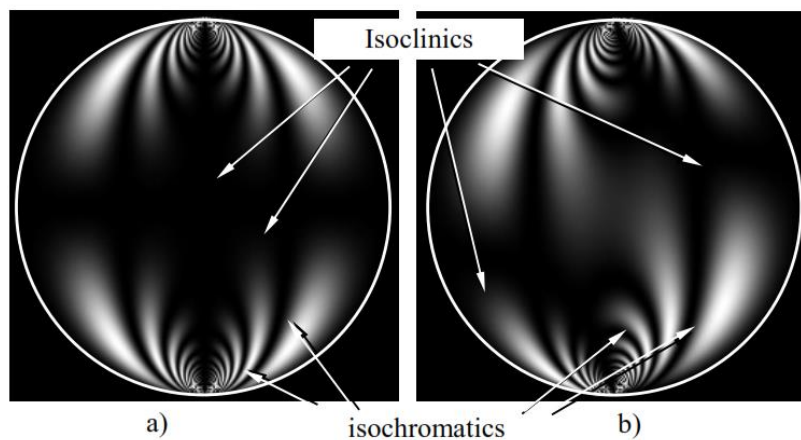


Fig. 2.2.2. Dark field plane polariscope for a disk under diametric compression for two orientations: a) $\alpha=0^\circ$ and b) $\alpha=15^\circ$

Outside the model or in unstressed conditions, we obtain $I=0$, so this crossed plane polariscope is also called a dark field. Thus, in such a polariscope described in relation (2.2.1), the light intensity I is zero (dark fringes) when $\sin 2\alpha = 0 \Rightarrow \alpha = k \pi/2$. These lines are called *isoclinics*; they are independent of the loading intensity and the wavelength of the light. They can change either by rotating the model along the z-axis inside the polariscope or, more easily, by rotating both the polarizer and analyser. They indicate the location of points where one of the principal orientations of stress is parallel to the direction of polarization.

When $\sin \phi/2 = 0 \Rightarrow \phi=2\pi k$ results $k = tC(\sigma_2 - \sigma_1)/\lambda$. These lines are called *isochromatics*; they represent equal maximum shear stress and they are dependent on the intensity of the load applied and the wavelength used. Along an isochromatic, the optical path difference is equal to an integer number of wavelengths. These lines are called isochromatics because when observed with white light (large spectrum) they are the same colour.

A circular polariscope comprises a light source giving a plane wave, a circular polarizer, a quarter-wave plate, the analysed model, a second quarter-wave plate, the analyser and a recording device. We can obtain different arrangements depending on the orientation γ of the second quarter-wave plate.

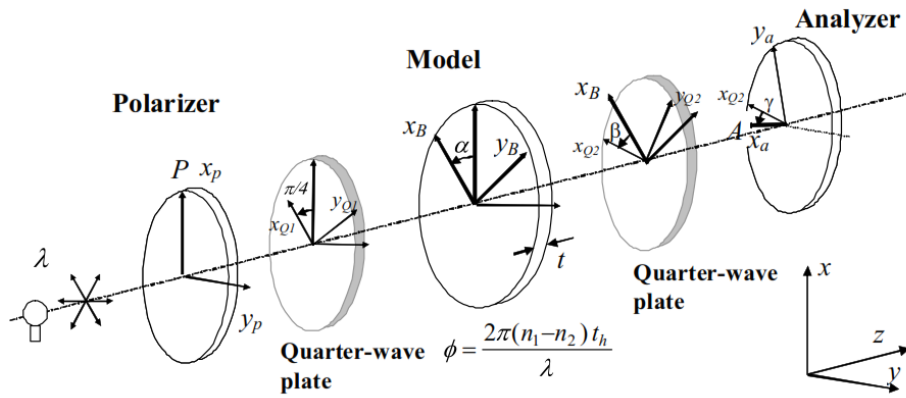


Fig. 2.2.3. Scheme of a circular polariscope

A similar approach to that of the plane polariscope allows us to calculate the following expression for the output light intensity:

$$I = \frac{I_0}{2} (1 + \sin 2\gamma \cos \phi + \sin 2\beta \sin 2\gamma \sin \phi) \tag{2.2.2}$$

When $\gamma = -\pi/4$, we obtain a dark field circular polariscope arrangement and the light intensity is $I = \frac{I_0}{2} \sin^2 \frac{\phi}{2}$. We can note that with this arrangement, isoclinics have been eliminated (Fig. 2.2.4[8]). Outside the model, or when the model is unstressed, the emergent light intensity is zero. Consequently we have a dark field, and the dark fringes are given by an integer number.

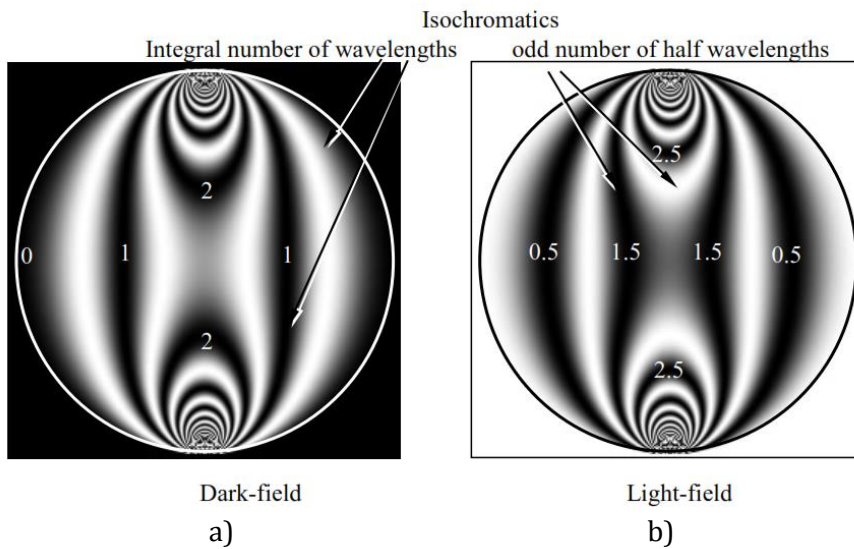


Fig. 2.2.4. Isochromatic patterns obtained with a circular polariscope: a) dark field and b) light field.

When $\gamma = \pi/4$, we obtain a light-field circular polariscope arrangement; the emergent light intensity is given by: $I = \frac{I_0}{2} \left(1 - \sin^2 \frac{\phi}{2}\right)$. With this configuration, outside the model or when the model is unstressed the emergent light intensity is at a maximum. Consequently we are in the presence of a light field, and the dark fringes are given by an odd number of half wavelengths (Fig. 2.2.4b)[8].

An interesting property of certain polymers, such as epoxy is the phenomenon, called “stress freezing”. This is based on the biphasic behavior of some polymer materials when heated. These materials are composed of two types of chains whose molecules are linked together: principal chains and secondary chains. At room temperature, these two families of molecular chains resist deformation due to an applied load. However, when the temperature of the polymer increases to the critical temperature about 130°C for an epoxy, the secondary chains break and the principal chains bear the entire load. If the temperature of the polymer slowly decreases to room temperature while the load is maintained, secondary molecular chains re-form between the strongly deformed principal chains. After unloading, the principal chains recover a little of their original shape, but a considerable proportion of the deformation remains. The elastic deformation of the principal chains is permanently fixed into the material by the re-formed secondary chains. When the model has cooled, it is mechanically cut into slices of appropriate thickness so that the change in the direction of principal stress across the thickness of each slice can be considered negligible. Each separate slice is then analysed with a circular or plane polariscope. By cutting the photoelastic model into slices for three orthogonal directions, the differences in principal stresses in each direction can be determined [8, 11, 12].

The photoelasticity has been employed at the Technical University of Cluj-Napoca since 1956 under the coordination of Prof. Ioan PĂSTRĂV, the founder of the Laboratory of Optical Methods for Stress Analysis[13]. The photoelasticity was firstly applied by the author in 1996 as main investigation methods for the PhD thesis. Even only the research results after the PhD should be reported, the author included this chapter to have a comprehensive image of the optical methods of engineering analysis among them the photoelasticity has an important place. There are a plenty of papers and studies based on this method, the author solved with good results the problem of applying frozen stress technique for flexible shells of revolution with application at bellows. In the lack of information regarding scientific impact and indexing the most of the published papers during and also after the PhD has been at national and international conferences on experimental mechanics and in one monograph.

Monograph

1. **Mircea Cristian Dudescu**, (2005): *Calculul de rezistență al tuburilor ondulate*. Editura U.T.Press, Cluj-Napoca, ISBN 973-662-207-X, 160 pag.

Articles & Conferences

2. **Dudescu, M.**, (2004): *Experimental Stress Analysis in Bellows Subjected to Axial Loads*. Proceedings of the 3rd Youth Symposium on Experimental Solid Mechanics, Poreta Terme, Italy, 12-15 May, 2004, ISBN 88-901080-0-3. ([Google Scholar](#))
3. **Dudescu, M.**, Hărdău, M., (2004): *Influence of the model weight in case of photoelastic analysis of bellows subjected to axial loading*. Proceedings of the 21th Danubia-Adria Symposium on Experimental Methods in Solid Mechanics, September 29 - October 2, 2004, Pula, Croatia, pp. 24-25, ISBN 953-96243-6-3.
4. Păstrav, I., **Dudescu, M.** (2008): *Metode optice de analiză a tensiunilor utilizate în laboratoarele UTC-N*. În: A Treia Conferință Națională a Academiei de Științe Tehnice din România, Cluj-Napoca, 12-13 Noiembrie 2008, pag. 75 -83.
5. Păstrav, I., **Dudescu, M.** (2000): *Studiul experimental al tensiunilor în tuburile ondulate comprimate axial*. Al VIII-lea Simpozion National de Tensometrie, Constanța, 1-3 iunie, 2000, pag. 127-132.
6. **Dudescu, M.**, (1999): *Stress analysis in bellows subjected to axial loading*. Acta Technica Napocensis, nr. 42/1999, pag. 167-172, Editura U.T.Pres Cluj-Napoca, ISSN 1221-5872;

2.2.2. Application of photoelasticity to thin-wall structures

EXPERIMENTAL STRESS ANALYSIS IN BELLOWS SUBJECTED TO AXIAL LOADS

Analytical computation of strains and stresses in bellows designed to compensate displacements hasn't a precise mathematical solution. Complicated shape and complex loadings have determined acceptance of some simplified hypotheses which correspond in some measure to real state [14] or was necessary to complete the formulas with some coefficients of correction experimentally determined [15]. Because 3D photoelasticity was less applied to this kind of shells, an important advantage of the method is displaying the full field stress distribution. The experimental results can be directly compared with Finite Element Method (FEM).

In figure 2.2.5 is presented the epoxy resin model represented one complete 3D corrugation of a bellows [11]. The most difficult part was to construct a metallic mould and to



Fig.2.2.5. Epoxy resin model of bellows having one corrugation corresponding to inner radius

cast the epoxy resin into it. Some of bellows dimensional parameters are: interior radius $R_i = 68$ mm, exterior radius $R_e = 118$ mm, radius of curvature $R_c = 12$ mm, pitch $T = 48$ mm, wall thickness $h = 4$ mm, Young's modulus $E = 2200$ N/mm².

Axially loaded model was heated up to 100°C, kept at this temperature one hour and then cooled down slowly. After

cooling, slices of constant thickness were cut in radial and circumferential direction. A diametrically compressed disk was analysed to determine value of stress-optic coefficient for the material's model. Photoelastic patterns and isochromatic fringes order determined by Tardy compensation are presented in figure 2.2.6 corresponding to radial direction (maximum values) and in figure 2.2.7 for circumferential direction [16].

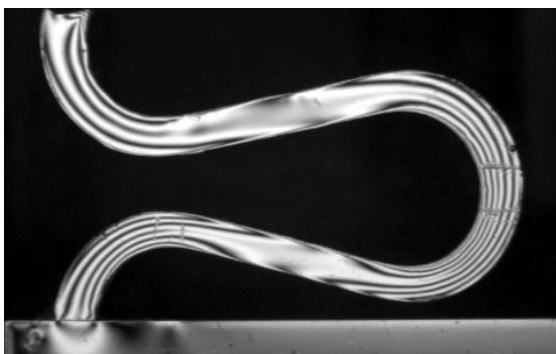


Fig. 2.2.6. Isochromatic fringe order: $k=2,9$ (inner surface), respectively $k=2,4$ for outer surface, $\sigma_0=0,0528$ N/mm²

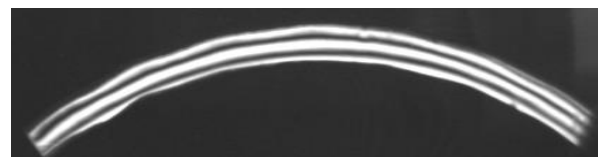


Fig. 2.2.7. Isochromatic fringe order: $k=1,6$ (inner surface), respectively $k=0,6$ for outer surface, $\sigma_0=0,0622$ N/mm²

In a similar way was analysed a model of bellows having one corrugation corresponding to exterior radius. Obtained results are presented for different loading values in tables 2.2.1 and 2.2.2. Finite element (FE) computation was performed on a 3D structure geometrically identically with epoxy resin models of bellows. In figure 2.2.8 is presented radial stress distribution corresponding to outer surface of bellows and in figures 2.2.9 & 2.2.10 radial and circumferential stress diagrams.

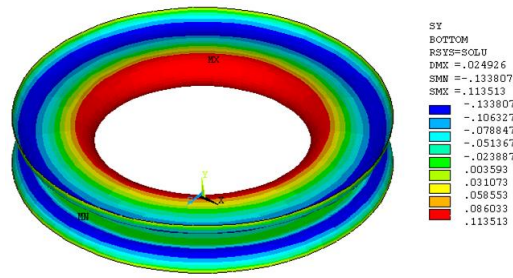


Fig.2.2.8. Distribution of radial stresses for one corrugation corresponding to inner radius

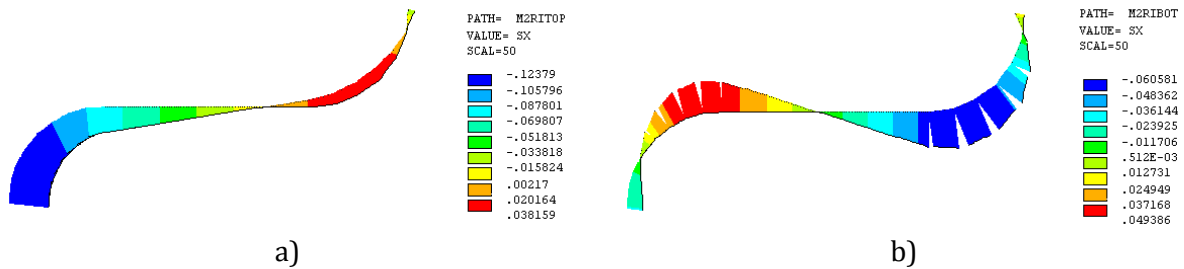


Fig. 2.2.9. Circumferential stress σ_t [N/mm²] diagrams for one corrugation of bellows axially loaded: a) outer surface, b) inner surface of bellows

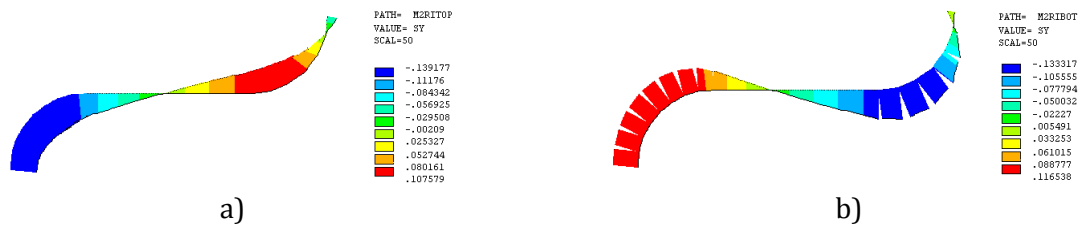


Fig. 2.2.10. Radial stress σ_r [N/mm²] diagrams for one corrugation of bellows axially loaded: a) outer surface, b) inner surface of bellows

Tables 2.2.1 & 2.2.2 present comparatively, numerical (FEM) and experimental results in terms of radial and circumferential stresses. Three resin models of bellows loaded by different axial forces (11.5 N, 12.3 N and 13 N) were used to validate the experimental results.

Table 2.2.1. Radial stresses

Radial stresses σ_r [N/mm ²] / Axial load P= 11,5 / 12,3 / 13 N									
Numerical				Relative deviatio n	Relative deviatio n	Experimental			
r → R _i		r → R _e				r → R _i		r → R _e	
Ext.	Int.	Ext.	Int.			Ext.	Int.	Ext.	Int.
-	-	0,098	-0,1057	7,5%	9,6%	-	-	0,106	-0,117
-0,137	0,113	-	-	10,4%	10,3%	-0,153	0,126	-	-
-	-	0,110	-0,1195	9%	10,1%	-	-	0,121	-0,133

Table 2.2.2. Circumferential (hoop) stresses

Circumferential stress σ_t [N/mm ²] /Axial load P= 11,5 / 12,3 /13 N									
Numerical				Relative deviatio n	Relative deviatio n	Experimental			
r → R _i		r → R _e				r → R _i		r → R _e	
Ext.	Int.	Ext.	Int.			Ext.	Int.	Ext.	Int.
-	-	0,0766	0,0089	1,1%	7,2%	-	-	0,0775	-0,0096
0,112	0,042	-	-	12,4%	12,5%	0,0995	0,0373	-	-
-	-	0,086	0,010	4,4%	5,2%	-	-	0,09015	-0,0095

Analysing the obtained stress values, a good agreement between FE analysis and 3D photoelasticity (frozen stress technique) can be noticed, that validates the experimental method for stress measurement in flexible shells and in particular in bellows subjected to axial loadings. Most difficult part of the method – casting of epoxy resin model of bellows - was overtook by using a well-designed mould and a special model extraction technique.

INFLUENCE OF THE MODEL WEIGHT IN CASE OF PHOTOELASTIC ANALYSIS OF BELLOWS SUBJECTED TO AXIAL LOADING

Application of 3D photoelastic method for bellows has been demonstrated for one corrugation model. Casting of an epoxy resin model with more corrugations will influence considerably the results because of the model own weight and procedure implied by frozen stress technique (heating up the model to 100°C)[17].

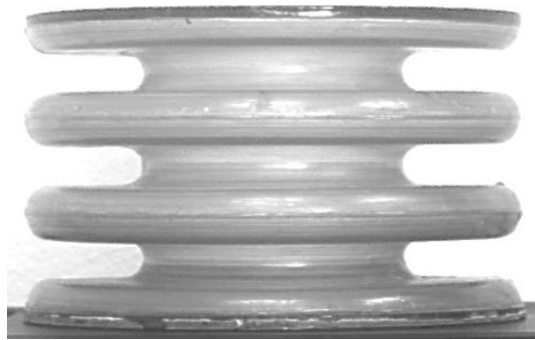


Fig. 2.2.11. Epoxy resin model of bellows with three corrugations

To analyse the above experimental effects upon the stress distribution frozen stress technique has been performed on epoxy resin model presented in figure 2.2.11 and having following geometrical parameters: inner radius $R_i=61,5$ mm, outer radius $R_e =118,5$ mm, radius of curvature $R_c=11,5$ mm, pitch $T =46$ mm, wall thickness $h=3$ mm, number of convolutions $N=3$, Young's modulus $E=2200$ N/mm² and Poisson's ratio $\mu=0,33$.

Analytical expression (2.2.3) shows dependence between work rigidity f_w of bellows [15] and its wall thickness h :

$$f_w = 1,7 \frac{D_m E h^3 n}{w^3 C_f} \quad (2.2.3)$$

where: D_m is average diameter, D_i inner diameter, n number of wall layers, $w = H - nh$, $H = R_e - R_i$ and C_f is a correction coefficient experimentally determined.

Another significant influence upon bellows work rigidity has Young modulus in case of the epoxy model. Epoxy resin has a modulus of elasticity about 10 N/mm² at 100°C (temperature necessary to “freeze” the stresses) comparatively with value of 2200 N/mm² at room temperature. In these conditions the model own weight modifies stress distribution and the deformed shape of bellows. Thus axial deformation grows gradually for first to last convolution, which is the most stressed one (Fig. 2.2.12). Slices of constant thickness in radial and circumferential directions were cut out from 3D model of bellows after stress freezing.

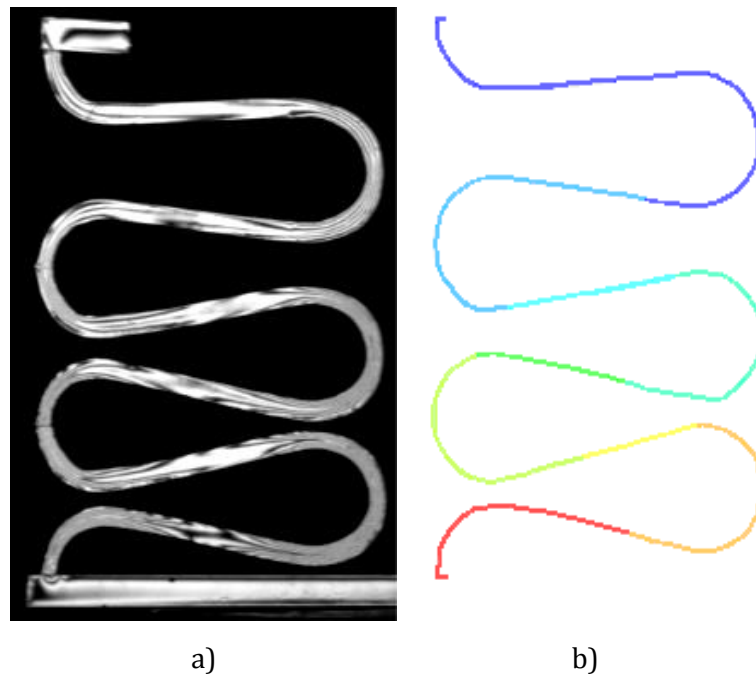


Fig.2.2.12. Axial deflection of bellows: a) experimental by 3D photoelasticity, b) numerical FEA

Using Tardy compensation were determined the isochromatic fringes order for two convolutions (Fig. 2.2.13 & 2.2.14). For the third one high number of fringes has made impossible an accurate counting.

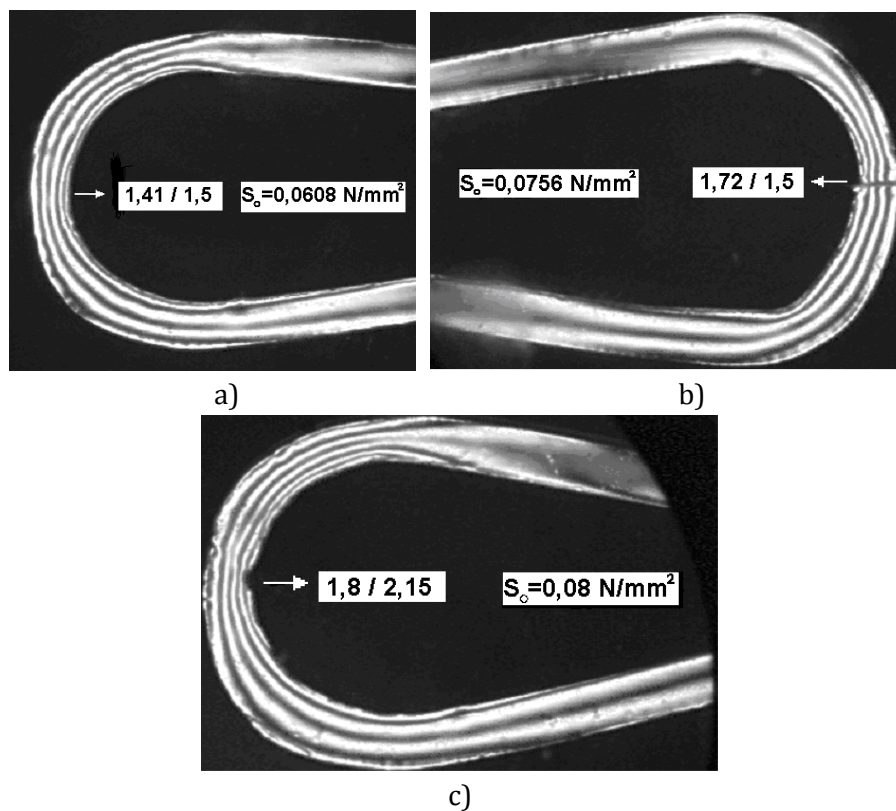


Fig.2.2.13. Isochromatics fringe order in first two convolutions to determine stresses in radial direction a), c) inner radius and b) outer radius

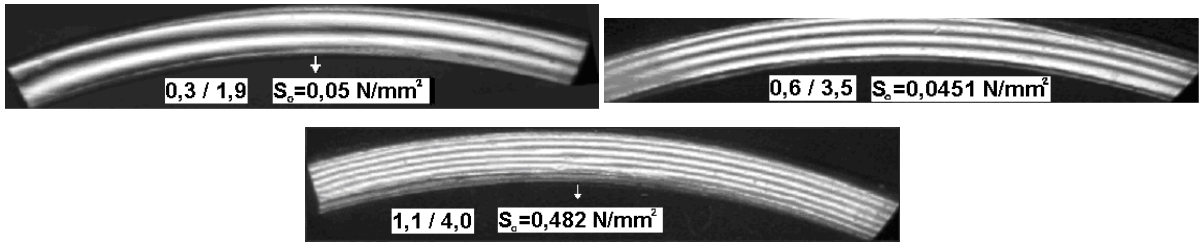


Fig.2.2.14. Isochromatics fringe order for stress computation in circumferential direction

FE calculation has been done on geometrically identically model taking into consideration epoxy resin density $\rho=1.25 \text{ kg/dm}^3$ for mass calculation. An example of stress distribution mapped on deformed bellows shape is presented in figure 2.2.15.

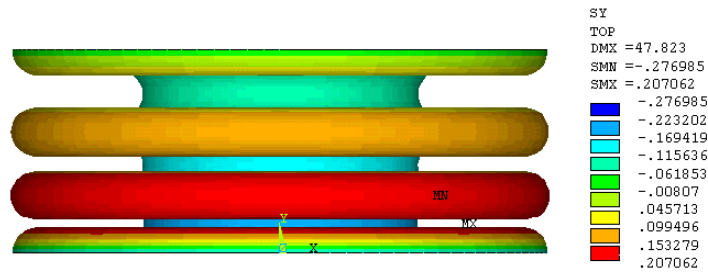


Fig.2.2.15. Radial stresses σ_r [N/mm²] distribution in outer surface of bellows axially loaded (FEA)

Comparative results in terms of radial and circumferential stresses between experimental and numerical analysis of bellows subjected to axial loading are presented in table 2.2.3.

Relative deviation is in a range of 2% to 13%, precision being affected by model casting imperfections. In case of bellows subjected to axial loading studied by 3D photoelasticity – frozen stress technique - own weight of the model is a factor that strongly influences application of this experimental technique. For a certain value of wall thickness the model will have uncontrolled deformation due to its mass, limiting the number of convolution and the applied force.

Table 2.2.3. Comparative results: experimental and numerical

3 [N]	Experimental		Numerical (FEA)		Relative deviation	
	Exterior surface	Interior surface	Exterior surface	Interior surface	Exterior surface	Interior surface
Radial stress σ_r [N/mm ²] $r \rightarrow R_i$ (inner radius)						
I	-0,091	0,085	-0,083	0,076	8,7 %	10,8%
II	-0,172	0,144	-0,152	0,140	13,3 %	2,7%
Radial stress σ_r [N/mm ²] $r \rightarrow R_e$ (outer radius)						
I	0,113	-0,128	0,108	-0,114	10,9%	4,4%
Circumferential stress σ_t [N/mm ²] $r \rightarrow R_i$ (inner radius)						
I	-0,095	0,017	-0,0918	0,0201	3,3%	15%
II	-0,148	0,027	-0,154	0,0258	3,4%	2%
III	-0,199	0,047	-0,207	0,051	3,8%	7,8%

2.3. Moiré methods

2.3.2. Introduction

In experimental mechanics, the moiré technique is defined as the utilization of the moiré patterns to measure displacements of surfaces. The basis of the moiré-pattern technique is based on the interaction of two gratings that are parallel to each other and are illuminated by a beam of coherent parallel light[8]. The state of deformation of a surface is characterized by a grating called a model grating. This grating acts as a reference element of the changes of the surface from the initial or reference state to the final or deformed state. These changes characterize the relative deformations of the studied surface. In order to determine the changes in the geometry of the model grating, the second grating or master grating is introduced. The superposition of the two gratings produces the moiré patterns (Fig. 2.3.1). The moiré patterns are formed on the image plane of the observation system.

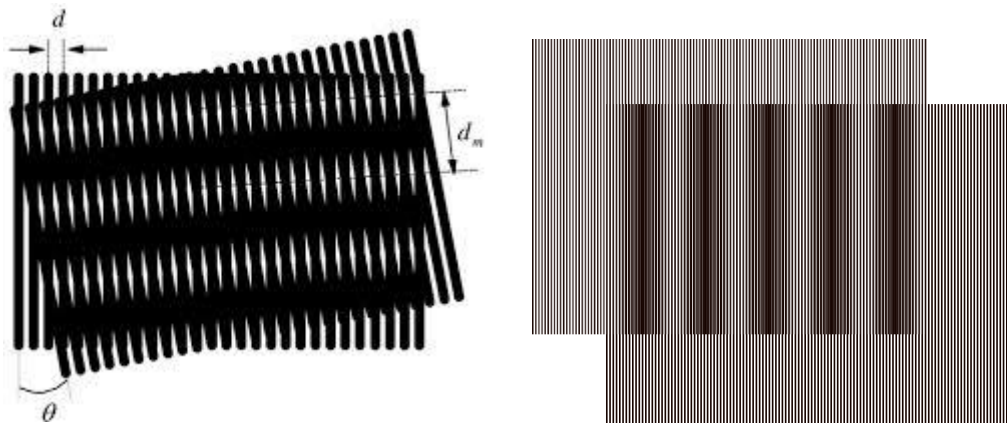


Fig. 2.3.1. Formation of moiré patterns

In order to obtain displacements or strains it is necessary to know the relationship between the model grating, the master grating, the observation system and the surface under study. This relationship depends on the particular technique utilized. Gratings can be engraved on the surface to be studied. Engraved gratings deform together with their supporting surface. The changes in geometry of the model grating provide the necessary information to determine displacements and strains of the specimen surface. Gratings can be projected on the surface to be studied. As the surface changes, the projection changes. In a diffusing surface these changes can be related to displacements with respect to a reference surface. In a reflecting surface the changes provide the slopes of the surface. Consequently, the relationship between the model and master grating depends on the particular method utilized.

There are three basic methods[8, 18]:

(a) intrinsic-moiré method or moiré method providing displacements of the points of a surface with respect to their initial position. In this method, the grating is fixed directly to the surface to be studied, thereby following all the changes experienced by the surface. The determination of the deformations of the model grating directly provides information concerning the displacements and strains of the studied surface.

(b) projection moiré, also known as shadow moiré. This method provides displacements of the points of the observed surface with respect to a reference surface.

(c) reflection moiré, providing the slopes of the surface with respect to the reference state. The discipline that deals with these three techniques and all their possible variations can be called theory of the moiré methods. The relationships between the model and master gratings in the observation plane depend only on their relative geometries.

The reflection moiré has been employed since 1970 in the former Chair of Strength of Materials from the Technical University of Cluj-Napoca as a lab work in optical methods. The shadow moiré technique was firstly applied in 1999 in a frame of a Tempus Programme together with the University of Poitiers who still develop the method in the group of experimental mechanics (Photomecanique in the Institute Pprime). There are a plenty of papers and studies based on this method [19]. The author applied the method to solve a research contract for young researchers (type AT) financed by Romanian Minister of Education and Research. Since then were published a lab work and the following papers in the proceedings of international conferences or journals:

1. Ioan Păstrav, **Mircea Cristian Dudescu** (2009): *Lucrări de laborator de metode optice de analiză a tensiunilor*. Editura U.T.Pres, Cluj-Napoca, ISBN 978-973-662-452-0, 92 pag.
2. Păstrav, I., Badea, C., **Dudescu, M.**, (2003): *Study by shadow-Moiré of the prismatic bars subjected to torsion*. Acta Technica Napocensis, nr. 46/2003, pp. 47-50, Editura U.T.Press Cluj-Napoca, ISSN 1221-5872;
3. **Dudescu, M.**, Şomotecan, M., (2007): *Application of shadow moiré method to determine the membrane characteristic*. In: Proceedings of the 24th Danubia-Adria Symposium on Developments in Experimental Mechanics, September 19-22, 2007, Sibiu, Romania, pag. 65-67, ISBN 978-973-739-456-9.
4. **Dudescu, M.**, (2005): *Application of shadow moiré method by phase shifting to membranes deformation measurement*. Proceedings of the 4st Youth Symposium on Experimental Solid Mechanics, Costracaro Terme, 4-7 May 2005, Italy, ISBN 88-901080-0-4. ([Google Scholar](#))
5. Păstrav, I., Badea, C., **Dudescu, M.** (2001): *Study by shadow-Moiré of the prismatic bars subjected to torsion*. Proceedings of the 18th Danubia-Adria Symposium on Experimental Methods in Solid Mechanics, Steyr, Austria, 2001, pp. 53-55. ([Google Scholar](#))
6. **Dudescu, M.** (2005): *Modern experimental and numerical methods to calculate membranes deformation*, In: International conference "Inter-Ing", Tg. Mureş, 10-11 Noiembrie 2005, România ([Google Scholar](#))

2.3.2. Shadow moiré principle

The shadow moiré method is based on the notion of parallax measurement. Parallax is the fundamental principle on which human sight is based and is a consequence of the fact that we have two eyes. It is also referred to as triangulation because the depth information results from the basic triangular equations of trigonometry. Another important aspect of shadow moiré is that, as is the case with intrinsic moiré, one can utilize non coherent or coherent illumination[18]. Since contouring is an important industrial tool, shadow moiré is utilized far more than the intrinsic moiré and has associated with it many industrial application developments.

The shadow moiré method for contour determination of an object relies on a master grid projection situated in front of the object illuminated by a point light source. The principle is schematically presented in Fig. 2.3.2 and the experimental set-up consists of a point light source

$$\phi = \frac{2 \cdot \pi \cdot z}{p} \left(\frac{x}{h_1 + z} + \frac{b-x}{h_2 + z} \right) \quad (2.3.6)$$

Usually the light source and the observation point are situated in the same plane, parallel with the master grid plane, thus $h_1=h_2=h$, and the equation (2.3.6) can be simplified as follows:

$$\phi = \frac{2 \cdot \pi}{p} \cdot \frac{b \cdot z}{h + z} \quad (2.3.7)$$

If the distance z between the object and the master grid is much shorter than distance h between the light source and grid ($z \ll h$), the value of z in the denominator can be neglected:

$$\phi = \frac{2 \cdot \pi}{p} \cdot \frac{b \cdot z}{h} \quad (2.3.8)$$

The distance z between the object and the master grid is obtained as:

$$z = \frac{\phi}{2 \cdot \pi} \cdot \frac{p \cdot h}{b} \quad (2.3.9)$$

Expressing the extinction condition $\phi = 2k\pi$ results the equation of the level curve (contour line) with the fringe order or contour line number k . Level difference Δz between two successive level curves is calculated replacing $k=1$.

$$\Delta z = \frac{ph}{b} \quad (2.3.10)$$

where Δz is called sensitivity coefficient of the set-up and can be easily determined knowing the grid's pitch and the distances light source - master grid h and light source - measured object b respectively.

Replacing Δz in the equation (2.3.8) results:

$$\phi = 2 \cdot \pi \cdot \frac{z}{\Delta z} \quad (2.3.11)$$

The above equation permits precise determination of Δz . Thus, moving the master grid with a known value d the number n of fringes passing through a point of the object can be counted.

Replacing $\phi = 2k\pi, k = n$ and $z = d$, result:

$$\Delta z = \frac{d}{n} \quad (2.3.12)$$

Determination of the displacement w of a point belonging to the object and through a fringe of k order is passing can be done with the formula:

$$w = k \Delta z \quad (2.3.13)$$

The sensitivity of shadow moiré method above described used for contour determination of the objects is relatively reduced and it is mainly influenced by the pitch of the master grid, the measurement precision is about 0.1 mm. A fine master grid having a high density of lines per millimeter is limited by the optical diffraction and the diameter of the light source. The method is successfully applied for big objects relative to the grid's pitch and having a relevant contour changes. A significant improvement of the measurement precision and sensitivity respectively, can be obtained by applying the phase shifting procedure. Introducing phase shifting method the accuracy comparatively with the classical shadow moiré will increase ten times up to 0.01 mm.

2.3.3. Shadow moiré by phase shifting method

Application of the phase shifting method presumes the optical analysis of the moiré phenomena as presented in Fig. 2.3.2. Considering the sinusoidal representation of the light given by equation (2.3.1) a light ray from the source S that pass the grid in point x_1 and rich the point M belonging to the object surface and situated at distance x . The reflected light from this point pass the grid in point x_2 and arrives in the observation point O . The light intensity in point O is given by the equation (2.3.2). In practice the observer and the light source are consider in the same plane parallel with the master grid plane. Replacing the phase value ϕ from equation (2.3.7), the equation (2.3.3) can be written as:

$$I(O) = H(M) \left[1 + \frac{1}{2} \cos 2\pi \frac{z}{\Delta z} \right] \quad (2.3.14)$$

Phase shifting methods require many phase-shifted images for the same fringe pattern. There are different methods to get phase shifting, but the real problem in shadow moiré is to introduce phase shift $\delta\phi$ between the different fringe patterns[21]. To change the phase from ϕ to $\phi + \delta\phi$ in equation (2.3.7) can be achieved only by modification of four parameters b , h , p and z , leading respectively to phase shifts $\delta\phi_b$, $\delta\phi_h$, $\delta\phi_p$ and $\delta\phi_z$, given by the following relationships:

$$\delta\phi_b = \frac{2\pi}{p} \cdot \frac{z}{(h+z)} \delta b \quad (2.3.15)$$

$$\delta\phi_h = -\frac{2\pi}{p} \cdot \frac{b \cdot z}{(h+z)^2} \delta h \quad (2.3.16)$$

$$\delta\phi_p = \frac{2\pi}{p^2} \cdot \frac{b \cdot z}{(h+z)} \delta p \quad (2.3.17)$$

$$\delta\phi_z = \frac{2\pi}{p} \cdot \frac{b \cdot h}{(h+z)^2} \delta z \quad (2.3.18)$$

where b is transformed in $b + \delta b$, h in $h + \delta h$, p in $p + \delta p$ and z in $z + \delta z$ respectively.

It can be seen that the phase shiftings depend on distance z . This means the fringe pattern cannot be uniformly phase shifted whatever is the chosen parameter. Practically the phase shifts given by equations (2.3.15 to 2.3.18) correspond to move the light source or the observer (parameter b), to move the light source and the observer (parameter h), to change the master grid line spacing (parameter p) or to move the object perpendicularly to the master grating plane (parameter z). From equations (2.3.15 to 2.3.18) it can be obtain the amplitude of the variation made on each parameter in function of the suitable phase shift $\delta\phi$.

The variation of phase shift is almost the same if the parameters b , h or p are changing[22], thus it is not possible to use any modifications of these parameters. The phase shift is almost constant on all depth of the object by translating the object perpendicularly from the master grating, this can be the only solution to reliable change the phase. This corresponds to a translation of δz leading to a phase shift, in practice considering $z \ll h$, the equation (2.3.18) becomes:

$$\delta\phi_z = 2\pi \frac{b}{ph} \delta z \quad (2.3.19)$$

In this relationship, the parameter z doesn't appear and the phase shift is the same anywhere. Concluding, it can be consider that moving of the object with a certain distance with respect to

the master grating is a good way to shift phase. In the general case, the error made on the phase shifts is around a few degrees (under 5° for z values between 0 and 20 mm)[22].

Phase shifting methods require many phase-shifted images for the same fringe pattern. The method that can be used is the translation of the object. Using the FFT (Fast Fourier Transformation) of each fringe pattern it is possible to solve the problem of non-constant phase shifts. The phase ϕ is determined from three images taking into account the intensities I_0 , I_1 and I_2 of each fringe pattern by:

$$\tan \phi = \frac{(I_2 - I_1) + (I_0 - I_2)\cos\phi_{10} + (I_1 - I_0)\cos\phi_{20}}{(I_1 - I_2)\sin\phi_{10} + (I_1 - I_0)\sin\phi_{20}}, \quad (2.3.20)$$

where $I_0(x, y)$, $I_1(x, y)$, $I_2(x, y)$ represents the grey level in the point of coordinate (x, y) , $\phi(x, y)$ is the phase in the same point (x, y) , $\phi_{10} = \phi_1 - \phi_0$, $\phi_{20} = \phi_2 - \phi_0$ are the phase shifts between images 2-1 and 3-1 respectively.

This relationship is always valuable even if the phase shift values are not equispaced on the trigonometric circle. Since this quantities should be known with the highest possible accuracy a procedure based on FFT algorithm can be used for each image in order to extract the main harmonic. The phase value can be calculated as:

$$\tan \varphi_k = \frac{\text{Im}_k}{\text{Re}_k} \quad k = 0, 1, 2 \quad (2.3.21)$$

where Im_k represents the imaginary part and Re_k is the real part of the first peak in the FFT for the k^{th} image. Through this procedure the phase shifts are obtained with a precision between 0.1 to 2 degrees.

Usually a shadow moiré fringe pattern recorded on the surface of an object has a few number of fringes which are not equidistant. In this condition it is very difficult to apply the FFT procedure to accurately determine the phase shift between images. In practice it is preferable to use an inclined plane on which numerous fringes appear with a constant pitch. This witness plate which is attached to the object support is submitted to the same phase shifts. The measurement principle is presented in figure 2.3.3. The dot white light source projects the shadow of the master grating. This grating is fixed while the object is mounted on a translation moving stage.

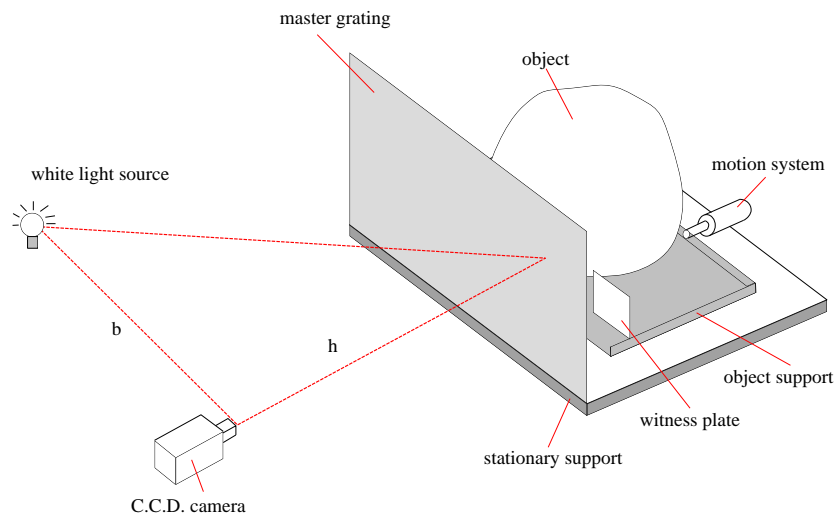


Fig. 2.3.3. Experimental setup for shadow Moiré by phase shifting method

In all applications the distance z between the object and master grating is considered negligible with respect to distance h between object and observation point (CCD camera), thus the equation (2.3.7) becomes:

$$\phi = \frac{2\pi}{p} \cdot \frac{bz}{h} = 2\pi \frac{z}{\Delta z} \quad (2.3.22)$$

where Δz is the sensitivity ratio of the experimental set-up.

This relationship shows the linearity between the distance z and phase value ϕ . The sensitivity ratio can be accurately evaluated by counting the number n of fringes which pass in a fixed point as the object is displaced by a quantity d :

$$\Delta z = \frac{d}{n} \quad (2.3.23)$$

By this way is not necessary to know the geometrical parameters b , h or p . The object is than motioned of around $\Delta z/3$.

After phase calculation a classical unwrapping algorithm must be applied to get the contour or the displacement between two loading stages. Phase values are between $-\pi$ and π , but for simplicity this is translated in the interval $[0; 2\pi]$ obtaining so called phase *modulo* 2π :

$$\phi_{\text{modulo } 2\pi} = \begin{cases} \phi + 2\pi & \phi < 0 \\ \phi & \phi > 0 \end{cases} \quad (2.3.24)$$

In the computer image processing the phase is represented by grey values between 0 (black) and 256 (white), thus an 8 bit colour depth (Fig. 2.3.4a). A diametric profile shows the saw-teeth aspect of the modulated phase, with jumps of 2π (Fig. 2.3.4b). To get a continuous phase distribution an unwrapping procedure is necessary, the discontinuities being eliminated by addition of an integer value of 2π (Fig. 2.3.4c, d)[23]. Also is necessary to determine the magnification of the optical system to transform the phase of a certain point from radians in length units (mm).

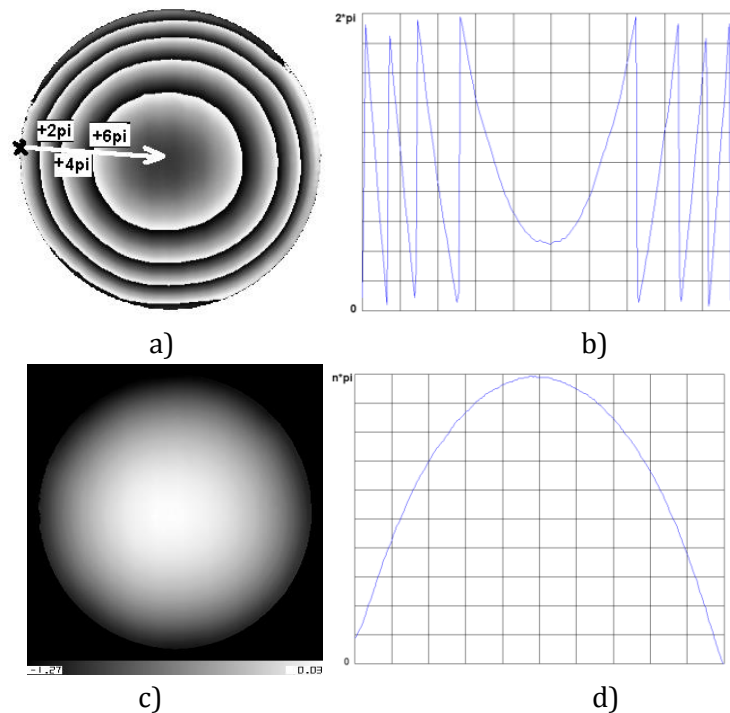


Fig. 2.3.4. a) Phase modulo 2π ; b) vertical profile of modulated phase; c) unwrapping; d) vertical profile of unwrapped phase.

2.3.4. Membranes analysis by shadow moiré technique

It is known that thin membranes undergoing high deformations comparatively with their thickness with a nonlinear behavior, their stiffness increase significantly with the applied load. For this case the theory offers only an approximate solution which is restricted to a circular membrane shape. An exact solution implies knowing of the membrane surface equation, which is difficult to be evaluated, the equation degree modifies with the applied load (pressure).

Considering a clamped plate with constant thickness h , undergoing uniform pressure p , the maximum deflection w_0 can be expressed[24]:

$$w_0 = 0,662 \cdot R \cdot \sqrt[3]{\frac{pR}{Eh}} \quad (2.3.25)$$

where: R is the membrane's radius, p applied pressure, E Young's modulus, h membrane's thickness, and value of Poisson's ratio equals 0.3.

Shadow moiré method is a known optical method for deformations analysis. Application of classical method to calculate displacements using level curves can be applied successfully if the desired accuracy is about 0.1 mm. Study of the thin membranes having large deformations isn't enough accurate by this method. If the phase shifting techniques is combined with shadow Moiré the accuracy increase ten times (up to 0.01 mm). The experimental measuring set-up based on shadow moiré principle is presented in figure 2.3.5[25, 26] .

The white light source projects the master grid with a pitch of 0.5 mm upon the analysed object (an aluminium circular membrane with thickness $h=0.14$ mm and radius $R=60$ mm). The master grid is fixed and the object can be moved with a micrometric screw. If the object is observed through the master grid it can be seen the level curves relative to the grid plane. The interference fringes captured with a CCD camera were digitized with a frame grabber having a resolution of 512x512 pixels and 8 bit colour depth.

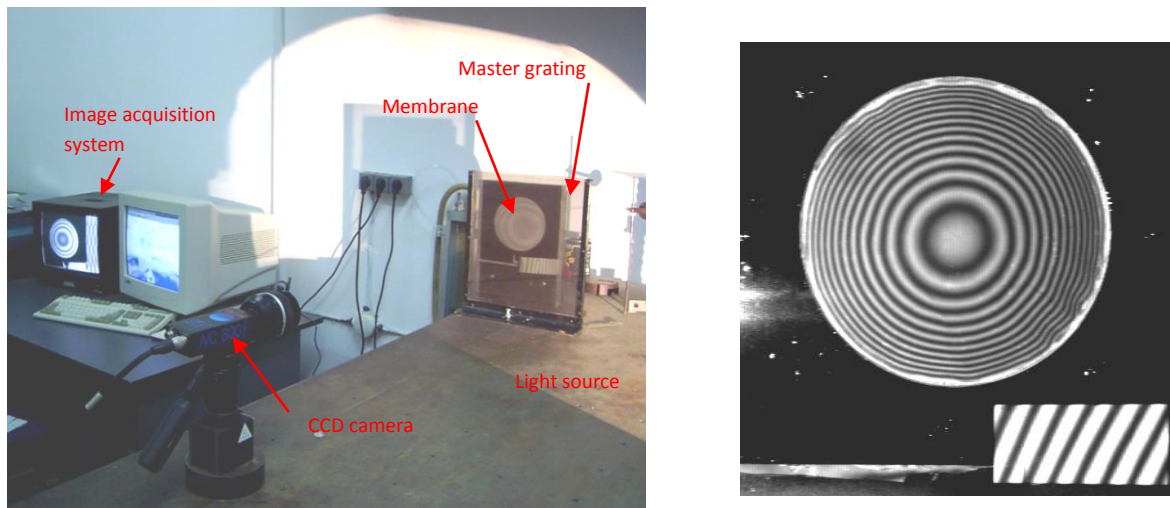


Fig. 2.3.5. Experimental set-up and level curves on pressurized membrane

Near the object is placed a small witness plate necessary to accurate evaluation of the phase value between the shifted images. The computation was performed using OMBRE software developed by University of Poitiers, France[27].

Loading of the membrane was done with a small pump, applied pressure being measured with a calibrated glass tube in millimeters of water column (mmH₂O). To automatically compute the membrane's relief (deformed shape) three images of the level curves (Fig. 2.3.6a, b, c)

phase-shifted with 0° , 120° and 240° are necessary. The software computes the phase distribution (Fig. 2.3.6d) and demodulates it (unwrapping). Introducing the set-up geometrical parameters (master grid pitch, distances between light source and CCD camera and light source to master grid) and correspondence pixels to mm, the relief (deformation values with respect to the reference plane) of the membrane can be obtain (Fig. 2.3.6.e). The data are represented as grey values or can be exported and represented with mapping software (Fig. 2.3.6f).

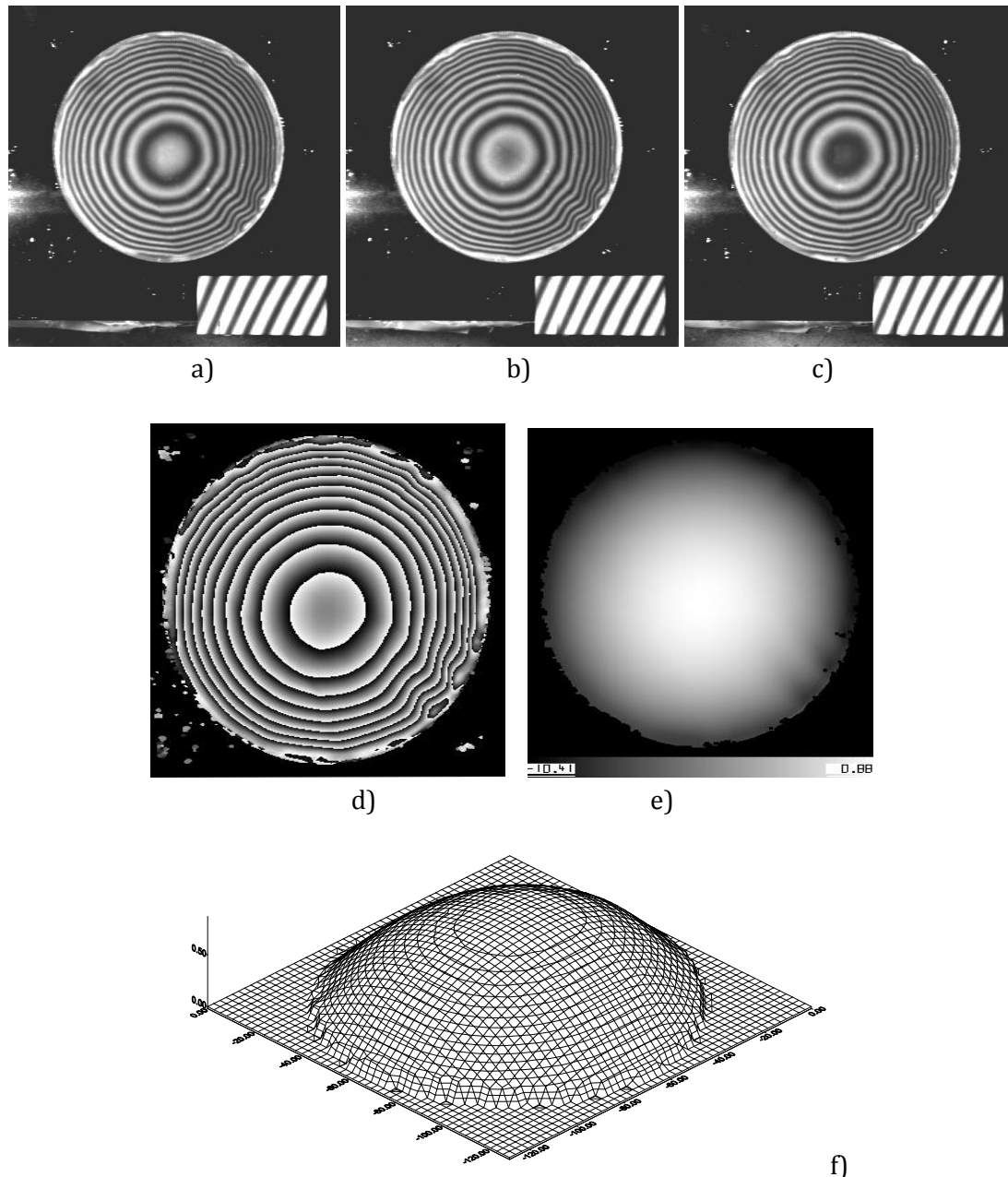


Fig 2.3.6. Phase shifting principle: a), b), c) images of the level curves 120° phase-shifted; d) phase map; e) unwrapped phase; f) measured membranes relief (contour)

To plot the membrane's load-deformation curve six measuring steps were performed. The maximum pressure was limited by the pressure measuring device (glass tube) and the number of level curves which can be accurate resolved by the computation software. The experimental

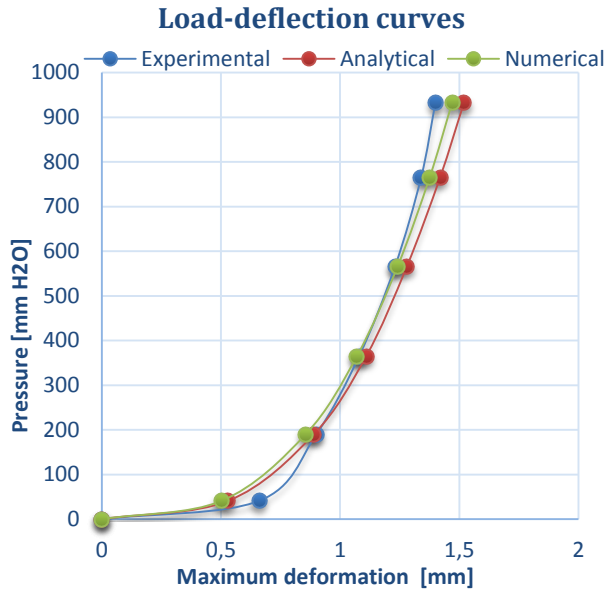


Fig. 2.3.7. Comparative results for the membrane's load-deformation curve

results at very low pressure (< 50 mm H₂O) were affected by initial membrane shape which wasn't plane due to technical difficulties to stretch it in the loading device. For pressure values higher than 100 mm H₂O (9.8E-04 N/mm²) the effect disappears and do not influence anymore the results. For numerical (FEM), analytical and experimental studies the membrane load-displacement curves are presented in figure 2.3.7.

Application of shadow Moiré method by phase shifting technique proved to be a reliable experimental method to analyses the membranes deformations. It can be noticed a relative small deviation (< 5%) between experiment and FEM method.

The obtained results consist of start point for further investigations of membranes with complex shape or approximate known of the material constants.

2.3.5. Study by shadow moiré method of prismatic bars subjected to torsion

The study presents shadow moiré method to solve torsion problems of bars with arbitrarily cross sections using membrane analogy. Method was applied for a bar with circular cross section with and without key slot[28].

The Saint-Venant method to solve problem of torsion for bars having arbitrarily cross-section consists to find a stress function $\Phi(x, y)$, which satisfies the Poisson equation

$$\frac{\partial^2 \Phi}{\partial x^2} + \frac{\partial^2 \Phi}{\partial y^2} = -2G\theta \quad (2.3.26)$$

and boundary condition

$$\Phi(x, y) = const \quad (2.3.27)$$

Where G is shear modulus and θ angle of twist.

In this case the shear stresses can be expressed by

$$\tau_{xz} = \frac{\partial \Phi}{\partial y}, \quad \tau_{yz} = \frac{\partial \Phi}{\partial x} \quad (2.3.28)$$

It was noticed that exact function corresponding to a certain section can be determined only in simple cases.

For arbitrarily cross-sections Prandtl has proposed membrane analogy. It is known that differential equation of a perfect stretched membrane is

$$\frac{\partial^2 z}{\partial x^2} + \frac{\partial^2 z}{\partial y^2} = \frac{q}{\sigma \cdot \delta} \quad (2.3.29)$$

Where q is applied pressure, σ uniform stress and δ membrane thickness.

In case that

$$\frac{q}{\sigma \cdot \delta} = -2G\theta, \quad (2.3.30)$$

equation (2.3.29) becomes identically with (2.3.26).

Membrane analogy method to solve the problem of twisting of prismatic bars is limited by the difficulty to reconstruct the membrane's deformed surface, which represents the stress function in Saint-Venant's solution.

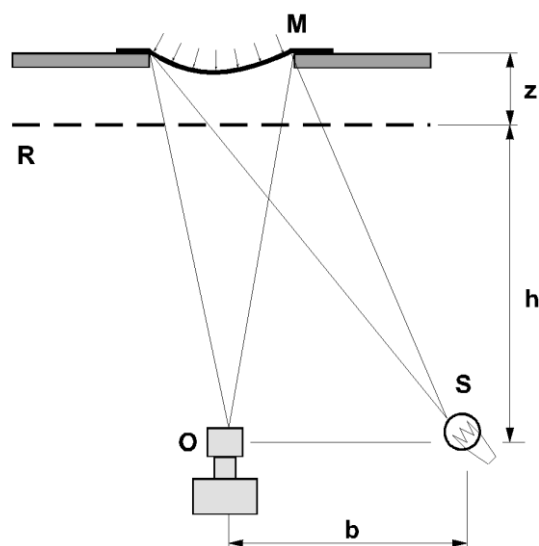


Fig. 2.3.8. Shadow moiré set-up to analyze membranes

The shadow moiré proved to be the most suitable method to solve this problem. It was utilized the set-up shown in figure 2.3.8, consists of a dot light source S , a grating with parallel lines drawn on transparent support R , a thin stretched membrane M on a hole having the contour identically with analyzed cross section and subjected to a constant internal pressure, and a CCD camera situated in the point of observation O . Superimposing grating image and its shadow moiré fringes occur on the analyzed object.

Results consist of level curves plotted in figure 2.3.9 and correspond to a bar having circular cross-section (Fig. 2.3.9a) and with a key slot (Fig. 2.3.9b).

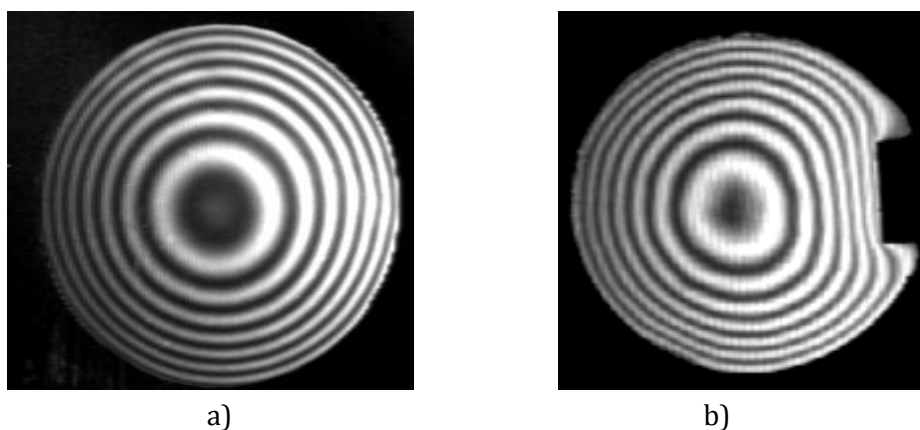


Fig. 2.3.9. Level curves on the pressurized membrane for analogy with: a) bar with circular cross section; b) bar with circular cross section with a key slot

The set-up sensitivity (level difference between two consecutive shadows) is given by

$$\Delta z = \frac{p \cdot h}{b} \quad (2.3.31)$$

where p is grating pitch, h distance from the light source plan to master grating and b distance between light source and CCD camera.

The sensitivity can be more precisely determined moving the master grating by a known amount d and countering the level curves that pass through a certain point, with the relationship

$$\Delta z = \frac{d}{n} \tag{2.3.32}$$

where n is the number of level curves that pass for a movement with d of the master grating.

With these elements is possible to reconstruct the membrane shape, which represents stress function $\Phi(x, y)$. Computation should be performed manually by representing stress function in ZOY or YOZ plane using levels curves and calculate first and second derivate, and volume V between base plane XOY and membrane surface. With these elements can be determined twisting moment $M_t = 2V$ and stresses τ_{xy} and τ_{zx} .

Using computer software Ombre V 2.1 [27] based on phase shifting method the membrane surfaces can be reconstructed (Fig. 2.3.10). For phase shifting method are necessary 3 images obtained by grating movements.

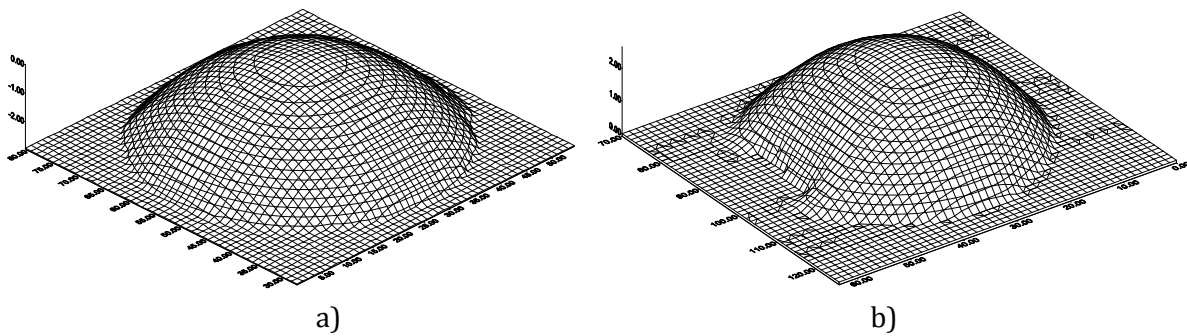


Fig. 2.3.10. Membranes reconstructed surfaces by shadow moiré technique for analogy with: a) bar with circular cross section; b) bar with circular cross section with a key slot

After computation were determined polar moment of inertia and polar section modulus. Relative deviation about known formulas for torsion of circular bars was 5% and 6%, respectively. Based on shape information a numerical derivative can be computed [29] obtaining full-field distribution of shear stresses (Fig. 2.3.11).

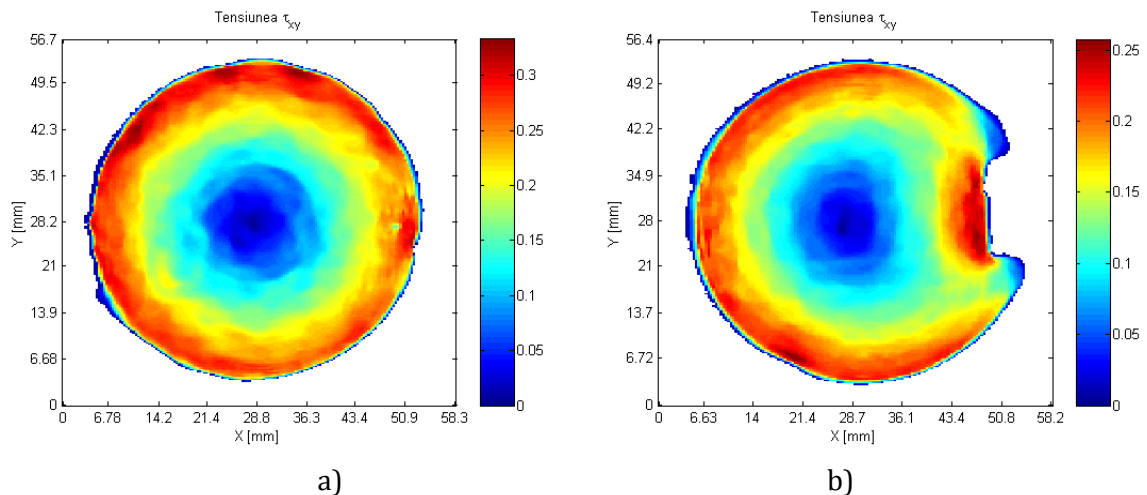


Fig. 2.3.11. Full-field distribution of shear stress in a bar subjected to torsion: a) circular cross section; b) circular cross section with a key slot

2.4. Electronic Speckle Pattern Interferometry (ESPI)

2.4.1. Introduction

With its nearly 40 years of existence, speckle interferometry (SI) has become a complete technique, widely used in many branches of experimental mechanics. A huge amount of scientific literature pertaining to SI is currently available, very rich in both theoretical and practical considerations [30-33]. Referring to the number of recent well-attended international conferences including in their programs SI techniques as a major topic (as e.g. "Speckles, from Grains to Flowers, 2006, Nimes, France), the research and application fields are by no means exhausted. Being an established technique, SI can be practiced using turnkey systems or self-made set-ups, offered on the vast quality equipment and components market.

Speckle interferometry can be looked at from no less than four points of view: the statistical, optical, mechanical and processing points of view, each reflecting a particular center of interest [30]. As an interferometric method, the sensitivity of SI is basically of 2π per λ optical path change. Taking in account the existing fringe interpolation techniques, the displacement measurement range and the displacement resolution are thus of the order of 10 nm to 10 μ m and 10 nm per loading step respectively. These characteristics are very well adapted to the general requirements of experimental mechanics, a great number of mechanical phenomena occurring at this scale. As an imaging technique based on photoelectric arrays, millions of points can be interrogated simultaneously, each pixel acting a priori as an independent detector. The overall performances of SI in spatial, temporal and measurement resolutions are thus exceptionally high, only challenged by classical holographic interferometry[30].

Tied to the intrinsic properties of SI, the photo-electric technology introduces many advantages: real-time visualization, high radiometric sensitivity, simplicity, robustness, no consumables and low cost. Its connection with computer and digital image processing is considerably developed and the future in these domains can only be still brighter. With its innumerable arrangements and not requiring specific surface preparations, SI counts an impressive set of variants, showing extreme flexibility and the possibility to choose multiple displacement sensitivities, both in the nature and the magnitude of the components.

Even if very high spatial resolution recording media are avoided, SI is nonetheless an interferometric technique and, except for the object deformation, no perturbation likely to change the optical path lengths between the two arms of the interferometer by more than a fraction of the wavelength during the exposure time should intervene. This is an obvious requirement when the aim is to measure displacements with a resolution in the nanometric range. The list of mechanical applications of SI is impressively long [33].

The future of speckle interferometry is essentially dependent on the needs and expectations of experimental mechanics. Now, there are many signs that the demand is strongly up. SI can certainly take advantage of this favourable orientation of experimental mechanics. Structural and material property identification, modelling assessment, residual stress, rheology, damage and ageing are in particular the sub-fields where SI looks likely to become a standard tool. The next chance of SI is in its very constitution: it is naturally boosted by the continuous progress of electronic imaging and digital image acquisition and processing. SI remains open to significant improvements, in particular in the sense of becoming a genuine adaptive method, efficient against external perturbations, thanks to the rapid development of phase modulators. Continuous progresses in speed, independence from the operator, reliability, made on the side

of the processing of the acquired patterns are very encouraging. The strong increase of the volume of recorded data allowed by present-day computers, when supplemented by clever data reduction methods, considerably extends the applicability of SI[30].

The author took its first contact with the method at the beginning of 2001 as a research fellow in a company that produces optical measurements systems based on ESPI. A second stage abroad (Chemnitz University of Technology, Germany) has been dedicated to developing of in house ESPI 2D measuring system. Since then were published one book and several papers in the proceedings of international conferences or journals. It has to be noticed that [34] is the most cited paper from the author's publication list (22 citations according to [Google Scholar](#)).

Monograph

1. **Dudescu, M.C.** (2010): *Introducere în interferometria electronică granulară*. Editura Risoprint, Cluj-Napoca, ISBN 978-973-53-0291-7, 164 pag.

Articles & Conferences

2. **Dudescu, C.**, Naumann, J., Stockmann, M. and Steger H. (2011): *Investigation of Non-linear Springback for High Strength Steel Sheets by ESPI*. STRAIN - International Journal of Experimental Mechanics, Blackwell Publishing, UK, Vol. 47, Issue Suppl.2, pp. 8-18, DOI: [10.1111/j.1475-1305.2009.00729.x](#).
3. **Dudescu, M.**, Naumann, J., Stockmann, M., Nebel, S., (2006): *Characterisation of Thermal Expansion Coefficient of Anisotropic Materials by ESPI*. STRAIN - International Journal of Experimental Mechanics, Blackwell Publishing, UK, Vol. 42, Issue 3, August 2006, pp. 197-206, DOI: [10.1111/j.1475-1305.2006.00271.x](#).
4. **Dudescu, M.**, Hărdău, M., (2007): *Strain-stress analysis by Electronic Speckle Pattern Interferometry*. Acta Technica Napocensis, nr. 50/2007, pp. 17-20, Editura U.T.Press Cluj-Napoca, ISSN 1224-9106.
5. **Dudescu, M.C.**, Stockmann, M., Naumann, J. (2012): *Optical measurement of the strain-stress response during unloading of metal sheets undergoing large plastic deformations*. In: 11th Youth Symposium on Experimental Solid Mechanics, 30th of May 2012 – 2nd of June 2012, Brasov, Romania, ISBN [978-606-19-0078-7](#).
6. **Dudescu, M.C.** (2011): *Measurement of materials proprieties by electronic speckle pattern interferometry*. In: 10th Youth Symposium on Experimental Solid Mechanics, 25-28 May 2011, Chemnitz, Germany ([Keynote lecture](#)) ISBN 978-3-941003-34-7.
7. **Dudescu, M.** (2010): *Optical methods in experimental mechanics*. In: Humboldt-Kolleg Cluj 2010, Förderung der Nachhaltigen Entwicklung im Donauraum durch Kulturelle und Wissenschaftliche Zusammenarbeit, 23-26 Mai, Cluj-Napoca, Romania, pp. 316-322, ISBN 978-97-713-276-5 (*oral presentation*).
8. Naumann, J., Stockmann, M., Nebel, S., **Dudescu, M.** (2007): *Measurement of the thermal expansion coefficient of carbon fibre composites by ESPI*. În: Proceedings of the 24th Danubia-Adria Symposium on Developments in Experimental Mechanics, September 19-22, 2007, Sibiu, Romania, pp. 85-87, ISBN 978-973-739-456-9.
9. **Dudescu, M.**, Naumann, J., Stockmann, M., Nebel, S., (2006): *Measurement of Thermal Expansion Coefficient of Anisotropic Materials by ESPI*. DANTEC Dynamics, 13th International User Meetings and Conference, 10-12. October 2006, Ulm, Germany, ISBN 3-00-019900-4 (*oral presentation*).
10. Nebel, S., Naumann, J., Stockmann, M., **Dudescu, M.**, (2006): *Experimental Investigation of the Thermal Expansion Behaviour of Composite Materials using ESPI*. Xth Bilateral German/Czech Symposium „Advances in Measurement Techniques and Experimental Methods in Engineering Research and Practice”, Gummersbach-Niedersessmar, 2-5 May 2006, Germany.
11. Siebert, Th., Ettemeyer, A., **Dudescu, M.**, (2002): *Integration of deformation and contour measurement with 3D-ESPI*. Proceedings of the 19th Danubia-Adria Symposium on Experimental Methods in Solid Mechanics, September 25-28, 2002, Polanica Zdrój, Poland, pag. 68-69, (*oral presentation*).

2.4.2. Electronic Speckle Pattern Interferometry principle

The principle of speckle-interferometry uses the ability of laser light for interference [35]. The object to be analyzed is entirely illuminated with laser light. The image of the object is recorded by a video camera. The light waves which are reflected by single points on the object's surface interfere and produce a so called speckle pattern. This represents the micro-structure of the object's surface in combined form. This speckle pattern is superimposed by reference light, by a different measuring technique. The interference between the reference light and the speckle pattern produces a new speckle pattern which defines a position of interest on the object's surface. This speckle pattern is stored in the image processing computer as reference image. When the object is moving, the speckle pattern is changing. By comparison with the reference pattern, correlation fringes are produced which represent the displacement respectively deformation component of the object's surface in the measuring direction which is defined by the applied measuring technique[36].

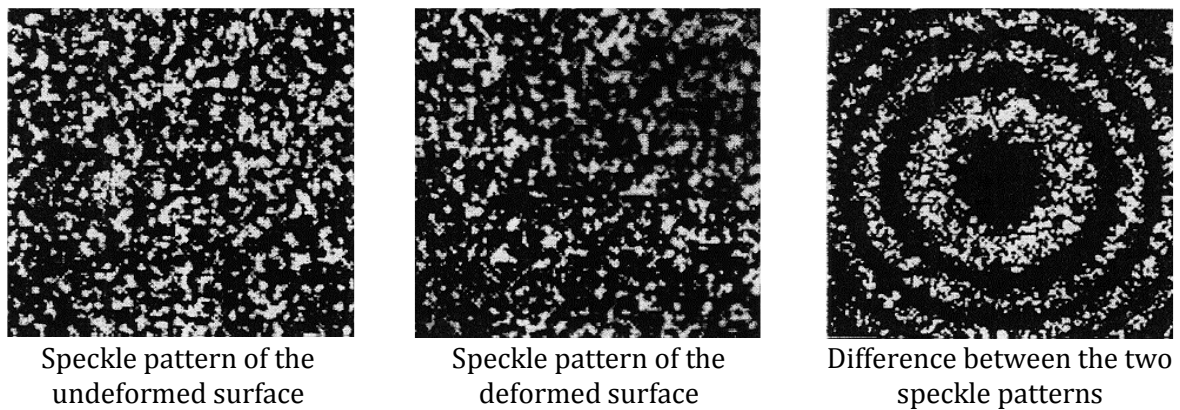


Fig.2.4.1. Electronic Speckle Pattern Interferometry principle

Speckle interferometers can be divided into two categories depending on whether two speckle fields (e.g. in-plane and shearing interferometry) or one speckle field and a reference beam (e.g. out-of-plane interferometry) are superimposed to form the interference pattern[35].

Principle of the dual illumination method

With the dual illumination method, the speckle pattern is produced by simultaneous illumination of the sample with two laser waves directed symmetrically to the observation direction (Fig. 2.4.2). The laser beam is split in two beams at an angle of 2θ using a beam splitter (e.g. diffraction grating). These two object beams generate their own speckle patterns which are added coherently and form a resulting subjective speckle at the detector of a CCD camera. The interference intensity in this speckle pattern is given by

$$I_1(x, y) = I_0(x, y) + I_M(x, y)\cos\phi(x, y), \quad (2.4.1)$$

where $I_0(x, y)$ is the background intensity, $I_M(x, y)$ is the intensity modulation of the speckle interference pattern, $\phi(x, y)$ is a random phase and (x, y) are the spatial co-ordinates in the reference frame of the image.

Deformation of the object changes the relative phase $\phi(x, y)$ of the interference patterns, thus another speckle pattern is formed and the intensity recorded in the deformed state becomes

$$I_2(x, y) = I_0(x, y) + I_M(x, y) \cos(\phi(x, y) + \Delta\phi(x, y)), \quad (2.4.2)$$

where $\Delta\phi(x, y)$ is the phase change caused by the deformation. Subtraction of the actual intensity $I_2(x, y)$ from the stored intensity $I_1(x, y)$ by image processing produces the real-time correlation fringes distribution[37], according to Equation

$$\Delta I(x, y) = |I_2(x, y) - I_1(x, y)| = \left| 2I_M(x, y) \cdot \sin\left(\phi(x, y) + \frac{\Delta\phi(x, y)}{2}\right) \cdot \sin\frac{\Delta\phi(x, y)}{2} \right|, \quad (2.4.3)$$

where $\sin(\phi(x, y) + \Delta\phi(x, y)/2)$ represents the speckle noise with random variation.

Equation (2.4.3) describes the modulation of the high frequency noise by a low-frequency interference pattern related to the phase difference term $\Delta\phi(x, y)$.

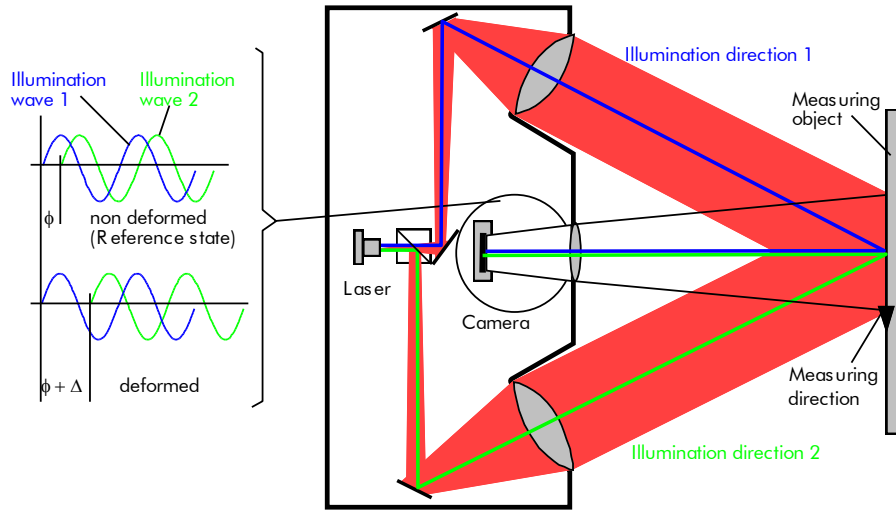


Fig.2.4.2. Principle of the dual illumination method

For such a double illumination arrangement, correlation fringes represent contours of equal in-plane displacement component parallel to the plane containing the two illumination beams. The phase change $\Delta\phi(x, y)$ is related to an object movement in the direction of the sensitivity vector \underline{S} ($\Delta\phi = \underline{S} \cdot \underline{u}$). It can be shown[35],[38] that the resultant sensitivity component for an in-plane arrangement (Figure 1) is given by

$$\underline{S} = (S_x, 0, 0)^T, \quad S_x = \frac{4\pi}{\lambda} \sin \theta, \quad (2.4.4)$$

where θ is the illumination beam's angle of incidence to the surface normal.

Measurement of the in-plane component u_x requires that the illumination beams are arranged parallel to the x - z plane. The presence of the term $\sin \theta$ in Equation (2.4.4) enables changing the in-plane sensitivity by modifying the illumination direction. The displacement can be calculated when the phase change $\Delta\phi(x, y)$ is known according to the formula

$$u_x(x, y) = \Delta\phi(x, y) \cdot \frac{\lambda}{4\pi \sin \theta}. \quad (2.4.5)$$

By counting the number (N) of fringes at every object point, the deformation of the object's surface in fractions of the laser wavelength is obtained. The measuring direction is orthogonal to the viewing direction in the plane which is produced by the two illumination directions. If the illumination directions are produced by parallel light bundles, the measuring

direction is constant in the whole measuring field. The measuring sensitivity can be calculated by the following formula:

$$u(x, y) = \frac{N \cdot \lambda}{2 \cdot \sin \theta} \quad (2.4.6)$$

where d : deformation component of the object point in the measuring direction;

N : fringe order at the measuring point;

λ : wavelength of the used laser light;

α : angle between the two illumination directions.

Out-of-plane setup

With out-of-plane ESPI, a small amount of the laser light is coupled with the object illumination and directly guided to the camera. There it is superimposed onto the image reflected from the object's surface. Object and reference light take different paths from the laser to the camera. The produced phase difference (ϕ) between both light waves produces interference effects. They are recorded by the camera as a speckle pattern. When the object is moved, the light path from the laser via the object's surface to the camera changes and produces a new phase relation ($\Delta\phi + \phi$) to the fixed reference light.

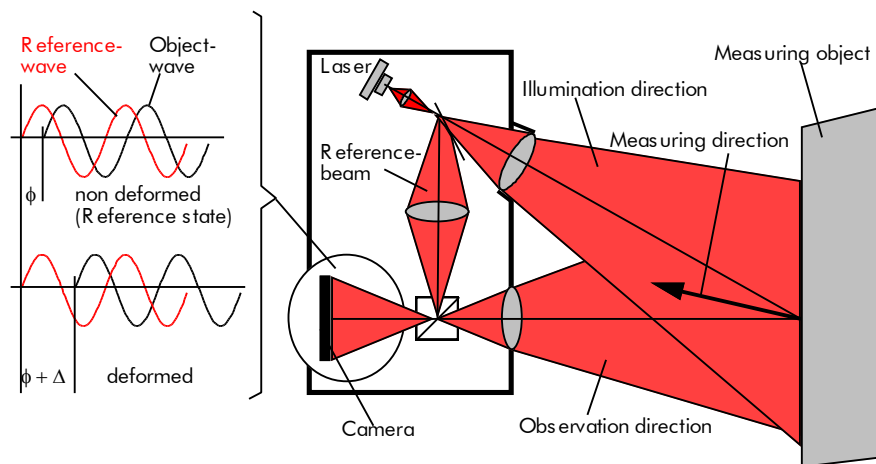


Fig.2.4.3. Measuring set-up to determine out-of-plane deformations

The measuring sensitivity can be calculated by the following formula:

$$w(x, y) = \frac{N \cdot \lambda}{2 \cdot \cos \theta} \quad (2.4.1)$$

where d : deformation component of the object point in the measuring direction;

N : fringe order at the measuring point;

λ : wavelength of the used laser light;

α : angle between illumination and observation direction.

2.4.3. Phase shifting technique. Quantitative evaluation of interferograms

In order to evaluate the correlation fringes quantitatively, typically the phase shifting technique is used. The phase shift can be applied by movement of an optical element in the illumination or observation path of the speckle interferometer[38].

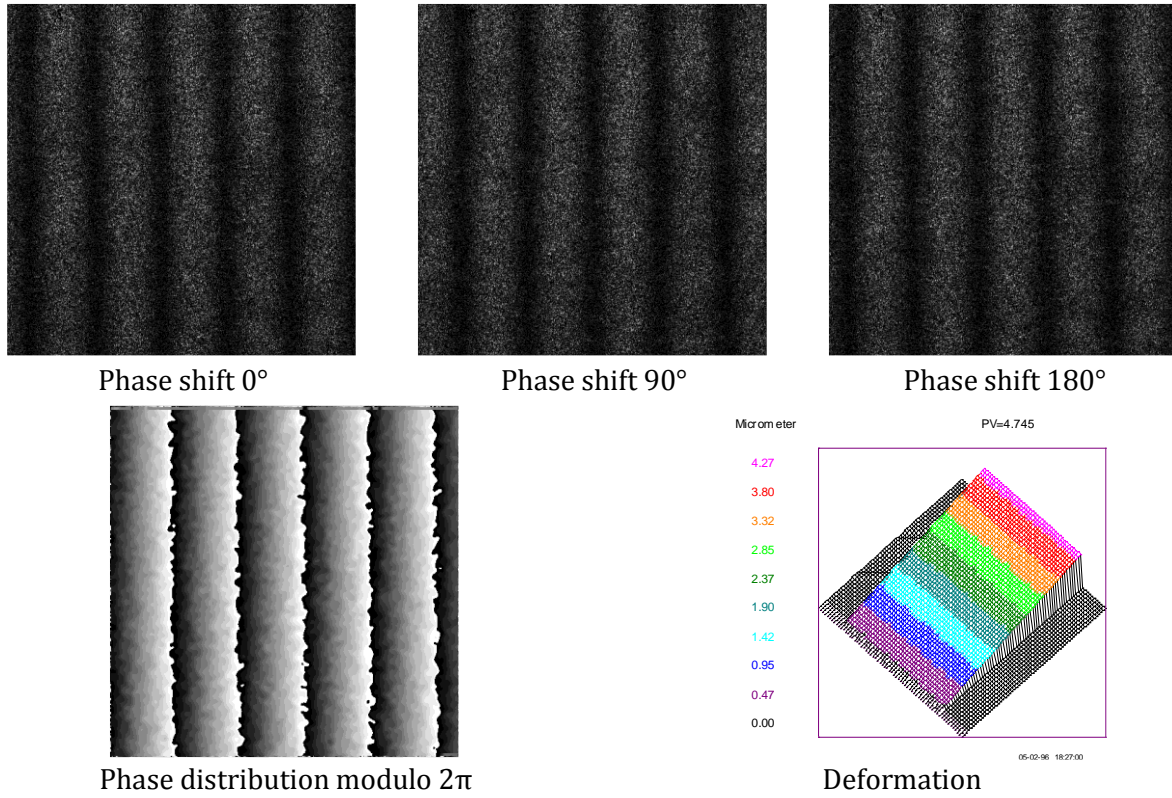


Fig.2.4.4. Phase shift technique

The phase determination relies on temporal phase shifting technique. To get the phase value from Equation (2.4.1), one has to determine the three unknowns I_0 , I_M and ϕ , so at least three acquisitions (interference images or camera frames) are necessary (Fig. 2.4.4). For a higher accuracy, a four phase algorithm was chosen in the presented studies in order to get the phase value [36]

$$\varphi(x, y) = \text{atan2}[I_4(x, y) - I_2(x, y), I_1(x, y) - I_3(x, y)], \quad \varphi(x, y) \in [-\pi, \pi], \quad (2.4.6)$$

where $I_1(x, y)$, $I_2(x, y)$, $I_3(x, y)$ and $I_4(x, y)$ are the light intensity values recorded in the four different acquisitions, corresponding to phase shifts of 0° , 90° , 180° and 270° . In practice phase modulation is conveniently achieved using a mirror mounted on a piezoelectric translator (PZT) to reflect one of the object beams. For each pixel the wrapped phase change value $\Delta\varphi(x, y)$ (modulo 2π of the true phase change $\Delta\phi$) is computed in correspondence of two different configurations, the reference state and the loaded state

$$\Delta\varphi(x, y) = \varphi_{loaded}(x, y) - \varphi_{reference}(x, y). \quad (2.4.7)$$

Finally, phase unwrapping is required to remove the 2π phase discontinuities from the computed phase map $\Delta\varphi(x, y)$ by the addition of an integral multiple of 2π to each phase value ($\Delta\varphi \rightarrow \Delta\phi$). In this way the evaluation program can also recognize the direction of the deformation as achieving higher measuring resolution beyond one fringe.

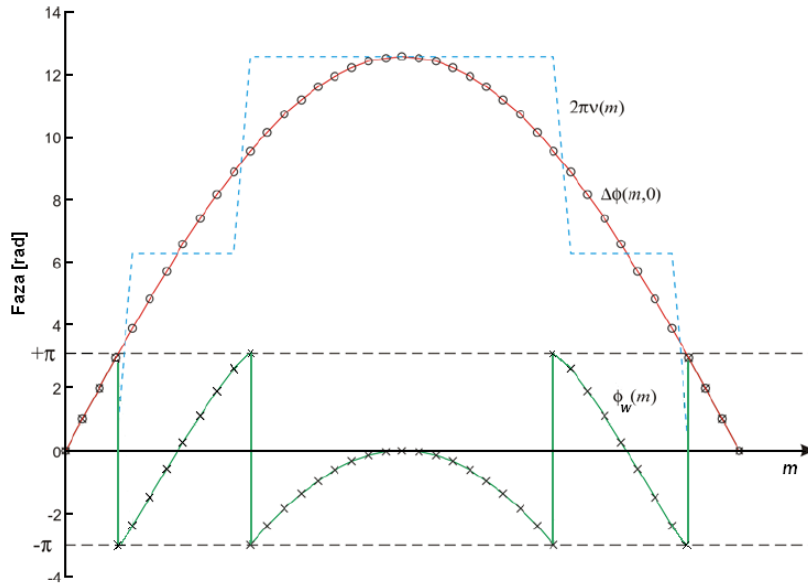


Fig. 2.4.5. Phase unwrapping

Full-field distribution of in-plane strains can be obtained by differentiating the in-plane displacement fields at each point of the measured area

$$\varepsilon_{xx} = \frac{\partial u_x}{\partial x}, \quad \varepsilon_{yy} = \frac{\partial u_y}{\partial y}, \quad \varepsilon_{xy} = \frac{1}{2} \left(\frac{\partial u_x}{\partial y} + \frac{\partial u_y}{\partial x} \right). \quad (2.4.8)$$

2.4.4. Contour measurement

Speckle interferometry techniques have proven their ability to deliver reliable and valuable information's about material behavior, deformations and strains in material testing. However, quantitative strain information had only been available on rather simple geometry's like flat surfaces or cylinders. In order to overcome this limitation, a contouring function has been developed, which allows the measurement of contour and deformation with one single instrument. The superposition of contour and deformation leads to the analysis of in-plane and out-of plane components of the deformation and hence to strains/stresses.

A 3D-ESPI sensor gives the information of the deformation of the object inside of an x, y, z coordinate system which belongs to the sensor[39]. In case of curved objects for a quantitative strain calculation the tangential components of the deformation is needed. With the knowledge of the direction of the normal vector at each point on the object, a transformation of the sensor coordinate system into the object coordinate system can be calculated. Several methods for using speckle techniques for contour measurement are known[32, 40]. One of them is the translation technique based on an in-plane setup with two illuminations of the object. The shifting of the illumination sources parallel to the x axis generates for a point P on the object a change in the optical path of Δd (Fig. 2.4.6). The value of this change depends on geometrical dimension of the sensor (\vec{L}_1, \vec{L}_2) translation (ΔL) and the relative position of the object point (P). With the use of series expansions for the absolute expressions, the z coordinate P of the object point can be separated as a function of the geometry of the set-up and the phase value measured for reason of the path change Δd .

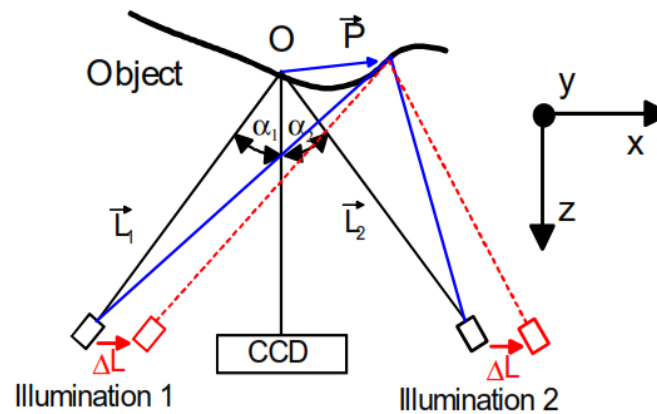


Fig. 2.4.6. Principle of contour measurement using the translation technique

This method for contour measurement is integrated into the commercial 3D ESPI measuring system called Q300 produced by Dantec-Dynamics Germany (www.dantecdynamics.com).

2.4.5. Applications of ESPI in material characterization

CHARACTERISATION OF THERMAL EXPANSION COEFFICIENT OF ISOTROPIC AND ANISOTROPIC MATERIALS

Knowledge of real material parameters is nowadays a condition for numerical simulations, widely used in industry to design quality components in very short time. The value of the thermal expansion coefficient (CTE) plays a key role in components design, in structure response or in the final decision-related materials selection. It is also desirable to be able to visualize mechanical behavior of materials or components under thermal loads. Determination of CTE with high accuracy for thin materials (e.g. thin films, foils, and shells), electronic boards, flip-chip packages or a large number of anisotropic materials (carbon fibre composites, reinforced laminates) is highly demanded. Conventional experimental procedures relying on dilatometers to measure CTE require a set of standard bars. This is not a realizable solution in above mentioned applications.

Electronic Speckle Pattern Interferometry (ESPI) is an optical measuring technique that allows rapid and highly accurate measurement of deformations. In comparison with other techniques for strain measurement or calculation, the ESPI enjoys the advantages of being non-contact, full-field, has a high spatial resolution, high sensitivity, delivers accurate displacement data and does not require any calibration or costly surface preparation. It can be applied to any material provided that the surface is sufficiently rough and the laser light is diffusely reflected. ESPI can be used for one step measurement or for a series of measurements, thus is suitable both for low or high loading[32],[41].

Carbon fibre laminated sheets have multiple industrial applications, products with low thickness being particularly required for lightweight structures. Measurement of the CTE for

anisotropic materials such as carbon fibre composites using ESPI offers not only a final value but also full-field information about the deformation of the material under thermal stress, especially if the mismatch between CTE of matrix and fibers are taken into account [42].

The CTE can be computed when the strain value and temperature change are known. Using the ESPI measuring technique, this presumes recording of the speckle patterns at two different temperatures T_1 and T_2 . T_1 corresponds to the above called reference state and T_2 for the loaded state. Using specific image processing software one can determine the full-field distributions of displacement and strain belonging to ΔT . The CTE is thus given by

$$\alpha = \frac{\varepsilon}{\Delta T}. \quad (2.4.9)$$

Anisotropic materials do not undergo a uniform thermal strain if temperature changes. For the carbon fibre composites, this effect is formed by the mismatch between thermal behavior of fibers and matrix. In this case the thermal expansion is described by a symmetrical tensor, which has the in-plane components [43]

$$\alpha_{xx} = \frac{\varepsilon_{xx}}{\Delta T}, \quad \alpha_{yy} = \frac{\varepsilon_{yy}}{\Delta T}, \quad \alpha_{xy} = \frac{\varepsilon_{xy}}{\Delta T}. \quad (2.4.10)$$

Comparable with the properties of the strain tensor the CTE corresponding to a certain direction can be expressed using coordinate transformation equations. Thus, terms as principal thermal expansion coefficients or coefficient of thermal shear can be considered. For example, if the two principal CTE's α_1 and α_2 are known, the CTE at an angle of 45° with respect to the principal directions is given by

$$\alpha_{45^\circ} = \frac{\alpha_1 + \alpha_2}{2}. \quad (2.4.11)$$

Another known aspect that should be taken into account is the temperature dependence of the CTE $\alpha = \alpha(T)$. Thus, the thermal strain can be expressed as a function of temperature

$$d\varepsilon = \alpha(T) \cdot dT. \quad (2.4.12)$$

Equation (2.4.12), taking account of $\varepsilon(T) = \int_{T_0}^T \alpha(T') dT'$, $\varepsilon(T_0) = 0$, leads to

$$\alpha(T) = \frac{d\varepsilon(T)}{dT}. \quad (2.4.13)$$

In the following the dependence between principal CTE values of an anisotropic material and the correlation fringes orientation of ESPI measurement is shown. If one consider an arbitrarily specimen orientation (Figure 2.4.7A) with the principal CTE directions rotated at an angle ξ counter clockwise from the ESPI measuring direction x , the displacements $u_x(x, y)$ of the specimen can be expressed

$$\begin{aligned} u_x(x, y) &= \Delta T [x(\alpha_1 \cos^2 \xi + \alpha_2 \sin^2 \xi) + y(\alpha_1 - \alpha_2) \sin \xi \cos \xi] \\ u_x(0,0) &= 0 \end{aligned} \quad (2.4.14)$$

According to Equation (2.4.6), the displacement value u_x is given by order N of the correlation fringes and fringe sensitivity p (defined as displacement step between two adjacent fringes)

$$u_x(x, y) = N(x, y) \cdot \frac{\lambda}{2 \sin \theta} = N(x, y) \cdot p. \quad (2.4.15)$$

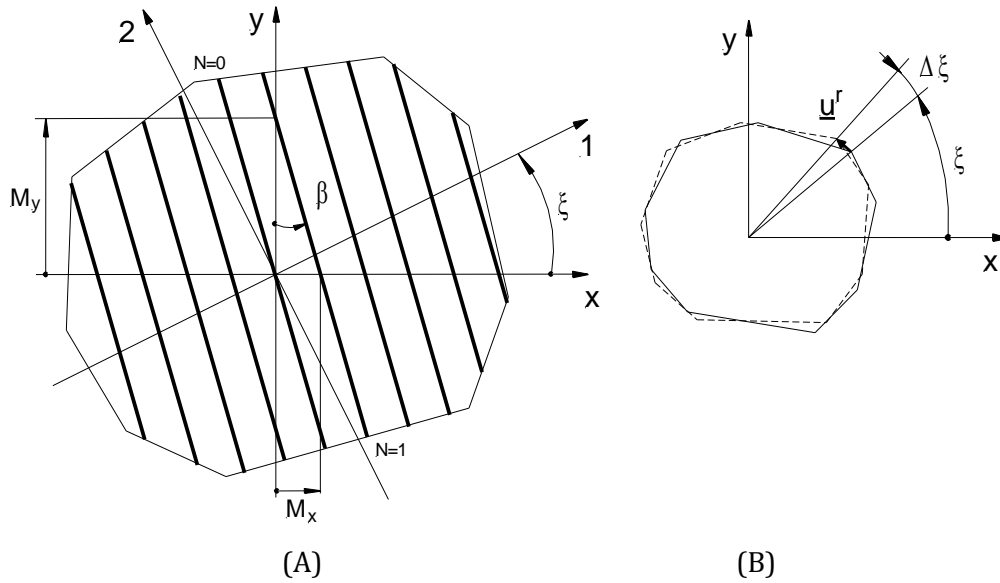


Fig. 2.4.7 (A) ESPI correlation fringes orientation in dependence with principal CTE values; (B) influence of a small rigid body rotation

Thus, the correlation fringes orientation can be determined with respect to the principal CTE's and their directions (Figure 2.4.7A). The x and y -intercepts of the $N(x, y)$ function, denoted M_x, M_y , can be determined as:

$$M_x = \frac{p}{\Delta T} \cdot \frac{1}{\alpha_1 \cos^2 \xi + \alpha_2 \sin^2 \xi}, \quad M_y = \frac{p}{\Delta T} \cdot \frac{1}{(\alpha_1 - \alpha_2) \sin \xi \cos \xi}. \quad (2.4.16)$$

Considering $\alpha_1 \neq \alpha_2$, $\alpha_2 = \kappa \cdot \alpha_1$, the inclination of the correlation fringes to the y -axis is given by an angle β in form of

$$\tan \beta = \frac{M_x}{M_y} = \frac{(1 - \kappa) \tan \xi}{1 + \kappa \tan^2 \xi}. \quad (2.4.17)$$

There are two particular cases that have to be discussed. First one, corresponding to $\kappa = 1$ and $\alpha_1 = \alpha_2 = \alpha$, represents the isotropic material model. Equation (2.4.17) yields $\beta = 0$, that means ESPI correlation fringes are equidistant and parallel with y -axis. The second one corresponds to $\kappa = 0$ and $\alpha_2 = 0$, Equation (2.4.17) yields $\tan \beta = \tan \xi$. The correlation fringes are inclined at an angle $\beta = \xi$ to the y -axis and parallel to the principal CTE direction 2. The case $\kappa \rightarrow \infty$ and $\alpha_1 = 0$ is analogous to the second one.

During the thermal expansion an arbitrarily small rigid body rotation of the specimen can occur, the displacement values in x -axis direction become then

$$u_x^r(x, y) = \Delta T [x(\alpha_1 \cos^2 \xi + \alpha_2 \sin^2 \xi) + y(\alpha_1 - \alpha_2) \sin \xi \cos \xi] - y \cdot \Delta \xi, \quad (2.4.18)$$

where $\Delta \xi$ is the rigid body rotation angle (Figure 2.4.7B).

Analogous, the tilt of the correlation fringes in measuring direction x can be derived using the new x and y -intercepts

$$M_x^r = \frac{p}{\Delta T} \cdot \frac{1}{\alpha_1 \cos^2 \xi + \alpha_2 \sin^2 \xi}, \quad M_y^r = \frac{p}{\Delta T \cdot (\alpha_1 - \alpha_2) \sin \xi \cos \xi - \Delta \xi}. \quad (2.4.19)$$

The inclination angle β^r of the correlation fringes for the general case $\alpha_1 \neq \alpha_2$, $\alpha_2 = \kappa \cdot \alpha_1$ can be written as

$$\tan \beta^r = \frac{M_x^r}{M_y^r} = \frac{(1 - \kappa) \tan \xi}{1 + \kappa \tan^2 \xi} - \frac{\Delta \xi}{\Delta T \cdot \alpha_1 (1 + (\kappa - 1) \sin^2 \xi)}. \quad (2.4.20)$$

In the case of isotropic materials, $\kappa = 1$, $\alpha_1 = \alpha_2 = \alpha$ Equation (2.4.20) leads to

$$\tan \beta^r = \frac{-\Delta \xi}{\Delta T \cdot \alpha}. \quad (2.4.21)$$

One can notice that even for very small rigid body rotation the fringe orientation changes significantly.

For the measuring direction y , the above equations can be obtained in a similar manner, the expression of displacement $u_y(x, y)$ due to the thermal stress and small rigid body rotation can be written as:

$$u_y^r(x, y) = \Delta T [x(\alpha_1 - \alpha_2) \sin \xi \cos \xi + y(\alpha_1 \sin^2 \xi + \alpha_2 \cos^2 \xi)] + x \cdot \Delta \xi. \quad (2.4.22)$$

The measurement of the CTE-tensor by ESPI and the validation of the above described theory about the thermal expansion have been performed for thin carbon fibre composites having different fibre orientations.

Two types of laminates made of SIGRAFIL PREPREG CE1007 (PREPREG means “pre-impregnated”) were investigated, both being produced as thin plates with a thickness of ≈ 0.92 mm and consisting of seven plies of ≈ 0.14 mm. The two samples differ in their structural configuration. The first one is a unidirectional laminate ($0^\circ/0^\circ$). The second one is a bi-directionally reinforced laminate ($0^\circ/90^\circ$), with the fibre orientations $0^\circ/90^\circ/0^\circ/90^\circ/0^\circ/90^\circ/0^\circ$. Specimens of 10 x 10 mm having sharp and smooth edges as well as accurate dimensions were machined by water jet cutting.

Instrumentation for the in-plane, one dimensional ESPI set-up includes typical components: a Nd:YAG laser, output power 100 mW, wavelength 532 nm and optical elements presented in Fig. 2.4.8.

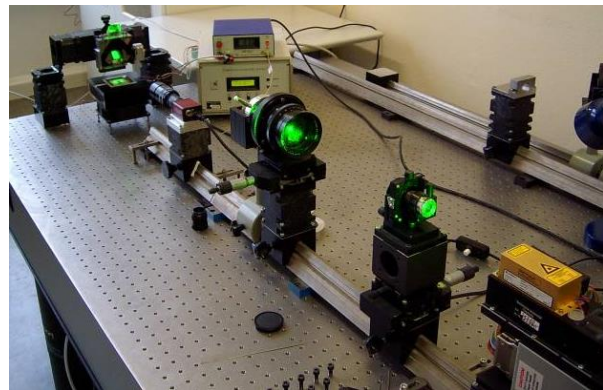
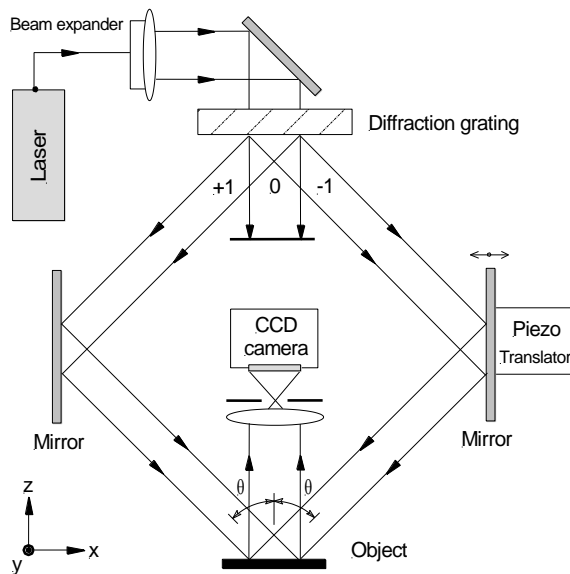


Fig. 2.4.8. Optical arrangement for in-plane ESPI

The beam splitter used was a diffraction grating with 1200 lines/mm, zero order being absorbed and the “+1” and “-1” orders representing the two illumination beams for the in-plane ESPI, measuring field was about 20 x 20 mm. The image processing system consists of a CCD

camera with FireWire technology, 8 bit, 1024 x 1024 pixels resolution and self-developed software for image acquisition and automated evaluation of interference images (Fig. 2.4.9).

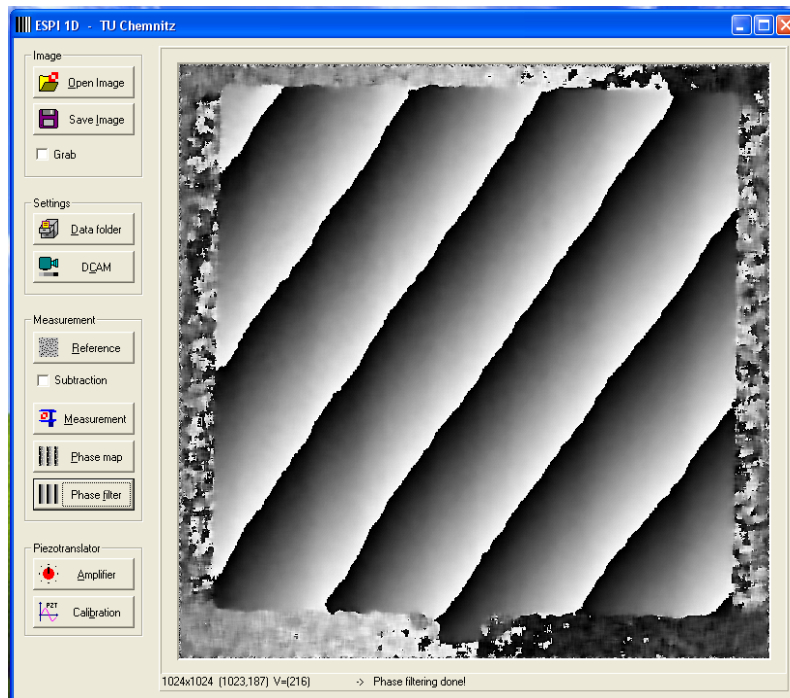


Fig.2.4.9. Self-developed software interface for 1D-ESPI setup

Figure 2.4.10 shows the experimental set-up developed to measure in-plane thermal strain of the carbon fibre specimens. It consists of two main parts: the ESPI measuring system and the heating/cooling device with temperature controller.

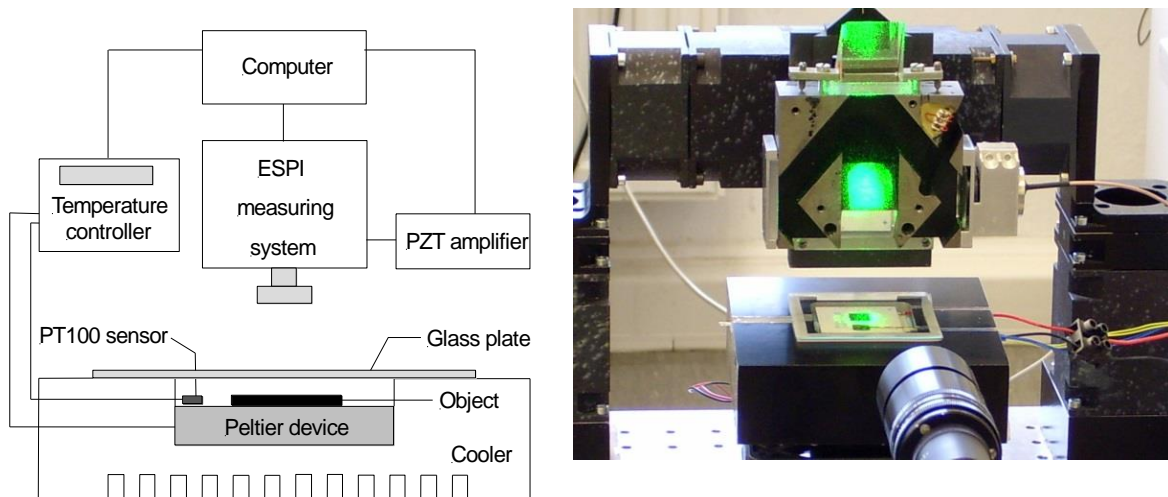


Fig.2.4.10. Experimental set-up for in-plane thermal strain measurement

Heating/cooling of the laminate plates was achieved in a small temperature chamber operating between $5 \div 70$ °C, and based on a Peltier device (known also as thermoelectric module). The Peltier device was driven by a highly accurate temperature controller. Included computer software allows temperature monitoring and implementing specialized temperature

control routines. The advantages of no moving parts, no noise, no vibration, very small size, fast temperature response, long life, capability of precision temperature control, make thermoelectric devices very suitable in applications with speckle interferometry.

Uniform heating/cooling of the specimen and precise determination of its temperature at the measurement time proved to be a critical point in connection with computation accuracy of the CTE. There are certain parameters which have to be taken into consideration, such as thermal conductivity and the heat transfer from the Peltier device to the specimen. Several tests with an infrared thermography system demonstrated that a uniform temperature field can be assumed in the thin laminate plates during heating and cooling periods. Other tests revealed only very small differences between indications of a resistance thermometer (PT 100) attached on the Peltier device surface as well as on the laminate surface.

Stationary conditions required during the ESPI phase shifting procedure can be easily achieved using the adequate control routine of the thermoelectric module. Real time observation of the correlation fringes during the thermal expansion is desirable and very helpful because certain fringes and phase perturbations can occur at temperatures higher than 50 °C. This effect is introduced by the thermal convection currents flowing around the specimen. Thermal currents can change the refractive index of the air surrounding the measuring object and hence introduce phase changes in the laser beam propagating through it[44]. The problem can be overcome by preventing fresh air coming into the temperature chamber or, much more effective, by evacuating.

The specimens of 10 x 10 mm were positioned on a horizontal plane plate without any fixation. Friction is minimized by a thin film of heat transfer paste. This procedure guarantees a free expansion and avoids any mechanical stresses within the specimen. On the other side as a disadvantage a small rigid body rotation can occur.

The specimen's surface was coated in fine white powder to increase the contrast of the ESPI fringes. A spray-on developer used for crack detection is ideal.

In-plane deformations due to thermal expansion at different temperatures were measured by ESPI in three directions for both unidirectional and bi-directional laminate plates. The first two measuring directions correspond to carbon fibre orientations (principal directions). The third one formed with the fibre directions of the outer plies an angle of 45°. Measurements were carried out during heating-up as well as cooling-down periods, in the interval 20 °C to 60 °C with temperature steps of 10 °C.

Examples of phase maps in dependence with fibre directions are presented in Figures 2.4.11 and 2.4.12 for the unidirectional laminate and in Figure 2.4.13 for the bi-directional laminate, respectively.

The unidirectional laminate has a CTE value in fibre direction of nearly zero, $\alpha_1 \neq 0, \alpha_2 \approx 0$. If no rigid body rotation occurs, the fringe orientation corresponds to the described mathematical model (Equation (2.4.17), $\kappa = 0$), as it can be observed in Figure 2.4.11. Thus, the fringes are parallel to the y -axis (Figure 2.4.11A) if the measuring direction is a principal direction $\xi = \beta = 0$ and they are inclined at an angle of 45° from the y -axis if the principal material directions are rotated at $\xi = 45^\circ$ from the measuring direction (Figure 2.4.11C).

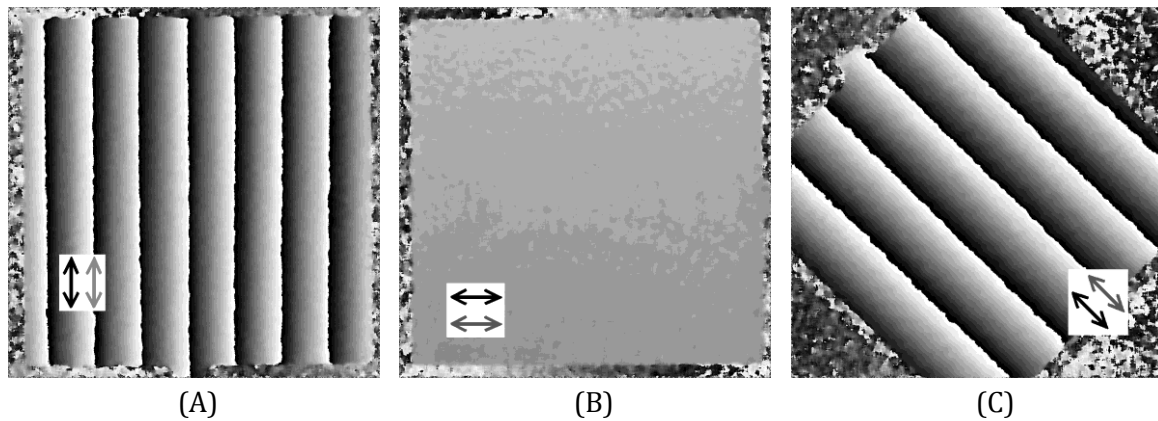


Fig.2.4.11. Phase maps of unidirectional laminate for fibers direction: (A) perpendicular to measuring direction, (B) parallel with measuring direction, (C) rotated -45° from measuring direction.

In many cases, when no movement restrictions are applied to the specimen, a small rigid body rotation occurs and the “ideal” fringe directions cannot be observed experimentally. The effect of rigid body rotation was stated mathematically in Equation (2.4.20) and is clearly visible in Figure 2.4.12 for the unidirectional laminate. For this specimen, a fringe tilt of ≈ 9 degrees means a rotation of $\approx 3 \cdot 10^{-3}$ degrees, visible in the Figure 2.4.12A.

It is very important to notice that fringe tilt does not influence thermal strain value in measuring direction. The distance M'_x between fringes is not affected by a small rigid body rotation (see the left one of Equations (2.4.19)). Therefore free positioning of specimens without fixation as above described has turned out to be a very useful method.

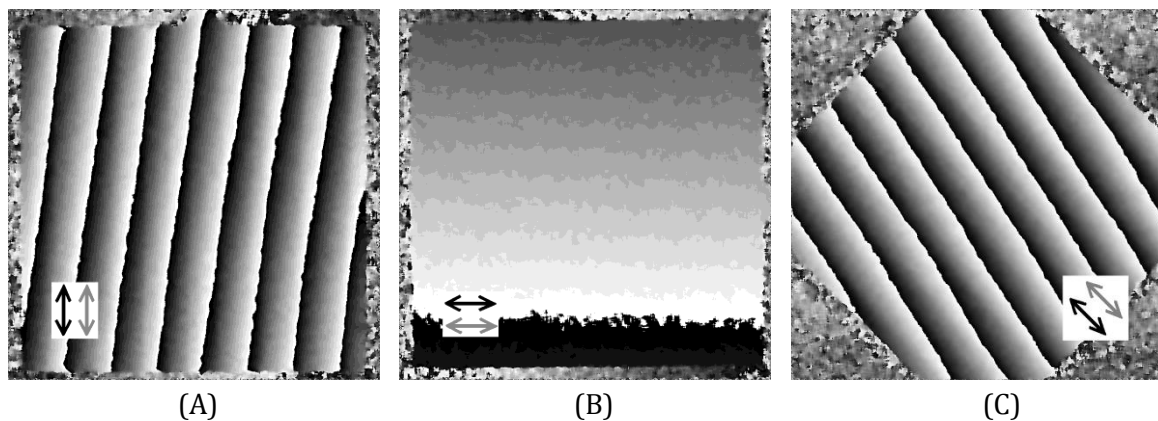


Fig.2.4.12. Phase maps of unidirectional laminate undergoing a small rigid body rotation and having fibers direction: (A) perpendicular to measuring direction, (B) parallel with measuring direction, (C) rotated -45° from measuring direction.

On the other side the distance M'_y between fringes significantly depends on the unknown angle of a small rigid body rotation (Equations (2.4.19)). That means, direct measurement of thermal shear strain ε_{xy} and accurate calculation of the coefficient of thermal shear is therefore a problem. It should not be discussed here.

For the bi-directional laminate the problem is similar. Figure 2.4.13 shows phase maps corresponding to different orientations of the outer 0° -plies with respect to the measuring

direction. For example, the measured fringe inclination with respect to y -axis was about 19° when the specimen is rotated at an angle $\xi = 45^\circ$, validating the theoretical prediction. The fringe inclination is the result of the thermal anisotropy as well as of a small rigid body rotation.

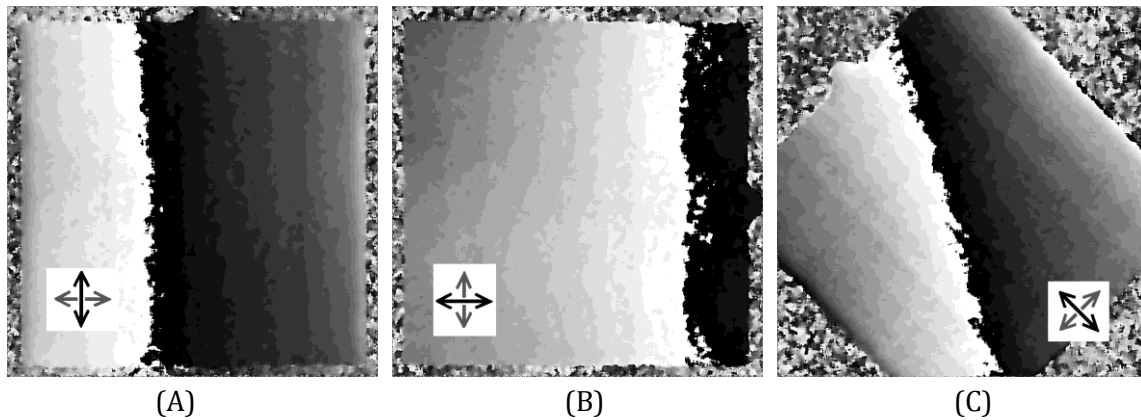


Fig.2.4.13. Phase maps for bi-directional laminate for upper fibers direction: (A) perpendicular to measuring direction, (B) parallel with measuring direction, (C) rotated -45° from measuring direction.

Quantitative values of the CTE for the two investigated carbon fibre laminates are shown in Tables 2.4.1 and 2.4.2 as well as Figure 2.4.14. CTE's are experimentally determined at different temperatures for the two principal material directions (0° and 90°) and at 45° with respect to these axes. A weak temperature dependence of the CTE's can be observed.

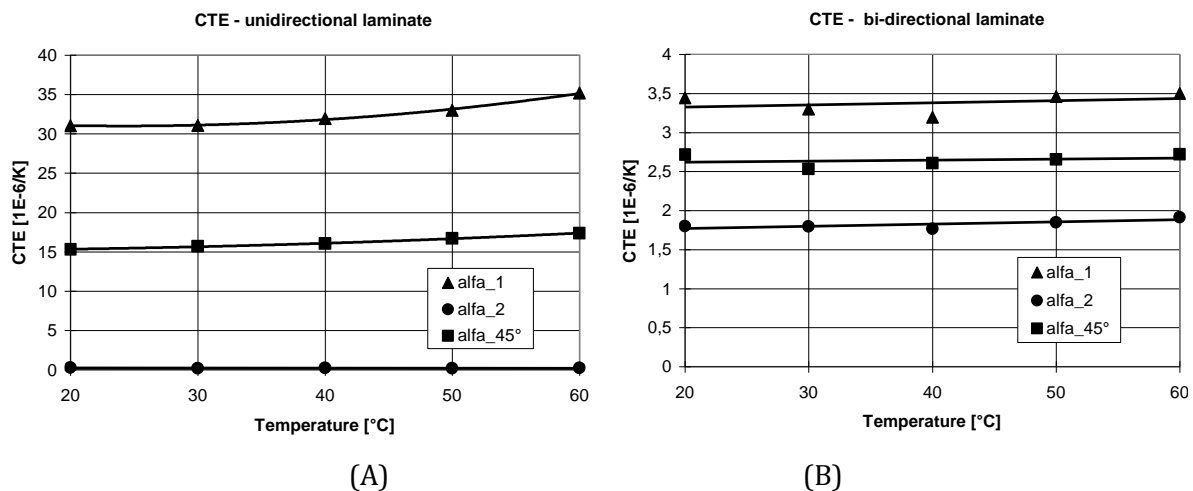


Fig.2.4.14. Expansion coefficient in dependence with material principal directions: (A) unidirectional, (B) bi-directional laminate

Besides, Tables 2.4.1 and 2.4.2 show the comparison between measured and calculated values of the CTE in the 45° -direction. If the values in the two principal material directions are known, the calculated values for 45° can be obtained from coordinate transformation equation of the CTE tensor, Equation (2.4.11). It is seen, that the deviations between experimental results and theoretical expectations are always smaller than 5%.

Table 2.4.1. Values of the CTE for unidirectional laminate

Unidirectional Laminate	Measurement temperature [°C]	Coefficient of thermal expansion α [$10^{-6}/K$]				Relative deviation [%]
		α_1	α_2	α_{45°	$\alpha_{45^\circ} = \frac{(\alpha_1 + \alpha_2)}{2}$	
	20	31,04	0,25	15,31	15,65	2,20
	30	31,07	0,18	15,67	15,62	0,26
	40	31,93	0,24	16,03	16,08	0,31
	50	33,00	0,17	16,68	16,59	0,55
	60	35,17	0,21	17,37	17,69	1,86
<i>Average value</i>		32,44	0,21	16,21	16,33	0,71

Table 2.4.2. Values of the CTE for bi-directional laminate

Bi-directional Laminate	Measurement temperature [°C]	Coefficient of thermal expansion α [$10^{-6}/K$]				Relative deviation [%]
		α_1	α_2	α_{45°	$\alpha_{45^\circ} = \frac{(\alpha_1 + \alpha_2)}{2}$	
	20	3,44	1,80	2,72	2,62	3,54
	30	3,30	1,80	2,53	2,55	0,72
	40	3,19	1,77	2,61	2,48	4,80
	50	3,46	1,85	2,654	2,652	0,07
	60	3,50	1,92	2,72	2,71	0,46
<i>Average value</i>		3,38	1,82	2,64	2,60	1,64

The high sensitivity and full-field information of the ESPI measurement is especially valuable in case of non-homogenous materials. Thus, the mismatch between thermal behavior of matrix and fibers in cases of the investigated laminates became visible. An example of thermal strain distribution is presented in Figure 2.4.15.

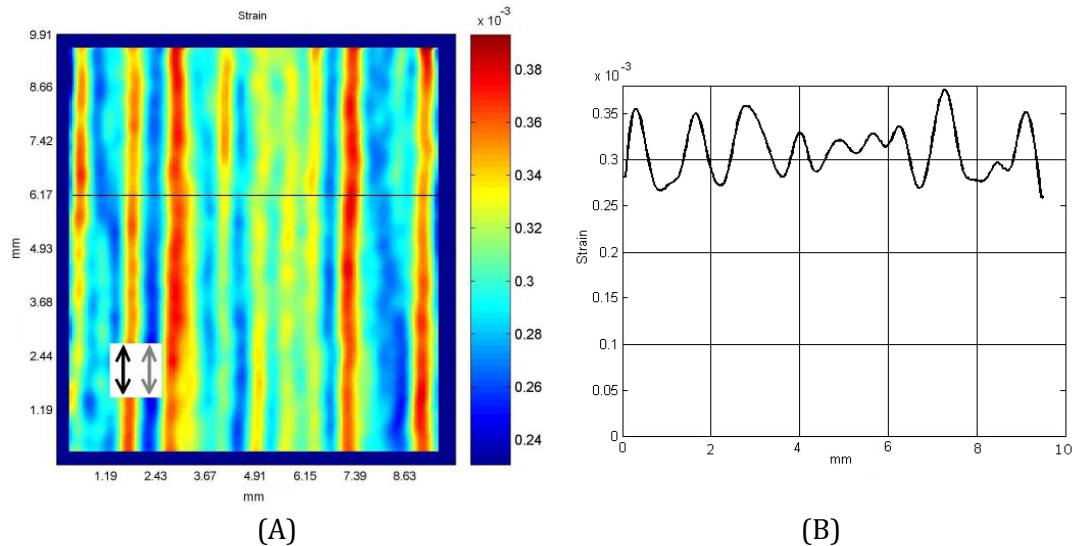


Fig. 2.4.15. (A) Local variation of thermal strain [$\mu\text{m}/\text{mm}$] for unidirectional laminate; (B) strain profile along the selected path

In this example it has been shown that the full-field and real time technique of the Electronic Speckle Pattern Interferometry (ESPI) is eminently suited to analyses the thermal expansion behavior and to determine the coefficients of thermal expansion (CTE) for thermally isotropic as well as anisotropic solid materials. It could be proved that the optical method of

ESPI has special advantages for the investigation of thin (< 1 mm) and small (< 10 mm) specimens, for which other methods cannot be applied. Another advantage is that the fringe or phase maps give important information about the uniformity or non-uniformity of the strain field in the specimen as for example in composites.

Especially for the non-trivial case of anisotropic materials the connection between fringe tilt and a small but unknown rigid body rotation and the influence upon the calculated CTE-values can be theoretically described. Only thereby is it possible to interpret all the experimental results and phenomena. It could be shown that a small rigid body rotation does not influence the accuracy of the CTE.

The overall accuracy of the CTE measurement by the suggested method was estimated at $\approx 0.1 \times 10^{-6}$ [1/K]. A first condition for such a high accuracy is the precise measurement of the thermal strain by ESPI including phase shifting technique. The second condition is the precise temperature measurement and control. The realized temperature chamber based on a Peltier device and a control unit in combination with a computer controlled temperature monitoring satisfies the high requirements of temperature measurement and adjustment.

The described investigations of anisotropic unidirectional and bi-directional carbon fibre laminates are only examples for the proposed technique, which can be applied to many other solid bodies. Some further developments are needed for anisotropic materials with unknown principal directions. If experimental CTE-values in more directions than absolutely necessary are measured the identification of the CTE-tensor elements can be carried out by a regression algorithm.

INVESTIGATION OF NON-LINEAR SPRINGBACK FOR HIGH STRENGTH STEEL SHEETS

The springback prediction in deep drawing is an important issue for the production of car bodies in the automotive industry. Springback, the elastically-driven change of the shape of a part during unloading after forming, has become a growing concern in the assembling process as currently the manufacturers increasingly use steels with higher strength. Because of their higher strength to Young's modulus ratio, these materials show an increased springback than traditional low-strength steels. It is absolutely necessary to compensate the springback in the design of deep drawing tools in order to obtain specified final shapes. Therefore, a good knowledge of the material mechanics of unloading after large elastic-plastic deformations is the base for an accurate description of springback[45].

A fundamental assumption of most plasticity models is that the unloading process, after elastic-plastic deformation, is elastic and linear with the same Young's modulus as in loading (Figure 2.4.16A). Sometimes, it is pointed out that the unloading process and a following reloading could show non-linear and inelastic effects (Figure 2.4.16B). On the one hand, the theoretical tool of Bauschinger effect and kinematic hardening can describe reasonably well the deformation behavior of reverse loading but, on the other hand, it doesn't describe the material behavior shown Figure 2.4.16B.

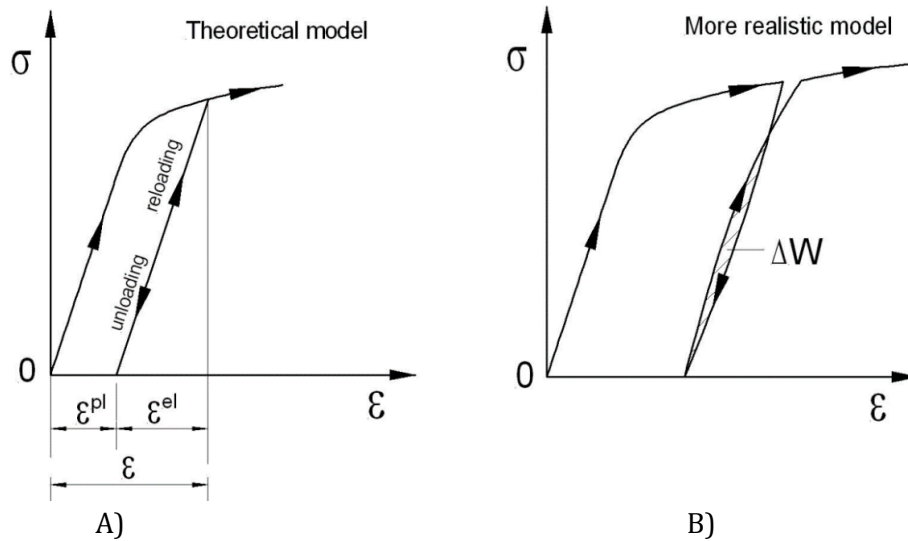


Fig. 2.4.16. Elastic-plastic material behavior:
A) theoretical model, B) a more realistic model

Wong and Johnson (1988) [46] have applied elastic theory including higher order elastic constants to explain a small departure from linearity by loading and unloading. Other researches have shown that micro plastic mechanisms affect the unloading behavior. Hart's [47] micromechanical model for inelastic deformation assumes that resistance to dislocation motion produces an inelastic strain (internal stress) due to pile-up of dislocation. Ghosh (1980) [48] states that mobile dislocation density is increasing during loading due to activations of dislocation and is decreasing during unloading due to annihilation and runback. Yamaguchi et al. (1998) [49] reported some experimental observations and that Young's modulus of sheets metals after biaxial stretching drastically decreases with prestraining. Yoshida et al. (2001) [50] investigating elastic-plastic behavior of steel sheets for deep drawing, observed during loading reversal a decrease in Young's modulus with increasing prestrain and derived the value of the "average elastic modulus" (defined as an average slope of the unloading stress-strain curve in a certain stress range) as a function of the accumulated plastic strain.

Recent investigations of Cleveland (2002) [51] have found that the average tangent modulus during unloading and reloading differs from their elastic values in the undeformed state and that this modulus referred as the "springback modulus" decreases linearly with plastic prestrain. According to [51] changes in the Young's modulus are shown to appear due to the recovery of micro plastic strain. Commercial alloys of aluminum and high strength steel were studied by uniaxial stretching, in-plane strains were measured by strain gauges. Strain introduced during loading was limited to less than 3% so as to not destroy the strain gauges. Sequential loadings were applied to obtain a higher strain level. Each loading and unloading test having different level of prestrain was run at constant cross-head speed. A model based on physical mechanisms for compliance recovery was proposed to describe the tension-unloading and compression segments.

Experimental measurement of the non-linear strain-stress response during the unloading of metal sheets undergoing large plastic deformations requires a very accurate method. Classical extensometers working in contact with the specimen would be suitable for this task. The strain gauge technique offers the required accuracy but the strain gages should be glued after the prestrain for best results. On the other hand, full-field optical methods are attractive

tools to get the strain values during unloading with high confidence. The electronic speckle pattern interferometry (ESPI) is an optical measuring technique that allows rapid and highly accurate measurement of displacements and deformations. It enjoys the advantages of being non-contact, full-field, it has a high spatial resolution and sensitivity. The ESPI principle is well described in the literature[38].

Instrumentation for the in-plane, one-dimensional ESPI set-up includes as typical components an Nd:YAG laser (100 mW, $\lambda=532$ nm) and optical elements presented in Fig. 2.4.8. The beam splitter used was a diffraction grating (1200 lines/mm). The “+1” and “-1” diffraction orders form two plane coherent waves at an angle of $\theta = 25.40^\circ$ for the illumination of the measuring field with a size of approximately 20 x 20 mm.

The displacement u_x can be calculated when the phase change $\Delta\phi(x, y)$ is known according to the following formula presented in more detail in [38]

$$u_x(x, y) = \Delta\phi(x, y) \cdot \frac{\lambda}{4\pi \sin \theta}. \quad (2.4.23)$$

This means the displacement difference between two speckle correlation fringes is $\Delta u_x (\Delta\phi = 2\pi) = 0.417 \mu m$.

To increase the performance of the ESPI, a temporal phase shifting technique is used. The phase shifting algorithm gives the phase change at each pixel of the image as shown in Figure 2.4.17. The image processing system consists of a CCD camera (AVT Dolphin F145B, IEEE 1394 interface, 1392x1040 pixels resolution, 15 fps frame rates at full resolution, 16 internal frame buffers) and in-house developed software for image acquisition and evaluation of interference images. The measurement of relatively large displacements by ESPI requires a serial measurement in combination with the temporal phase shifting algorithm.

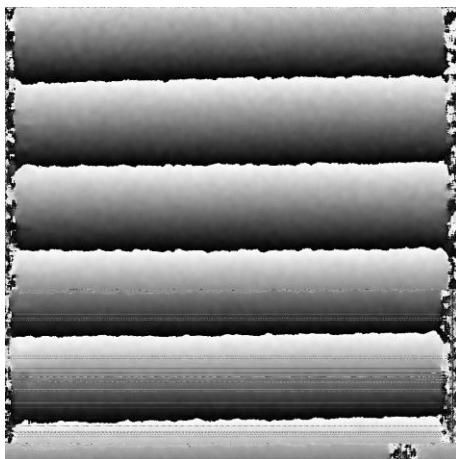


Fig.2.4.16. Phase map of one measuring step

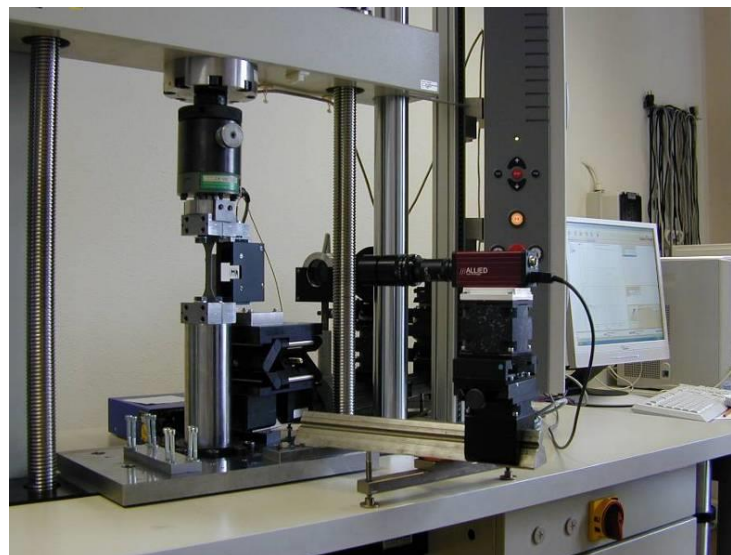


Fig. 2.4.17. Measurement setup to determine non-linear recovery of metal sheets by ESPI

Through its original design the interferometer enjoys the advantage of collimated laser beam (constant sensitivity vector), well defined geometry (incidence angles of the object beams given by the diffraction grating), stable four frame phase shifting algorithm with image based calibration of the phase shifter, fast image acquisition and rigid design.

The speckle interferometer components were mounted on the 100 kN capacity Zwick/Roell testing machine (Figure 2.4.17). The load–crosshead displacement data were collected from the testing machine and the full-field specimen displacements and strains were measured by ESPI.

Temporal phase shifting procedure assumes that the state of the measured object doesn't change during the acquisition of the phase shifted speckle interferograms. This is not fulfilled when ongoing processes are investigated, the calculated phase value being susceptible to errors. The errors are similar to those produced by mis-calibration of the phase shifter. After several tests and studies the crosshead speed during the unloading process was set at 10 $\mu\text{m}/\text{min}$ for all measurements. For the above described measuring system the phase shifting procedure (including piezo translations, image acquisition, transmission and storage of the four interferograms) is executed within 1s, the analysed area of the specimen (12x12 mm) is shifted during this time with ~ 70 nm. The most part of the introduced phase error is a constant offset which cancels when measuring phase changes.

The best way to have an overall evaluation of the ESPI measurement accuracy was to compare it with other technique. Figure 2.4.18 shows a comparison during unloading between ESPI and strain gauge technique for the same specimen. The small differences ($\sim 2\%$) proved the reliability and accuracy of the developed ESPI measuring system. Full-field information, in terms of strains in tensile direction, pointed out a homogenous distribution. The final strain values were calculated as mean values of all points in the evaluated area. Sensitivity of the measured strain is about $5 \cdot 10^{-6}$.

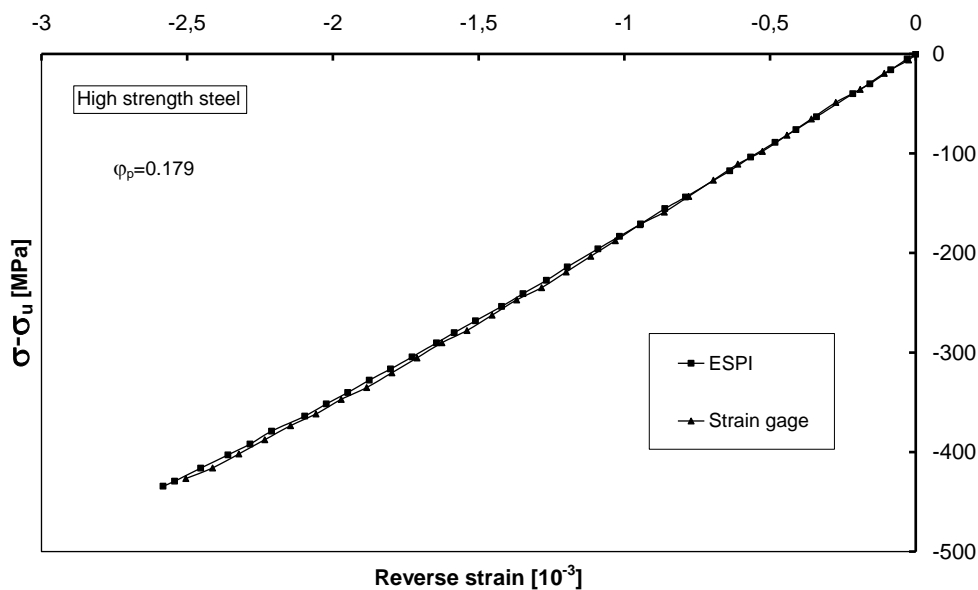


Fig. 2.4.18. Comparative analysis: ESPI vs strain gauge technique

Two types of steel sheets, cold-rolled high strength micro-alloyed steel sheet (H320LA / EN10268) and low carbon steel sheet (DC04 / EN10130) were tested in the as-received state. Both sheets had a thickness of 1 mm.

Because of the higher stress level, the knowledge of the springback is particularly important for the new high strength steels. Therefore the main focus of the investigations is oriented to the steel type H320LA. The traditional deep drawing steel sheet DC04 is investigated for comparison.

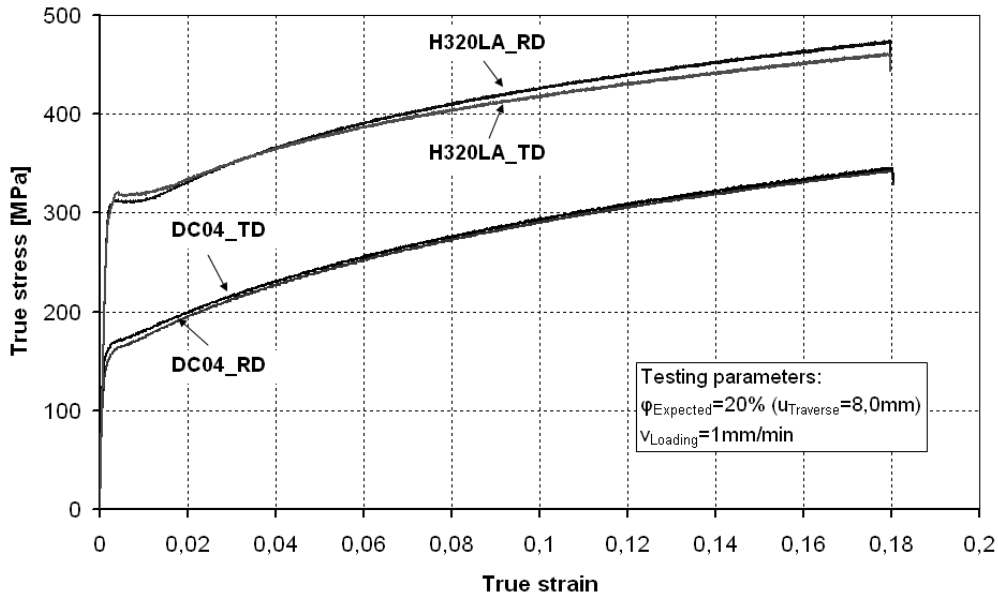


Fig. 2.4.19. Stress-strain curves for RD- and TD-specimens

The orthotropy axes of the deep drawing sheets are described as rolling (RD), transverse (TD) and normal (ND) directions. RD- and TD-specimens were cut by the water jet technology to avoid deformations and temperature influence. All the specimens had in the center a width of 12mm and an FEM-checked homogeneous uniaxial stress state in a region of a 20mm approximate length. To avoid large rigid body displacements in view of the ESPI technique a high-precision gripping device was constructed as shown in Figure 2.4.17. The specimens were clamped between two rigid blocks by four screws on each end without any slip-effects.

The stress-strain response is shown in Figure 2.4.19. For both steel types the difference between rolling and transverse directions is remarkably small. Lueders lines or similar effects at the yield stress are not observed.

Both steel types were investigated metallographically in the as-received state to observe the texture and the effect of the cold rolling on the microstructure. Figure 2.4.20 shows that the structure in the RD-ND-plane of the two alloys is slightly anisotropic. This can also be observed in the TD-ND-plane but, in this case, the anisotropy is smaller.

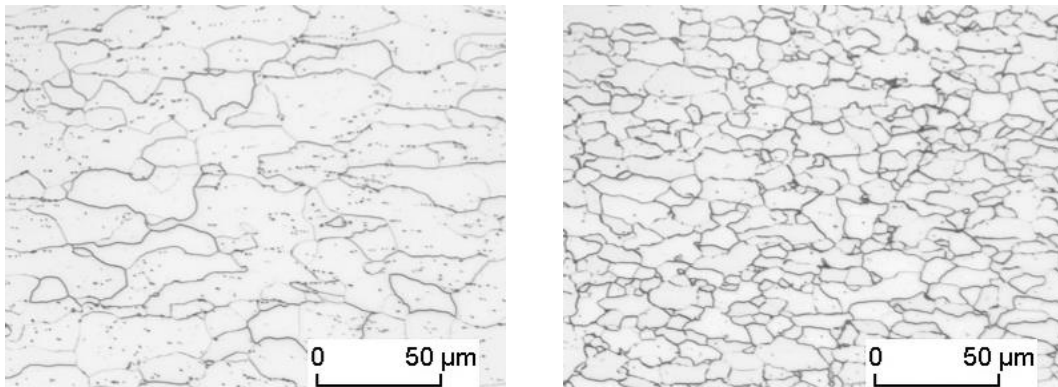


Fig.2.4.20. Metallographic structure in the RD-ND-plane for DC04 and H320LA steel

Also, surface roughness determinations for unloaded and plastically loaded specimens in rolling and traverse directions were performed. A summary, of the achieved results in our own experiments to characterize the materials, is presented in Table 2.4.3.

Table 2.4.3. Measured properties of the investigated materials

<i>Material properties</i>	DC04	H320LA	<i>Unit</i>
Sheet thickness	1.0	1.0 (10 μm Zn)	mm
Young's modulus (measured with strain gauges)	200000	212000	N/mm^2
Yield stress	160	312	N/mm^2
True stress at a logarithmic strain $\varphi = 0.10$	292	423	N/mm^2
$\varphi = 0.18$	343	466	
Mean linear grain size (as-received state)			μm
RD-ND-plane:			
RD	24	11	
ND	12	7	
TD-ND-plane:			
TD	20	9	
ND	12	7	
Average roughness R_a (RD-TD-plane)			μm
as-received state:			
RD	1.3	1.0	
TD	1.2	0.9	
deformed state, $\varphi = 0.18$:			
RD	1.3	0.9	
TD	1.4	1.0	

The loading-unloading cycle consisted of the following three steps:

- continuous loading up to different levels of prestrain
- loading interruption (crosshead stop)
- continuous unloading.

Figure 2.4.21 shows the typical stress-strain curve of the high strength steel sheet H320LA corresponding to a prestrain value of approximately $\varphi = 0.095$. The dots represent discrete full-field ESPI measurement steps and only a small part is visible near the end of the loading curve. After loading the specimen up to a desired prestrain level the crosshead was stopped for a period of time and then unloading began. If the loading of the specimen is interrupted, a drop in stress was observed experimentally. In Figure 2.4.21 is seen that this is not a pure relaxation process. Because the testing machine is not ideally rigid, the strain of the specimen increases as well.

During the third step, the unloading strain-stress response of the specimen can be observed with high precision by the serial ESPI technique. The level of the very large prestrain in relation to the strain during unloading does not influence the accuracy of these ESPI measurements. If the unloading response is observed carefully, the stress-strain curve shows two remarkable effects. First, in contrast to the basic assumptions in plasticity theory, the mechanical behavior during unloading is clearly non-linear. Secondly, it can also be noticed that the springback is considerably larger than expected according to the primary Young's modulus.

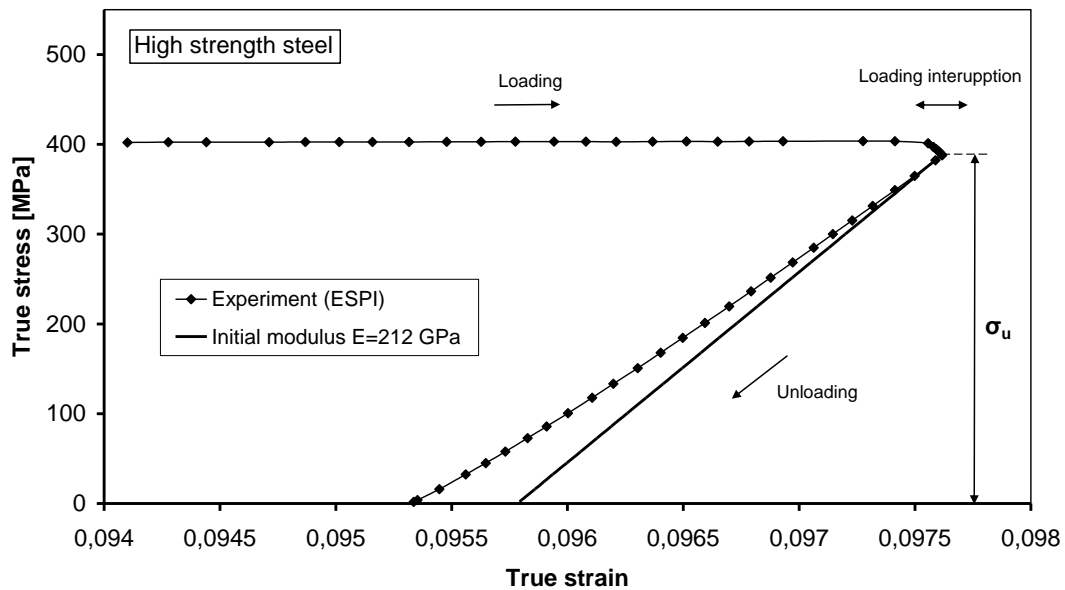


Fig.2.4.21. Unloading strain-stress response for the high strength steel sheet

Starting from these experimental observations it was attempted to identify the effect of different material and testing parameters on strain-stress response of the steel sheets by unloading. Investigated parameters were: type of steel sheets, rolling and transverse direction, strain rate, load interruption time periods before unloading, prestrain level and partly unloading followed by re-loading cycles.

The high strength steel as well as the low carbon steel showed the described non-linear effects. For the samples prestrained in tension to $\varphi = 0.18$, the measured strain recovery exceeds the expected linear recovery by about 25% for the high strength steel and 21% for the low carbon steel (Figure 2.4.22).

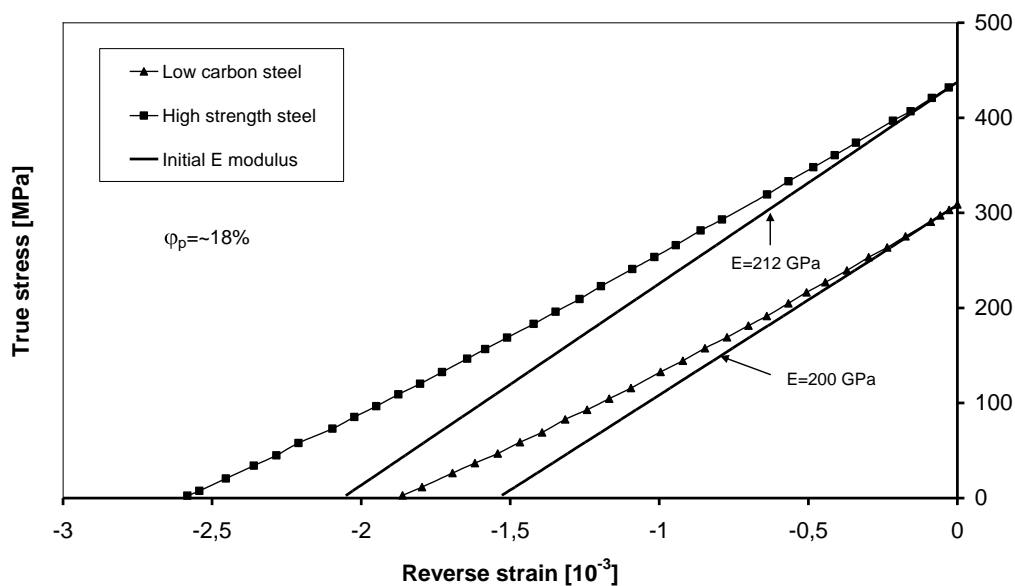


Fig.2.4.22. Inelastic recovery for the high strength steel in comparison with the low carbon steel

Analyzing the measurements results during unloading for steel sheets in rolling and traverse direction, differences couldn't be noticed. The measured strain-stress curves overlapped for the same prestrain value and testing parameters. An explanation can be found in the almost identical flow curves (Figure 2.4.19) and the relatively small crystallographic texture of the steel sheet in rolling and traverse direction (Figure 2.4.20).

To study the influence of the strain rate the specimens were loaded to a prestrain of $\varphi = 0.18$ with four crosshead speeds of 0.02, 1, 10 and 100 mm/min. This is equivalent with an initial strain rate of 0.07×10^{-5} , 3.5×10^{-5} , 35×10^{-5} and $350 \times 10^{-5} \text{ s}^{-1}$. The obtained results point out that there is no marked influence of the loading strain rate upon unloading strain-stress response of the steel sheets. In a logical succession, for a selected prestrain and crosshead speed, the influence of different unloading strain rates upon inelastic recovery had to be investigated. Because the ESPI method based on temporal phase shifting is limited in measuring high speed processes, the results obtained by speckle interferometry for a crosshead speed of 10 $\mu\text{m}/\text{min}$ were compared with those obtained by strain gauge measuring technique at 1 mm/min. Similar to the case of loading, a marked rate dependence of the inelastic recovery could not be detected. It is worth noting that strain gauges were glued on the tension specimens under load after the prestrain, during the crosshead stop, with a quickly curing strain gauge adhesive.

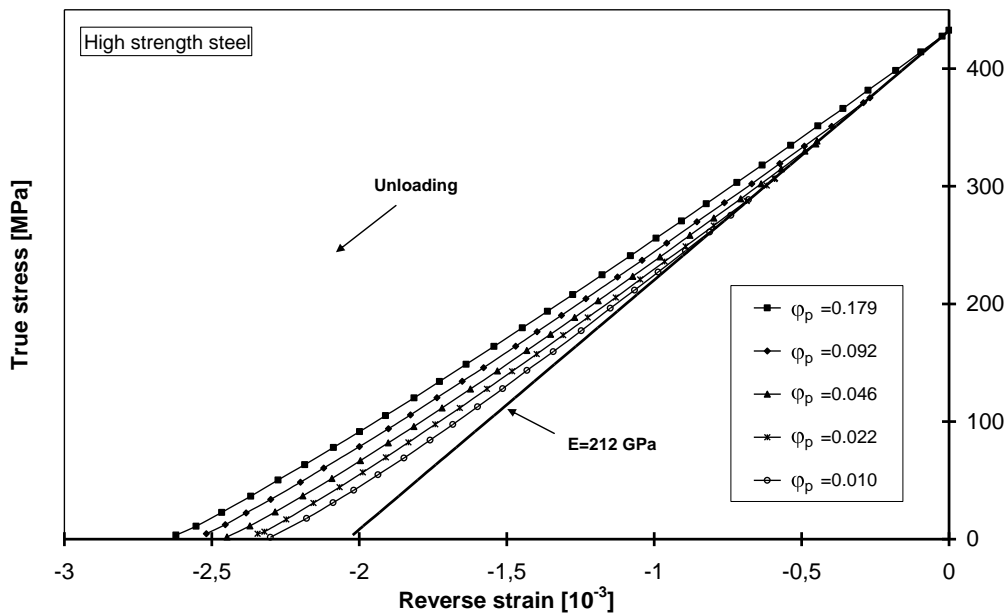


Fig.2.4.23. Inelastic recovery of the high strength steel sheets after several prestrain levels

In the tensile test after loading the specimen at desired prestrain level the crosshead was paused for a period of time and then unloading began. Experimentally, it was observed that a drop in stress occurs if the loading of the specimen is interrupted. The stress starts to relax to a threshold value and rise again to the value attained before when the loading is resumed. An appropriate description of this phenomenon can be made using the viscoplastic model with a threshold value for creep. The curve drawn through the stress values after relaxation is very close to a curve obtained in an extremely prolonged tensile test. The threshold stress value can be approximated to the stress diminished by this drop in stress and stands for the unloading stress σ_u in our investigations. Relaxation to the threshold values occurs in time periods of

minutes. It was also analyzed if this time period influences the inelastic response of the metal sheets by unloading. Furthermore, we tried to find out the effect of loading interruption time period in combination with the loading strain rate and prestrain values upon inelastic recovery. Comparison of the stress-strain response by unloading for two waiting periods (10 s and 15 min) revealed no differences of the final value of inelastic recovery and minor differences just after the beginning of unloading which would occur due to the viscosity of the steel and the above described relaxation phenomenon. A part of a prolonged tensile test is shown in Figure 8, the strain values resulting from a full-field ESPI measurement.

Inelastic response of the high strength steel sheets during unloading for five levels of prestrain is depicted in Figure 2.4.23. It was found that inelastic strain recovery increased when the value of prestrain became larger.

Instantaneous tangent modulus, defined as the slope of a line tangent to the stress-strain curve at a point of interest, may be calculated from the stress-strain data as $E_t = d\sigma/d\varepsilon$. Its value as function of prestrain and normalized stress σ/σ_u is plotted in Figure 2.4.24. Different stages characterize the instantaneous tangent modulus curve, noticed also by Cleveland et al.[51]. At the beginning of unloading ($0.9 < \sigma/\sigma_u < 1$) the instantaneous tangent modulus decrease rapidly, then it follows a relatively gradual decrease ($0.2 < \sigma/\sigma_u < 0.9$). When the stress value approaches zero ($\sigma/\sigma_u < 0.2$) it drops significantly. This Young's modulus is reduce in comparison with its initial elastic value and further decreases with the diminishing stress. The first stage is strongly influenced by the load interruption time. Immediately unloading after loading produces a drop of the instantaneous tangent modulus, which is attenuate after the stress reaches the threshold value.

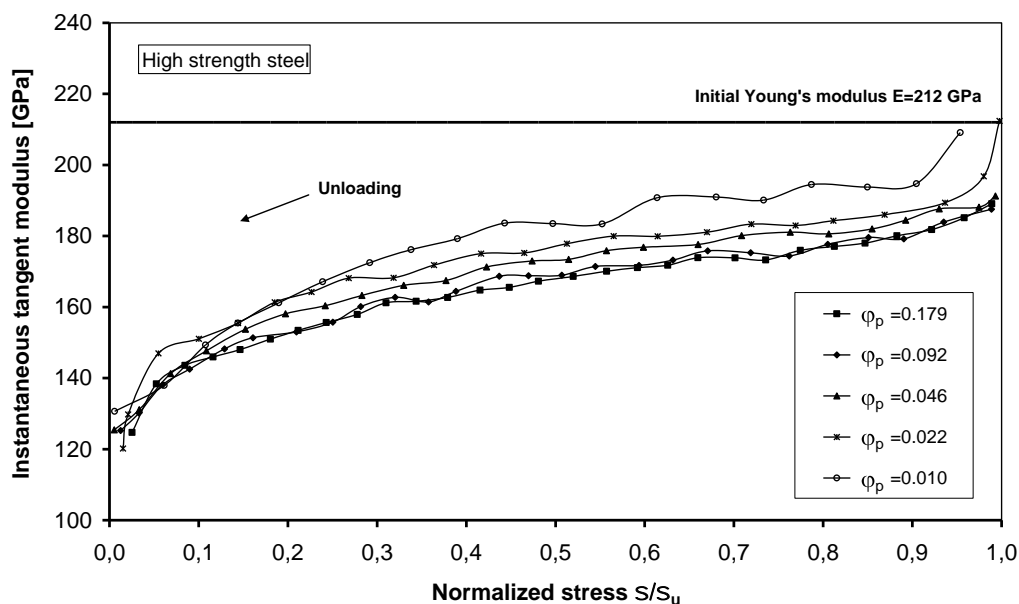


Fig.2.4.24. Instantaneous tangent modulus of unloading for high strength steel sheet

Another unloading modulus called secant modulus is obtained by calculating the slope of the line joining the coordinates of the start and end of unloading. From the unloading stress-strain curve at each value of stress decrement, the instantaneous secant modulus defined as the

stress to strain ratio $E_s = (\sigma_u - \sigma)/(\varepsilon_u - \varepsilon)$, may be calculated. Values of instantaneous secant modulus as function of prestrain and normalized stress σ/σ_u are plotted in Figure 2.4.25.

The instantaneous secant modulus also decreases with increases of prestrain. The curves corresponding to a higher prestrain value are situated under those corresponding to a lower prestrain value. The above described stages in the tangent modulus evolution during unloading can be also associated with the secant modulus curves. A smoother transition between them occurs especially in the stress range $\sigma/\sigma_u < 0.2$.

Concluding, the unloading Young's moduli decrease with the increase of prestrain level and the influence of the prestrain path upon inelastic strain recovery is minor. When the prestrain values become large enough they approach their asymptotic values (saturated values).

An interesting result (Figure 2.4.26) was obtained conducting a cyclic straining and subsequent partly unloading. The specimens first undergo a prestraining in tension to about 18%, followed by unloading to $\sigma = \kappa \cdot \sigma_u$ ($\kappa = 0, 0.25, 0.5$ and 0.75) and then reloading close to σ_u . It must be noted that the Young's modulus of reloading is the secant modulus of unloading corresponding to the initial part of the strain-stress curve ($0.75 < \sigma/\sigma_u < 1$).

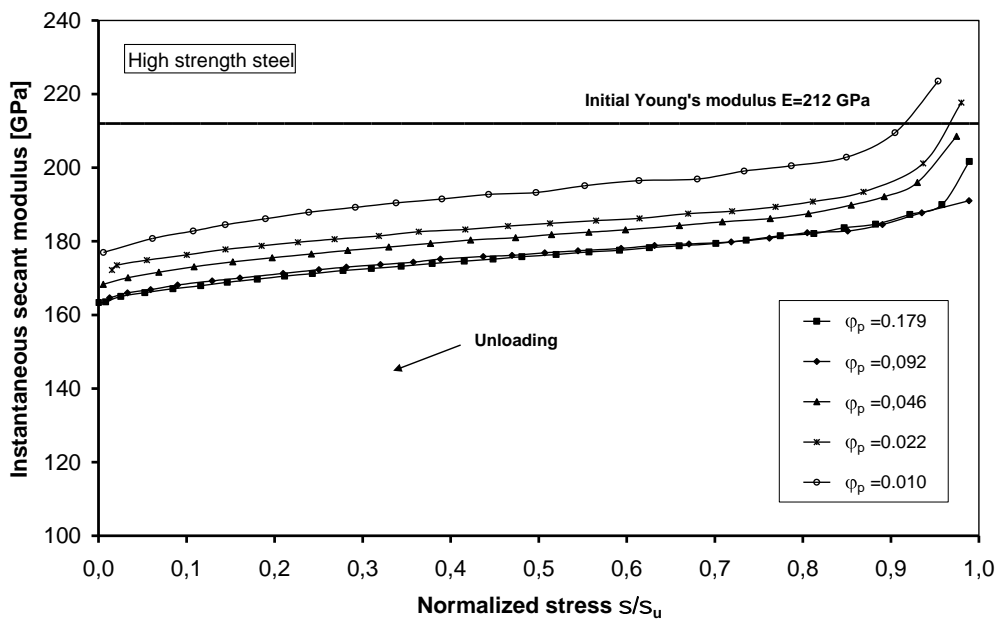


Fig.2.4.25. Instantaneous secant modulus of unloading for high strength steel sheet

From the macroscopic point of view, when a material undergoes a plastic deformation the work done on the material (the mechanical energy supplied) is partially stored and partially dissipated. The energy is stored in form of elastic and inelastic energy, only the former being recoverable in isothermal processes during the load removal. The inelastic energy is related to the internal stresses induced by plastic deformation and to the dislocations mechanism. A key role is played not only by the density of the dislocation network, which increases with the monotonic plastic deformation until a saturation point is reached, but also by the arrangement of the dislocations, which are not randomly dispersed and tend to form dislocation structures. When the load is reversed, the dislocations structure is first annihilated and then rebuilt in the reverse direction. The evolution of the dislocation density depends upon the accumulated inelastic strain and is sensitive to direction changes[52].

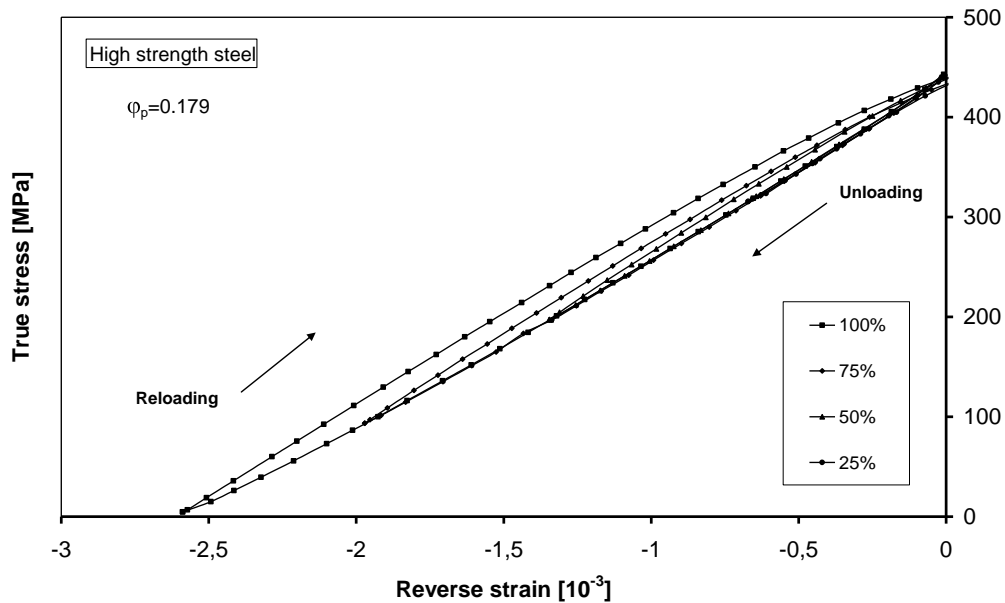


Fig.2.4.26. Partly unloading and reloading of high strength steel specimens

In the theory of mechanical processes, the recovery is elastic, but analyzing the obtained experimental results, it can be stated that strain recovery is not purely elastic and it assumes that inelasticity is micro plastic in nature. Cleveland et al., [51] assumed that during the unloading at microscopic level complex mechanisms of strain recovery take place which are responsible for the inelastic behavior. It is assumed that the existence of additional strain besides the elastic part is driven by the contraction of the crystal lattice, which is unable to hold together the large number of mutually repelling mobile dislocation introduced during straining. The drastically decrease of the Young's modulus at the beginning of unloading is assumed to occur due to dislocation structure annihilation and rebuilding in the reverse direction. The release of the dislocation from pile-ups and respectively from tangles, characterize the second and third stage of the unloading Young's modulus evolution.

We assume that the inelastic effect of unloading is caused by differences between stored energy of cold work after and before load removal, which occurs in case of large prestrain values. Recent findings [53] about discrete dislocation plasticity of the stored energy of cold work showed that for long range stresses the unloaded state has a stored energy smaller than the loaded case, which means that an additional energy is released during the unloading. It was found that, for a sufficiently large prestrain, the dislocation density increases during unloading while the stored energy decreases. The calculations showed that when long range stresses are present the dislocation density does not fully characterize the state of material. The stored energy of cold work depends on details of the dislocation structure, or more generally, on how the dislocations are arranged in the material. Even for nearly similar dislocation density in the loaded and unloaded states, for long range stresses, the unloaded state has a stored energy smaller than the loaded case. Berzerga et al. [53] stated that there is a connection between the stored energy of cold work and what they expressed as Bauschinger effect (reverse yielding occurring while $\sigma > 0$), which corresponds actually to the inelastic unloading. Furthermore, the magnitude of this effect increases with increasing strain and there is a particularly rapid increase in the later stages of the calculated deformation.

The experimental results presented in this paper are consistent with the calculations conclusions in[53]. Supplementary energy release apart from recoverable elastic energy is associated with an internal stress state and is responsible for the inelastic recovery by unloading. The inelastic effect has a non-linear evolution and increase with increasing of the prestrain.

Simultaneous presence of elastic and inelastic recovery allows decomposing the instantaneous secant Young's modulus of unloading E into the elastic part, represented by initial E_0 modulus, in the undeformed state, and a part combining damage and inelastic (micro plastic) effects.

$$\begin{aligned} E &= E_0 - \Delta E \\ \Delta E &= \Delta E_{damage} + \Delta E_{inelastic} \end{aligned} \quad (2.4.24)$$

where ΔE is the change in E -modulus due to loading and unloading, ΔE_{damage} change in E -modulus due to the plastic prestraining and relaxation and $\Delta E_{inelastic}$ is the change in E -modulus only in the unloading state. At the beginning of unloading E -modulus has the value $E_{damage} = E_0 - \Delta E_{damage}$. Assuming isotropic damage due to the plastic prestraining φ_p , the damage variable ω ($0 < \omega < 1$) can be specified as $\omega = 1 - E_{damage} / E_0 = \Delta E_{damage} / E_0$ and respectively $\Delta E_{damage} = \omega E_0$.

Noting that the instantaneous secant modulus increases with the stress decrement $\sigma_u - \sigma$, its total change, including both damage and inelastic effects, was found to be well expressed by the equation:

$$\Delta E = A \cdot \exp \left[B \left(1 - \frac{\sigma}{\sigma_u} \right) \right], \quad (2.4.25)$$

where A is a parameter depending on prestrain value and B is a material constant. Parameter $A = \Delta E_{damage}$ has a physical value and represents the decrease in E -modulus with respect to E_0 at the beginning of unloading ($\sigma = \sigma_u$).

According to the presented experimental observations, ΔE decreases with the increase of prestrain level and when the prestrain becomes large enough approaches its saturated value. The evolution of parameter A can be described by an exponential function of prestrain as:

$$A = A_{sat} (1 - \exp(-C \cdot \varphi_p)), \quad (2.4.26)$$

where A_{sat} stands for saturated value of A at infinitely large plastic strain and C is a material constant that controls the rate of parameter evolution. The values of these materials constants determined by curve fitting, for the high strength and low carbon steel sheets, are listed in Table 2.4.4.

Table 2.4.4. Material constants in Equation (2.4.27)

Material	E_0 (GPa)	A_{sat} (GPa)	B	C
H320LA	212	28	0.5	70
DC04	200	11	1,2	120

Thus, the instantaneous secant Young's modulus of unloading can be represented as a function of initial Young's modulus, accumulated prestrain, unloading stress decrement and three material constants:

$$E = E_0 - A_{sat} \left(1 - \exp(-C \cdot \varphi_p)\right) \cdot \exp\left[B \left(1 - \frac{\sigma}{\sigma_u}\right)\right]. \quad (2.4.27)$$

From Equation (2.4.27) the stress-strain response during unloading of the steel sheets can be reconstructed for a known prestrain and stress value. The instantaneous tangent modulus results by calculating the derivative of the secant modulus of unloading.

In Figure 2.4.27 is depicted the change in secant modulus with prestrain for full unloading ($\sigma = 0$) of the high strength steel specimen. The figure contains both experimental and simulation results.

In this study it has been shown that the full-field and real time technique of the ESPI is eminently suited to analyses the strain recovery by unloading of the steel sheets for cold forming. High precision of strain measurement, no-contact, non-destructive and full-field information are major advantages of the method in comparison with other measurement techniques. The application of ESPI to precise measurement the Young's modulus of unloading gives the possibility to view in another perspective the unloading response of the steel sheets undergoing large plastic deformation.

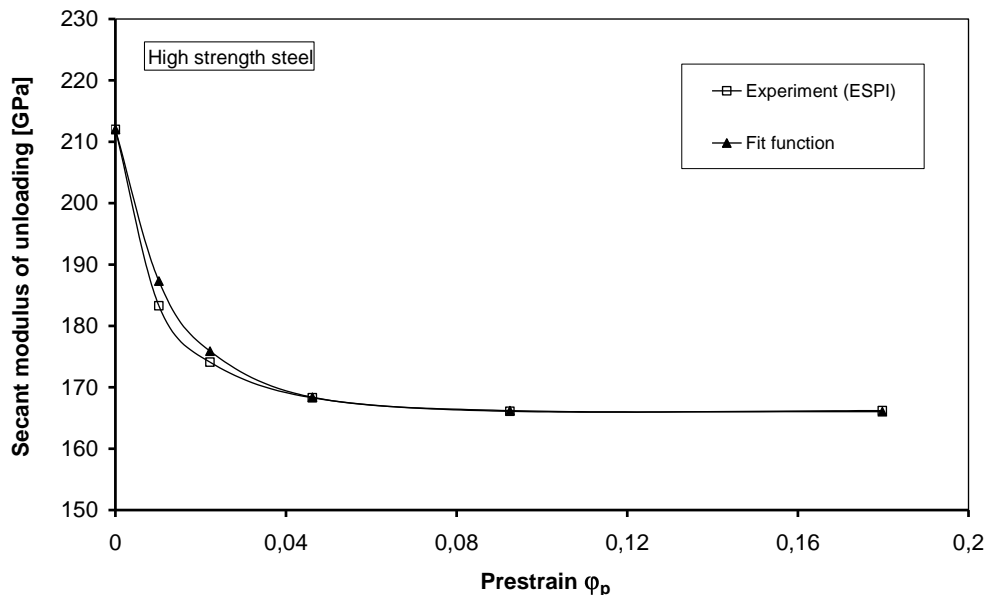


Fig. 2.4.27. Secant modulus of unloading in dependence with prestrain value for the high strength steel

For the steel sheets samples stretched to large prestrain value (18%) the measured strain recovery exceeded the expected linear recovery by about 25% for the high strength steel (H320LA) and 21% for the low carbon steel (DC04) [54]. The unloading Young's moduli decrease with the increase in total amount of prestrain and the influence of the prestrain path upon inelastic strain recovery is minor. When the prestrain values become large enough they approach their asymptotic values (saturated values). It can be assumed that strain recovery is not purely elastic and is micro plastic in nature. The inelastic effects are caused by the mobile dislocation response after the load removal and the arrangement of the dislocations structure. In case of long range stresses there is a difference between stored energy of cold work after and before load removal[53].

We assume that supplementary energy release, apart from recoverable elastic energy, is responsible for the inelastic recovery by unloading. The influences of the accumulated prestrain value, unloading stress decrement and initial value upon secant modulus of unloading were quantified in an empirical relation describing very well its evolution [45].

Prediction of springback considering an inelastic strain recovery by unloading instead of linear elastic theory is significantly improved. Including a “variable” E-modulus in a material model describing the springback effect brings it more closely to reality[55].

The measurement of both components of in-plane strain recovery during unloading and the analysis of the Poisson’s ratio evolution can be carried out with a two dimensional speckle interferometry system in a similar way. Full-field strain data will offer interesting information especially in biaxial testing.

2.5. Digital Image Correlation

2.5.1. Introduction

Correlation analysis of grey scale video patterns is an optical full-field measuring and characterization method based on video image acquisition and digital image processing. Digital image correlation methods (DIC) first have been developed and applied in the early 1980s and had a major impact in the field of mechanics of solids and structures and it is still undergoing very interesting developments [56-58]. The idea is to measure the displacement fields of surfaces of stressed specimens and structures from images acquired at different stages of loading. A specific advantage of this tool is that it exploits numerical images that are usually acquired by optical means. Comparatively with other optical techniques to measure displacements where light modulation produces fringe patterns and these patterns contain phase information that can be decoded, in DIC displacements are directly obtained from point trajectories and the process of fringe unwrapping is bypassed. Imaging devices have made in the last years significant progress both in terms of quality and definition and also in affordable cost [8, 18].

The correlation analysis of grey scale video images offers a lot of possibilities for non-destructive evaluations in a wide field of materials science and production technology. The evaluation of deformation of materials, structures and components due to thermal and mechanical loading, the derivation of material parameters such as elastic properties and CTE's, the evaluation of the deviation of an object's position as well as the detection of structural or micro-structural changes of optically perceptible surfaces are only few of the established application possibilities.

DIC can easily be used at different scales of space and time to the extent that it relies on principles applicable to pictures obtained by very different imaging systems. It is nowadays possible to use images shot by fast and ultra-fast cameras at timescales down to the microsecond or less [59, 60], acquired by a scanning electron microscope (SEM) or an atomic force microscope (AFM) at nanometric scales [57], but also satellite images at geophysical scales [8]. Multi-camera systems give access to three-dimensional (3D) shapes and displacement fields of the surfaces of an observed object [61].

The methods had a significant growth in popularity in the last decade. There are a plenty of papers and studies based on this method. The author took its first contact with the method at the beginning of 2003 as an alternative to ESPI. Since then were published the following papers in the proceedings of international conferences or journals:

1. **Dudescu, C.**, Botean, A., Hărdău, M., Bal, N. (2014): *Measurement of thermoplastics tensile properties using digital image correlation*, Key Engineering Materials, vol. 601 (2014) pp. 33-36, DOI: [10.4028/www.scientific.net/KEM.601.33](https://doi.org/10.4028/www.scientific.net/KEM.601.33).
2. Chiorean, R., **Dudescu, C.**, Pustan, M., Hardau, M. (2014): *Deflection determination of V-beam thermal sensors using Digital Image Correlation*, Key Engineering Materials, vol. 601 (2014) pp. 41-44, DOI: [10.4028/www.scientific.net/KEM.601.41](https://doi.org/10.4028/www.scientific.net/KEM.601.41)
3. **Dudescu, C.**, Botean, A., Hardau, M. (2013): *Thermal expansion coefficient determination of polymeric materials using digital image correlation*, Materiale Plastice **50** (1) pp. 55-59.
4. Chiorean, R., **Dudescu, C.**, Pustan, M., Hardau, M. (2014): *Deflection determination of V-beam thermal sensors using Digital Image Correlation*, Key Engineering Materials, vol. 601 (2014) pp. 41-44, DOI: [10.4028/www.scientific.net/KEM.601.41](https://doi.org/10.4028/www.scientific.net/KEM.601.41)

5. **Dudescu, M.**, Botean, A., Hărdău, M. (2009): *Application of digital image correlation for measuring e-modulus of wood beam*. Annals of DAAAM for 2009 & Proceedings of 20th DAAAM International Symposium "Intelligent Manufacturing & Automation: Theory, Practice & Education", Vienna, Austria, 25-28th November 2009, pp.42-44, ISBN 978-3-901509-70-4 (ISI Proceedings).
6. **Dudescu, M.**, Botean, A., Hărdău, M. (2009): *Digital image correlation method applied to material testing*. In: Proceedings of the 26th Danubia-Adria Symposium on Advances in Experimental Mechanics, September 23-26, 2009, Leoben, Austria, pp. 45-47, ISBN 978-3-902544-02-5 (Google Scholar).
7. **Dudescu, M.**, Botean, A., Hărdău, M. (2008): *Applications of 3D digital image correlation in experimental mechanics*. In: Proceedings of the Dantec Dynamics 15th International Conference and User Meeting, Schloss Großlaupheim, Sept. 22nd – 23rd, 2008, Ulm, Germany (Google Scholar).
8. **Dudescu, M.**, Botean, A., Hărdău, M. (2008): *E-modulus measurement of wood beams using digital image correlation principle*. In: Proceedings of the 12th International Symposium of Experimental Analysis and Testing of Materials, October 24-25, 2008, Galați, Romania, pag. 123-126, ISSN 1224 - 5615. Indexed: CSA Illumina.
9. **Dudescu, M.**, Botean, A.I. (2007): *Deformations measurement using digital image correlation principle*. Acta Technica Napocensis, nr. 50/2007, pp. 21-24, Editura U.T.Press Cluj-Napoca, ISSN 1224-9106.

2.5.2. Two-dimensional Digital Image Correlation principle

To use the grey scale correlation method it is necessary to acquire (at least two) images of different states of the objects under investigation. In common applications standard video equipment and video digitizers (frame grabbers) can be used to generate grey scale images of the reality scenes to be analysed. To solve more sophisticated measuring tasks, high resolution or high speed cameras are applied. The combination of the image correlation method with microscopic and nanoscopic imaging techniques, such as light microscope, laser scanning microscope or atomic force microscope opens interesting new approaches to micro- and even nanoscale deformation and motion analysis.

The digitized images acquired from the object under investigation at a reference state and (at least) one different second state are compared one to each other using a special algorithm, that is applied to small local submatrices taken from the image matrices (Fig. 2.5.1) in the local surrounding of a desired measuring point. The comparison is performed by means of two-dimensional cross correlation analysis applied to local "grey" (in this case intensity) scale submatrices taken from the reference and the comparison image in the surrounding of predefined measuring points[62, 63].

The relative shift of the searched local reference area (reference matrix, containing the local grey scale structure) in the compared pattern is determined with the help of the maximum cross correlation coefficient. The cross correlation coefficient K gives a measure of similarity between grey scale intensity patterns of images 1 and 2, which have the same size of the kernel. A correlation coefficient is calculated for all possible displacements of the reference matrix within the (larger) analysed image region, the K coefficient can be expressed:

$$K_{i'j'} = \frac{\sum_{i=i_0}^{i_0+n-1} \sum_{j=j_0}^{j_0+n-1} (I_1(i, j) - M_{I_1}) (I_2(i+i', j+j') - M_{I_2})}{\sqrt{\sum_{i=i_0}^{i_0+n-1} \sum_{j=j_0}^{j_0+n-1} (I_1(i, j) - M_{I_1})^2 \sum_{i=i_0}^{i_0+n-1} \sum_{j=j_0}^{j_0+n-1} (I_2(i+i', j+j') - M_{I_2})^2}} \tag{2.5.1}$$

where: $I_{1,2}$ are the intensity gray values of the pixel (i,j) in the load state images 1 (reference or undeformed) and 2 (deformed) and $M_{I_{1,2}}$ the average gray value over the kernel size, respectively. Values i' and j' indicate the integer part of the displacement of the reference matrix within values have to be determined for all displacements the analyzed region of load state image 2 given by $-(N-n)/2 \leq i', j' \leq (N-n)/2$, assuming quadrangle kernel and search matrix sizes $K_{i'j'}$.

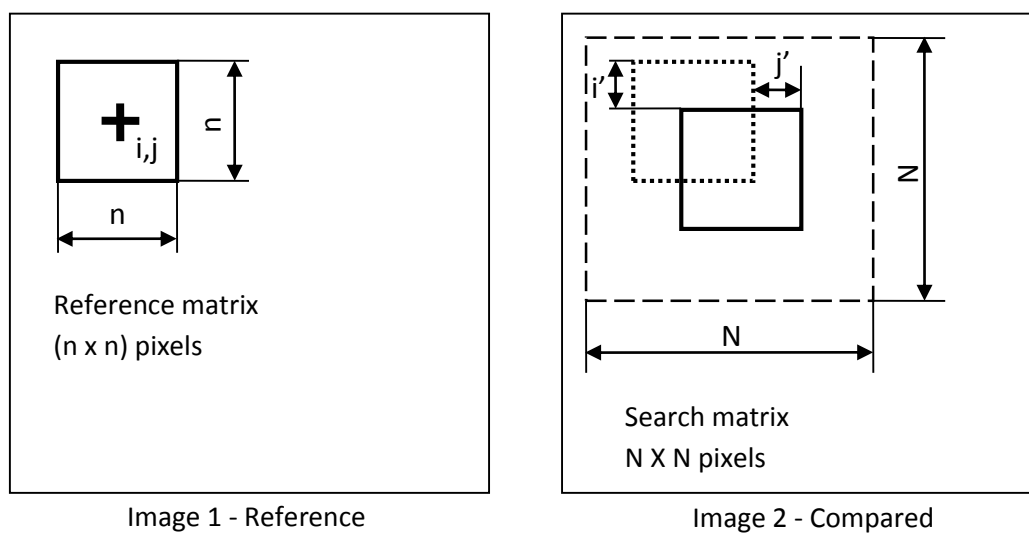
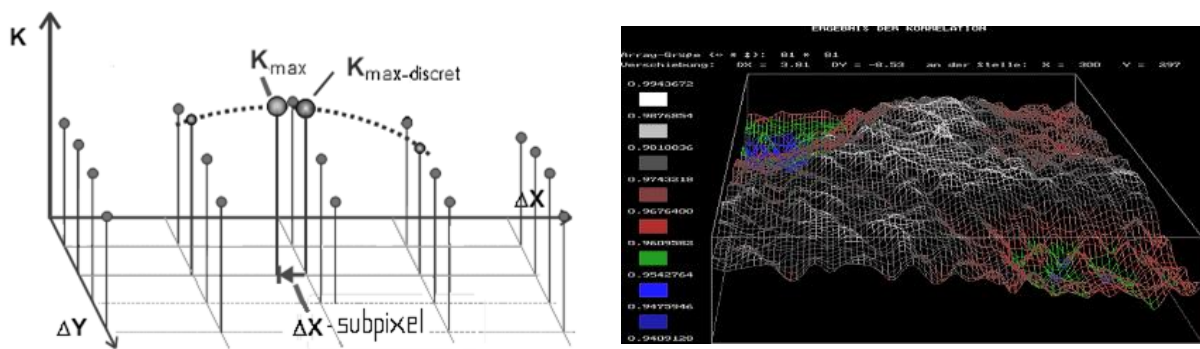


Fig. 2.5.1. Two-dimensional cross correlation analysis

This algorithm gives a two-dimensional discrete field of correlation coefficients defined only at integer pixel coordinates (i,j) . The discrete maximum of this field is interpreted as the location, where the reference matrix is shifted from its position in the first (reference) image (Fig. 2.5.2.a).



a) b)
Fig. 2.5.2. Discrete field of correlation coefficients

The accuracy of the displacement evaluation is improved in a second calculation step using a special subpixel algorithm. A simple and quick way to find a value for the non-integer subpixel-part of the displacement is the search for the maximum of a parabolic approximation of the discrete function of correlation coefficients in the close surrounding of the maximum coefficient K (Fig. 2.5.2.b).

Alternative approaches to subpixel accuracy are based on cross correlation analysis in submatrices with artificially enhanced resolution that are calculated from the initial images by linear, bilinear or spline interpolation in the intensity matrix.

The result of the two-dimensional cross correlation and subpixel analysis in the surrounding of one measuring point (represented by the coordinates of the middle point of the investigated submatrix) gives the two components of the projection of the displacement vector into the image plane at the corresponding surface point of the object under investigation. Applied to a set of measuring points (e.g. to a rectangular grid of points with user-defined pitch), this method gives the in-plane displacement field. For real values it is obviously necessary to convert pixels in length unit.

These results can be displayed in the simplest way as a numerical list, which can be post processed using standard scientific software codes, but - due to specific software implementation - also in different graphic representations (vectors, superimposed lattices – Fig. 2.5.3 - or color scale coded representation [64]).

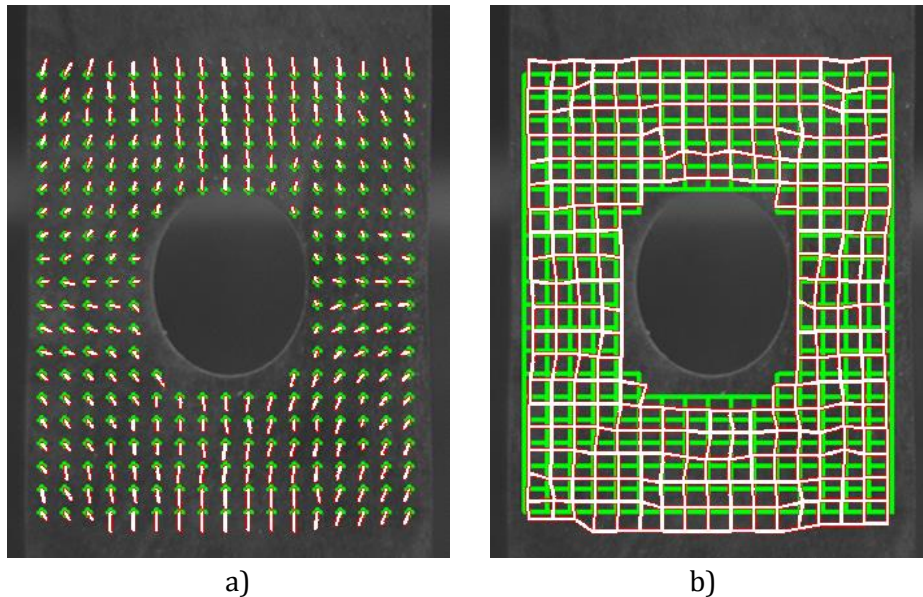


Fig. 2.5.3. Graphic representation of the DIC results: a) vectors; b) superimposed lattices

The resolution of the displacement measurement $\delta u_{x,y}$, defined by the object-site field-of-view length $l_{x,y}$, the pixel amount of the CCD image sensor in vertical (n_y) and horizontal (n_x) direction and the subpixel shift resolution k , is given by equation (2):

$$\delta u_{x,y} = \frac{l_{x,y}}{n_{x,y}} k \quad (2.5.2)$$

The subpixel shift resolution k is a measure of the available displacement resolution and strongly depends on the experimental conditions, the quality of the images obtained in the experiment (noise, sharpness, optical distortion etc.) and the quality of the algorithms that are used to calculate them from the given initial image data. The value k varies in most practically

relevant cases between $\frac{1}{4}$ to $\frac{1}{10}$ for the resolution of the displacement of a single measuring point. For calculation results obtained by the stochastic analysis of multiple point measurement (e.g. rigid body displacement calculated as the mean value of shifts measured at multiple points, linear elastic strain calculated from the slope of a regression line), resolutions equivalent to 0.01 pixels and better are reached. Assuming typical values of the field-of-view $l = 100$ mm, the side length pixel number of the camera chip $n \times n = 1024 \times 1024$ pixels and the measurable subpixel shift resolution $k = 0.1$ (estimated), a measurement resolution of a single point displacement measurement down to $10 \mu\text{m}$ can be reached. 3D-displacement field measurements are possible by combining the digital image correlation analysis with stereo image acquisition and photogrammetric algorithms.

2.5.3. Three-dimensional Digital Image Correlation

In the 3D digital image correlation technique, random gray value dot patterns on specimen surfaces are observed by two cameras from different directions in a stereoscopic setup (Fig. 2.5.4), the position of each object point being focused on a specific pixel in the camera plane [61, 65]. With the knowledge of the imaging parameters for each camera (intrinsic parameters: focal length, principle point and distortion parameters) and the orientations of the two cameras with respect to each other (extrinsic parameters: rotation matrix and translation vector), the position of each object point in three dimensions can be calculated. Using a stochastic intensity pattern on the object's surface, the position of each surface point in the two images can be identified by applying a correlation algorithm. By using this correlation algorithm, a matching accuracy of the original and the transformed facet of better than 0.01 pixel can be achieved [66]. The stochastic pattern can be applied easily with a colored spray paint, printing or other transfer methods. The size and distribution does influence the achievable resolution.

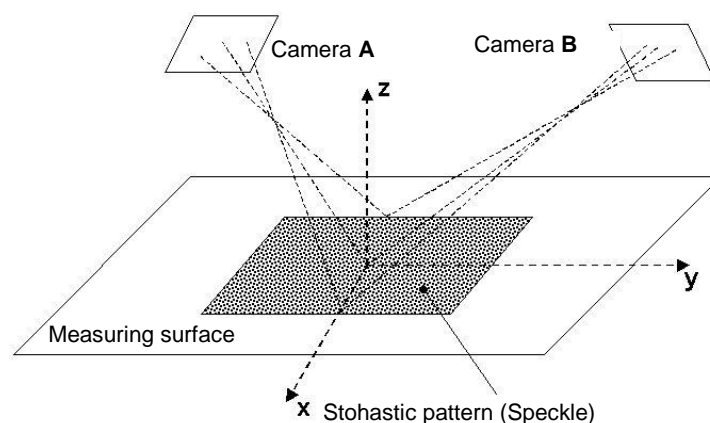


Fig. 2.5.4. Principle of 3D-DIC with two cameras

The process of determining the projection parameters (intrinsic and extrinsic imaging parameters) is described as the calibration process. Images of a target with a known accurate pattern are recorded with both cameras simultaneously. The system displays in real-time the tracking of target markers and automatically acquires a sequence of images of the target

positioned at different angles. From this sequence of images the projection parameter of the whole system, with additional distortion parameter, is calculated based on the pinhole model. The quality of the measurement is directly related to the accuracy of the projection parameters and by simplifying the calibration process and providing quality feedback in this process, accurate measurements can be assured. Typically eight images are sufficient to calculate all calibration parameters accurately.

The digitized images are compared to match subsets (facets) from one image to another by using an image correlation algorithm. Typically a facet size between 20x20 and 30x30 pixels is chosen. Knowing the imaging parameters for each camera and the orientations of the cameras with respect to each other, the position of each object point in three dimensions can be calculated. If this calculation is done for every point of the object surface, the 3D surface contour of the object can be determined in all areas, which are observed by both cameras. In order to evaluate surface displacements and strains on the object surface, a series of measurements is taken, while the specimen surface is moved due to a loading. Through the difference between the contours of the object surface corresponding to different loading stages the displacements field of the surface points in the three-dimensional space can be computed. In other words the software follows the gray values inside some facets and transforms their position for both cameras in the 3D coordinate space (Fig. 2.5.5,[65]).

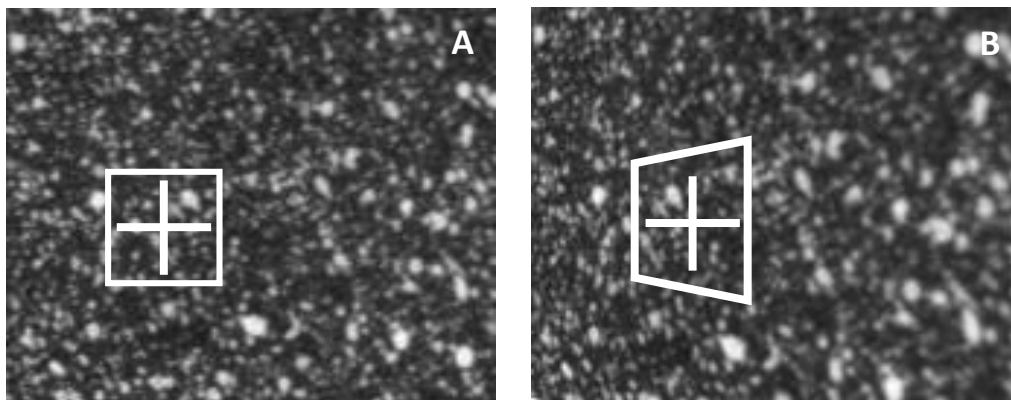


Fig. 2.5.5. Grey value pattern in different images on the camera

The correlation algorithm is based on a pseudo-affine coordinate transformation with 10 variables, where the transformations are described by a combination of translation (a_0, a_4), shear (a_1, a_5), stretch (a_2, a_6), distortion (a_3, a_7) and photogrammetric corrections [66] as described mathematically by the equation (2.5.3).

$$\begin{aligned} x_i(a_0, a_1, a_2, a_3, x, y) &= a_0 + a_1x + a_2y + a_3xy \\ y_i(a_4, a_5, a_6, a_7, x, y) &= a_4 + a_5x + a_6y + a_7xy \end{aligned} \quad (2.5.3)$$

The pseudo-affine transformation coefficients are schematically represented in Fig. 2.5.6.

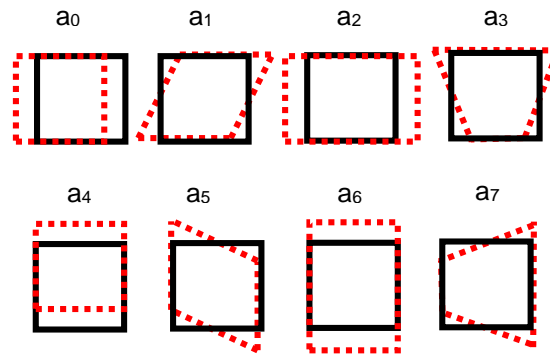


Fig. 2.5.6. Pseudo-affine coordinate's transformation

Within the correlation algorithm the transformation parameters are determined by minimizing the distance between the observed gray value pattern $G_2(x,y)$ in the second image (camera B) and the original pattern $G_1(x,y)$ (camera A) by applying the coordinate transformations (x_t, y_t) plus photogrammetric corrections, which consider different contrast and intensity levels of the images [3]. The value R is a residuum and it's a correlation quality parameter.

$$R = \min_{a_0, \dots, a_7, g_0, g_1} \sum_{x,y} \|G_2(x, y) - G_T(x, y)\| \quad (2.5.4)$$

where $G_T(x, y) = g_0 + g_1 G_1(x_t(x, y), y_t(x, y))$, a_0, \dots, a_7 are affine transformation parameters and g_0 și g_1 represents the illumination parameters.

Schematically the correlation procedure required for displacement measurement is presented in Fig. 2.5.7. Thus for displacements measurement of the analyzed object surface a successive application of correlation algorithm and coordinate transformations for minimum two loading stages are necessary. The Fig. 2.5.7 presents the transformation of a square facet from the perspective of the two cameras according to the two stages of the analyzed object.

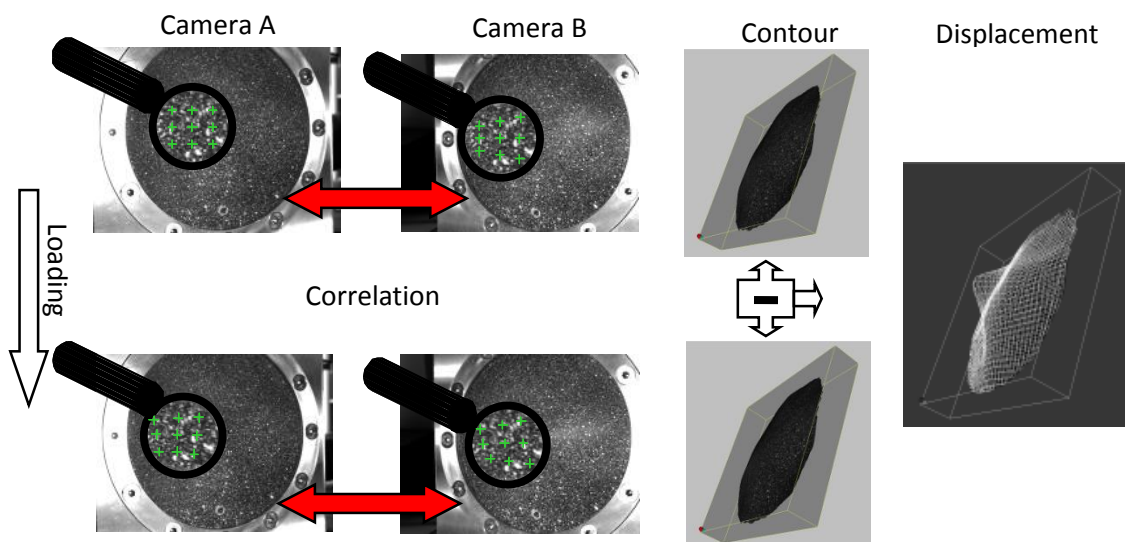


Fig. 2.5.7. Displacement measurement using 3D-DIC

Figure 2.5.8 shows the displacement vector of a surface element. Point P has been displaced from the reference state (undeformed) u in the deformed state v , the element surface is in the time rotated, re-oriented and distorted.

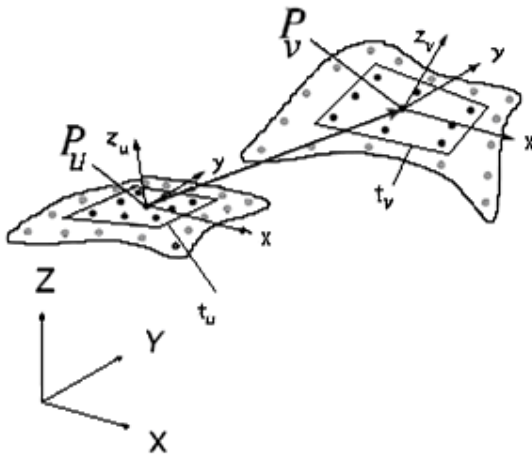


Fig. 2.4.8. Displacement vector of a surface point

By differentiating the displacements of the surface elements one can get the strain of the according facet. For strain calculation the shape (contour) of the object surface is taken into account and the strain values are those determined in the non-linear field of big displacements (Green-Lagrange).

Before any measurement the system calibration is necessary to be performed. The scope of the calibration is to calculate the intrinsic (focal length, principal point and radial and tangential

distortions of the lenses) and extrinsic (translation vector and rotation matrix) parameters of the cameras with respect to a global coordinate system. The system calibration is needed for transforming image positions on the CCDs of the two cameras of a specimen surface point to the corresponding 3D coordinates of that point. Calibration errors are potentially a major source of systematic evaluation errors limiting the resolution of the results [66].

The calibration algorithm makes use of the “Plumb Model” [66]. According to this model the projection of the object point on the CCD is defined by the intersection of the line from the object point through the principle point and the CCD (pinhole model – Fig. 2.5.9.a). The distance of the principle point to the image plane is the focal length and the projection on the image plane gives the position of the optical axis on the CCD. The calibration is done by taking a series of exposures of a calibration target with both cameras simultaneously. The calibration target is a chess pattern with known geometry (Fig. 2.5.9.b). The software detects the corners of the squares. Additional circular markers define the center and the orientation of the target.

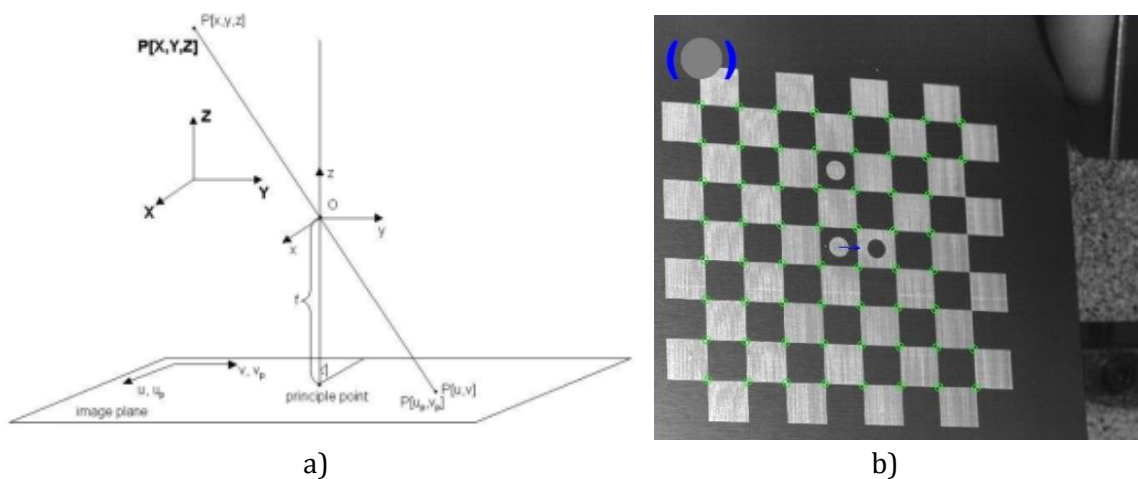


Fig. 2.5.9. Camera calibration: a) pinhole model and b) calibration board

During the calibration process these markers are detected automatically and displayed online on the monitor, while the calibration target is positioned into different spatial orientations. The evaluation algorithm calculates the intrinsic parameters for each camera, the extrinsic parameters as well as the uncertainties of the calibration parameters, resulting from the deviations of the detected markers from the model positions. Typically a total number of eight images are sufficient to calculate all calibration parameters accurately.

2.5.4. Applications of DIC in material characterization

MEASUREMENT OF FLEXURAL MODULUS OF WOOD BEAMS

First study case presents the application of digital image correlation method to determine the E-modulus values of two wood specimens oak (*Quercus robur*) and beech (*Fagus sylvatica*) [67]. Contact measurement of wood specimens using direct applied strain gauges proved to be another experimental techniques that can be employed to determine the mechanical characteristics but a certain correction should be applied [68]. The image correlation technique based on Q400 measuring system developed by Dantec Dynamics (www.dantecdynamics.com) has proven to be a useful tool for contour and deformation analysis. For three-dimensional measurement it uses two cameras (Fig.2.5.10).



Fig.2.5.10. Q-400 measuring system [65]

The Q400 measuring system is very easy to handle. Before any measurement the system calibration is necessary to be performed. The Q-400 system has, for a successful measurement, a calibration procedure incorporated in the measurement and analysis software ISTR4-4D. A test plate with a chess model on it is moved in front of the cameras and the software automatically registers the nodal points of the test blade and calculates the intrinsic (focal length, principal point and radial and tangential distortions of the lenses) and extrinsic (translation vector and rotation matrix) parameters. The experimental set-up was specially designed for testing of wood beams using the procedure of four point bending (Fig.2.5.11). The investigated wood beams have had the dimensions of 20x20x300mm according to the ISO-3349/75 standard. Special devices permitting free rotation of the supports, respectively loading heads were designed (Fig. 2.5.12).

The load was applied by a screw-nut mechanism. The loading frame was completed by a measuring chain supplied by HBM and consisted of a force transducer (U2B-10kN), three

displacement transducers (WA-T/20mm) and the Spider8 amplifier [www.hbm.com]. The three displacement transducers allow additional beam's deflection measurements and determination of the strains based on the beam's curvature. Thus the reliability of the correlation techniques could be proved. The relative deviation between the two methods in the field of big displacements was under 4% and increase when the deflection of the beam is small. It is known that the method of digital image correlation delivers highly accurate results especially in the field of the big displacements.

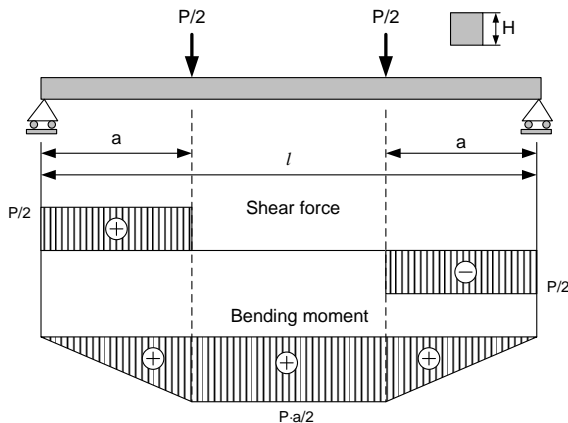


Fig. 2.5.11. Four point bending procedure



Fig. 2.5.12. Experimental set-up

After finishing the calibration according to the above mentioned procedure the measurement required load application on the wood beam and images recording. In this case it was done manually but the system can be operated by an external trigger. The beams, made of oak and beech wood, were stressed in almost equal loading steps until their central deflection reached approximately the value of 3,5mm. This value corresponds to a maximum bending strain of 4000 $\mu\text{m}/\text{m}$.

After evaluation the results consist of 3-D displacements of the analysed object were obtained. Strain calculation should take into account also the contour information to get the in-plane strain. These values are automatically computed by the ISTR4-4D software and displays as color-coded images (similar to FE software) or discrete values in selected points or profiles along desired lines.

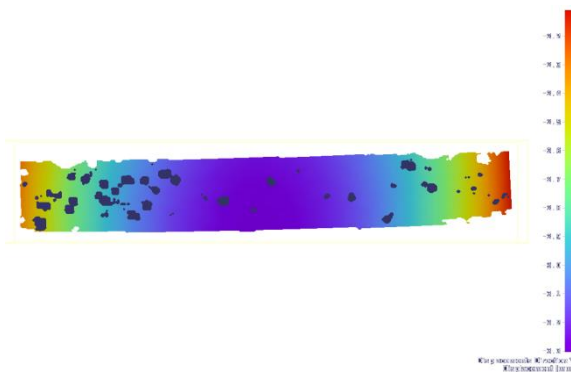


Fig.2.5.13. Vertical displacement distribution in the wood beam (ΔY)

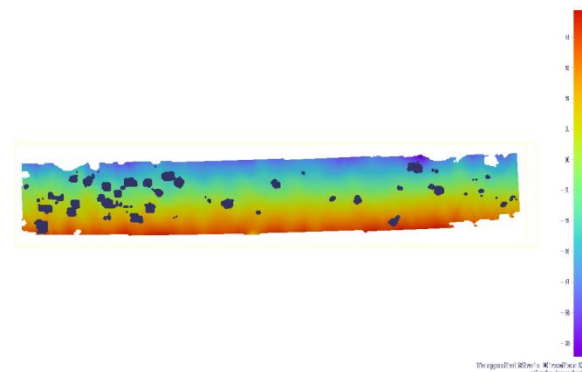


Fig. 2.5.14. Bending strain distribution in the wood beam (ϵ_{xx})

In Fig. 2.5.13 is presented, as color coded image, the vertical displacement distribution (ΔY) of the wood beam. Picking a specific position one can get the deflection of the beam or using so called "gauge function" of the ISTR4-4D software the deflection curve or mean values in a specific area. It can be observed that all values are negative, the Y positive being upwards. Looking at the values it can be noticed also that there is a small rigid body displacement. This effect is due to so called indentation effect and represents the deflection introduced by the supports and the loading head. The ISTR4-4D software has the possibility to remove the rigid body movements. To be sure that the measured values are accurate a comparison with the displacement transducers was performed.

Figure 2.5.14 shows the computed strain distribution in the X direction or bending strains. The color coded values are in mm/m. In both picture some blue spots can be observed. These are areas in which the correlation algorithm cannot deliver accurate data and are automatically masked and eliminated. The stress values can be computed easily by dividing the maximum bending moment to the beam section modulus. Applied force was measured very precisely by the force transducer and the Spider 8 strain gauge amplifier. Having the strain and the stress it can be easily computed the real E-modulus.

In the figures 2.5.15 and 2.5.16 are presented the strain-stress curves obtained by linear interpolation of the discrete measured values for the beech and oak wood specimens.

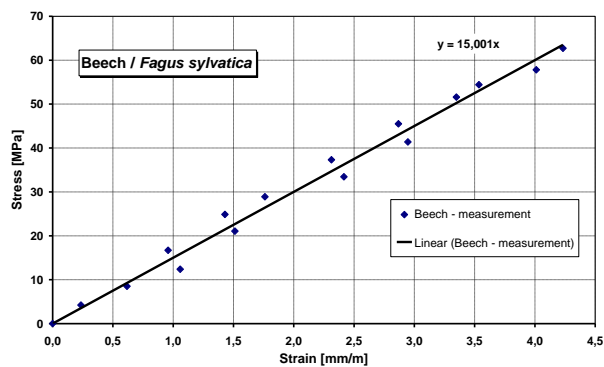


Fig.2.5.15. Strain-stress curve of beech wood

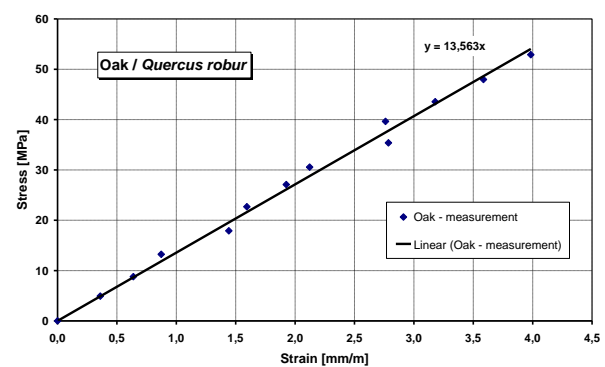


Fig.2.5.16. Strain-stress curve of oak wood

The slope of these curves represents the value of the Young modulus (E-modulus). The values for the two types of investigated wood are presented in Table 2.5.1. In the table are also presented the values of E-modulus given by technical literature or wood standards.

Table 2.5.1. E-Modulus of the investigated wood beams

Wood type	E-Modulus [MPa]	
	Experiment (DIC)	literature
Beech	15000	14000-15700
Oak	13563	13000

The measured E-modulus of the wood specimens showed closer values to those presented in the literature. This validates the experimental method of the image correlation and shows its high potential for material testing, fracture mechanics and component investigation [69]. The measuring system Q-400 from Dantec Dynamics proved to be very accurate and reliable especially in the field of large displacements. Full field information in terms of displacements and strains increase the understanding of the component behavior under loads.

MATERIAL STRAIN-STRESS CURVES BY DIGITAL IMAGE CORRELATION

The second study presents the application of digital image correlation method to determine materials curves and constants (E-modulus, Poisson ratio) [70, 71]. The method was applied for aluminum specimens subjected to tension.

The experimental set-up, presented in figure 2.5.17, consists of the optical measurement system Q400, the aluminum specimen and the tensile test machine type INSTRON 3360 (10kN). The tensile test was conducted according to the EN 10002-1:1990 for tensile testing of metallic materials at ambient temperature. Five specimens having the same dimensions were tested in the same conditions to check if the measuring results can be reproduced. Instead of using a classical extensometer during the tensile test many images of the specimen were acquired by both cameras of the optical measurement system. The values of the corresponding force at the acquisition time were recorded.

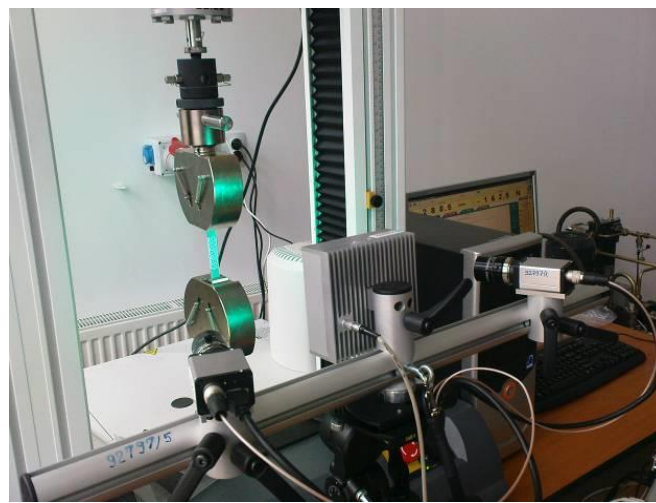


Fig. 2.5.17. Experimental set-up for tensile test

After evaluation procedures the results consisting of 3D displacements of the analyzed specimen were obtained. Strain calculation should take into account also the contour information to get the in-plane strain. In this case the surface was plane and it could be noticed a small rigid body movement of the specimens that were not precisely aligned in the grips of the testing machine. These 2D strain values were automatically computed by the ISTR4-4D software and displays as color-coded images or discrete values in the selected points or along desired lines. Picking a specific position one can get for example the principal strains in that point or using so called "gauge function" of the ISTR4-4D software the mean values of principal strains over measuring steps.

Calculating the engineering stress one can get the strain-stress curve and important information regarding the tested materials. Thus for tested commercial aluminum the measured material constants were Young modulus about 58 N/mm² and Poisson ratio 0.35. The yield stress was about 92 N/mm² and the ultimate stress about 98 N/mm². The measured values had closer values to those presented in the literature. This validates the experimental method of the 3D image correlation and shows its high potential for material testing, fracture mechanics and component investigation. The measuring system Q-400 from Dantec Dynamics proved to be very accurate and reliable especially in the field of large displacements. Full field information in

terms of displacements and strains increase the understanding of the material behavior under loads.

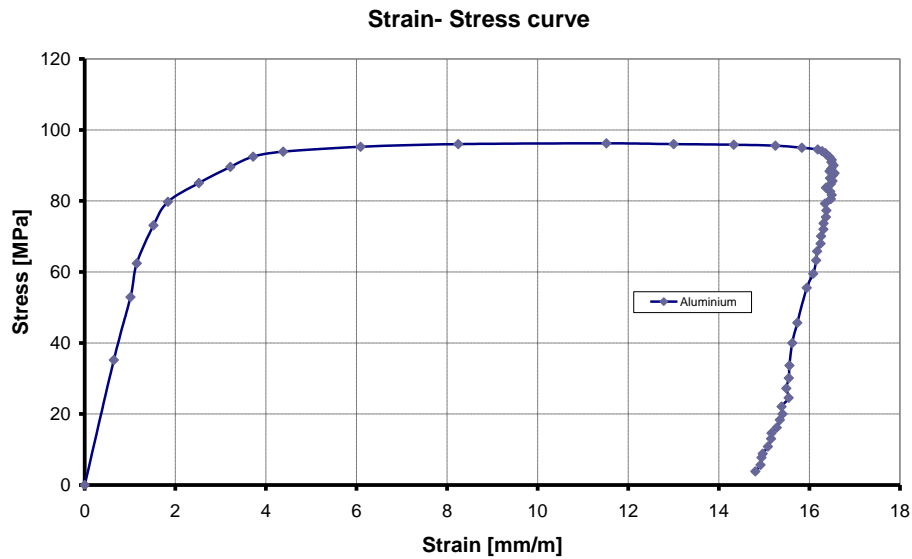


Fig. 2.5.18. Engineering stress-strain curve of aluminum

MEASUREMENT OF THERMOPLASTICS TENSILE PROPERTIES USING DIGITAL IMAGE CORRELATION

Thermoplastic polymers are increasingly used in structures such as automobiles, aircraft, spacecraft pressure vessels or pipes. Knowing the behavior of these materials from the small strain range up to ultimate failure is important for developing adequate material laws necessary in numerical simulations. Because polymers have much more complicated mechanisms of deformation and failure than metals deriving of proper theoretical material models must rely on reliable experimental results which depend on the accurate measurement of the large deformation of polymers. Up to the yield point, most polymers deformed homogeneously, at large strains, in the yield and post-yield regimes, inhomogeneous deformations are observed in many polymers which are not properly recorded by traditional extensometers.

Optical methods of experimental mechanics have been extensively used in the last decade for investigation of the tensile properties of different materials. An optical strain measurement enjoys the advantage of contactless in contrast with the classical clip-on extensometers and delivers full-field strain map of the investigated specimen. For polymeric materials undergoing large deformations the optical method of digital image correlation (DIC) are particularly suitable [72]. Local stress concentrations occurring from the specimen indentation and the bending caused by the weight of an attached mechanical extensometer are avoided. The digital image correlation technique has proven to be a useful tool for investigation of polymers mechanical behavior and provided insight of the non-uniform strain behavior of these materials in the yield and post-yield regimes[73]. Strain fields of two sides of a rectangular tensile specimen was measured using one camera and a right-angle prism [73] or one camera and a mirror to measure fields on both the front and the lateral side of a specimen simultaneously[74]. Three dimensional deformation measurements (3D-DIC) based on two cameras and stereoscopic vision provides both longitudinal and transverse strain distributions

also in the highly strained neck region of the specimen, Young's modulus and Poisson's ratio in the pre-yield regime and the true strain-stress relationships in the post-yield regime can be calculated. A methodology including 3D-DIC has been developed in [75], in order to determine full-field displacements during uniaxial tensile tests on a specimen with rectangular cross section made of a modified polypropylene (PP) compound and in [76] for PP and PP composites.

Rate-dependent large-strain mechanical proprieties of thermoplastic polymers are also of great interest in numerical simulations and cannot be ignored. DIC measurement techniques allow measurement of local strains variation and analysis of local strain rates on deformation performance of polymers. Rate dependent large deformations of the alloy of polycarbonate and acrylonitrile-butadiene-styrene (PC/ABS) was experimentally investigated [77] over a crosshead speed range of 1-3000 mm/min. Based on experimental results a phenomenological constitutive model has been proposed for the glassy polymers in which the effect of strain rate was also considered.

The objectives of the presented work are to characterize using a commercial 3D-DIC measuring system the pre- and post-yield regime of polyvinylchloride (PVC) under uniaxial tension, to compare the results with a classical extensometer and to investigate the rate-dependent large deformation behavior over different crosshead speeds. Based on experimental results a phenomenological constitutive model is implemented.

The investigated material is polyvinylchloride (PVC) produced by Rehau, Germany, and used in the windows frame applications. The tensile tests are conducted according to the EN ISO 527-4: 1997 standard using an Instron 3366 (10 kN) tensile test machine, at room temperature. The specimens were cut out by milling with the dimensions presented in Fig. 2.5.19. The three dimensional DIC measuring system Q400 (www.dantecdynamics.com) has been used to carry out the in-plane and out of plane displacement measurements. DIC measuring principle, calibration procedure and aspects related strain measurement accuracy are described in detail in [70]. Because at higher strains paint will dissolute from the specimen, a pattern was manually applied with a fine marker directly on the specimen's white surface. The specimens are loaded to failure at constant crosshead speeds of 1, 5 and 25 mm/min, which correspond to an initial stretch rate $\dot{\lambda}_0$ of 1.75×10^{-4} , 8.77×10^{-4} and 43.86×10^{-4} 1/s respectively. For the first crosshead speed strain measurement has been captured also with a uniaxial clip-on extensometer (gauge length 10 mm) connected to the tensile test machine.

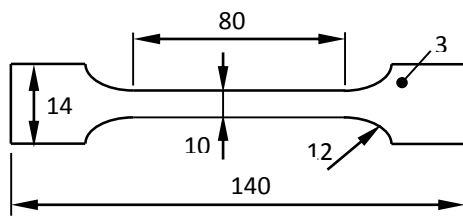


Fig. 2.5.19. Tensile specimen dimensions

The longitudinal ε_x and transversal ε_y true strains are obtained directly from the measuring system. Otherwise if engineering strains ε_e are known the true strains ε can be calculated as function of the local principal strength λ :

$$\varepsilon = \ln(1 + \varepsilon_e) = \ln \lambda. \quad (2.5.5)$$

The local stress was computed knowing the force and the corresponding cross-sectional area. The true stress σ_{xt} are given by:

$$\sigma_{xt} = \frac{F}{A} = \frac{F}{A_0} \frac{A_0}{A} = \frac{F}{A_0} \frac{w_0 t_0}{w t}. \quad (2.5.6)$$

where F is the applied force, A_0 and A are the initial and current cross-sectional area, t and t_0 are the current and initial thickness and w and w_0 are the current and initial width of the specimen.

In the present work the current cross-sectional area is calculated using the transverse strain measured by 3D-DIC and the out of plane displacement of points situated in the analysed cross-section, with the assumption of symmetrical change in the thickness:

$$A = w_0(1 - \varepsilon_y)(t_0 - 2\Delta z). \quad (2.5.7)$$

where Δz is the out of plane displacement of the specimen measured by 3D-DIC system and represents a half of the change in thickness.

Analyzing the full field distribution of the strain field in the necking region, corresponding to maximum tensile strain and minimum cross-section area it can be noticed that shear strain γ_{xy} is zero and the strain in x and y-direction are the principal strains. In this area a square zone was selected using a feature of the 3D-DIC measurement software called gauge function. The mean value over this area of the displacements and strains is calculated and can be automatically exported over the measuring steps. Recording the images acquisition time of each measurement step and correlating them with the force versus time values delivered by the tensile test machine, the corresponding force of each image capture can be obtained.

The true strain-stress curves of PVC tested with different loading speeds are experimentally obtained and depicted in Fig. 2.5.20. The comparative results between the DIC measuring system and the classical clip-on extensometer, shown in Fig. 2.5.21, pointed out the limits of the contact measurement for materials undergoing large displacements until failure and validate the accuracy of the DIC.

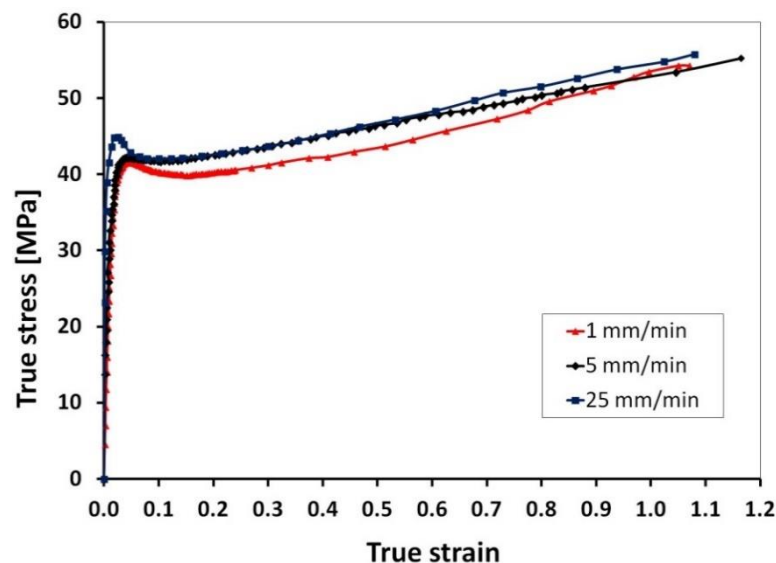


Fig. 2.5.20. True strain-stress curves of PVC tested at different loading speeds

Based on experimental results a phenomenological constitutive model, presented in the literature[77], is implemented (Fig. 2.5.22). The theoretical material model considers the variation of strain rates due to the inhomogeneous deformation behavior of thermoplastic polymer and includes six parameters (material constants) to be identified according to the experimental results.

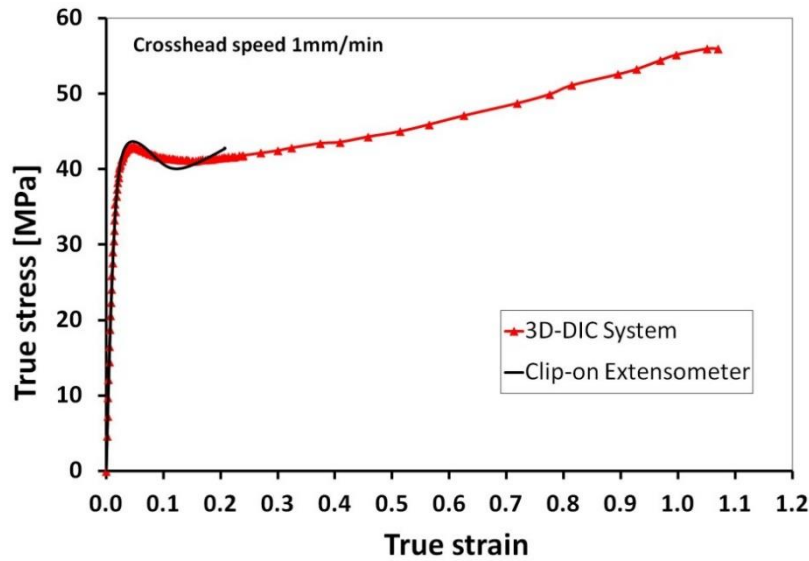
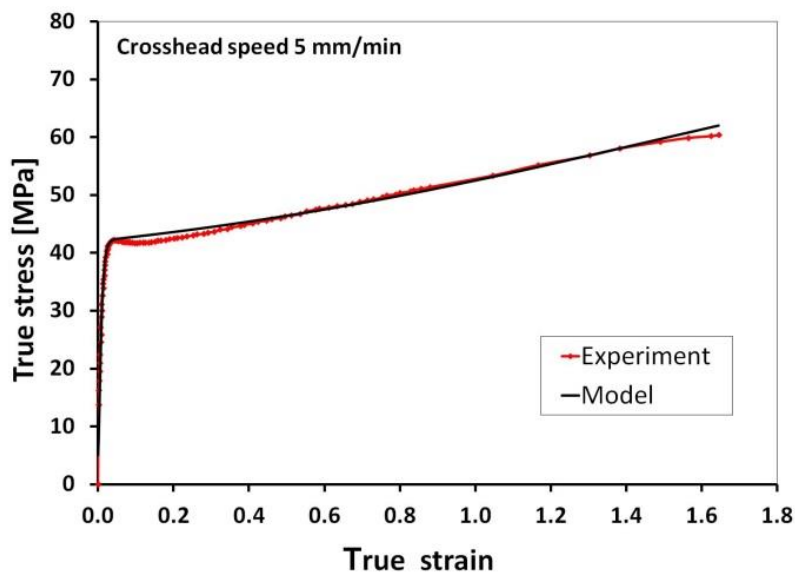


Fig. 2.5.21. Comparative results between DIC and mechanical extensometer

One exponential function was defined to describe the two (elastic and yielding) first deformation stages of the PVC and other function for the after-yielding stage. Combining the two functions by fitting the experimental values the phenomenological constitutive formula for PVC in term of principal stretch rate has been obtained[77].

$$\sigma = \left(A + \eta \ln \left(\frac{\dot{\lambda}_0}{\dot{\lambda}^*} \right) + \mu \exp \left(\frac{\varepsilon}{2} \right) \sqrt{\frac{\dot{\varepsilon}}{\dot{\lambda}^*}} \right) \cdot \left\{ 1 - \exp \left[- \left(B - \kappa \sqrt{\frac{\dot{\lambda}_0}{\dot{\lambda}^*}} \right) \varepsilon \right] \right\} + \left[A + \eta \ln \left(\frac{\dot{\lambda}_0}{\dot{\lambda}^*} \right) \right] \exp \left[- \frac{1}{2} \left(\frac{\varepsilon - \varepsilon_m}{s} \right)^2 \right]. \quad (2.5.8)$$

where A , B , η , κ , s , ε_m are material constants, $\dot{\varepsilon} = \frac{d\varepsilon}{dt}$ is the true strain rate, $\dot{\lambda} = e^\varepsilon \dot{\varepsilon}$ is local principal stretch rate, $\dot{\lambda}_0$ is the initial stretch rate and $\dot{\lambda}^* = 1.0$ [1/s] is the reference principal strain rate.



a)

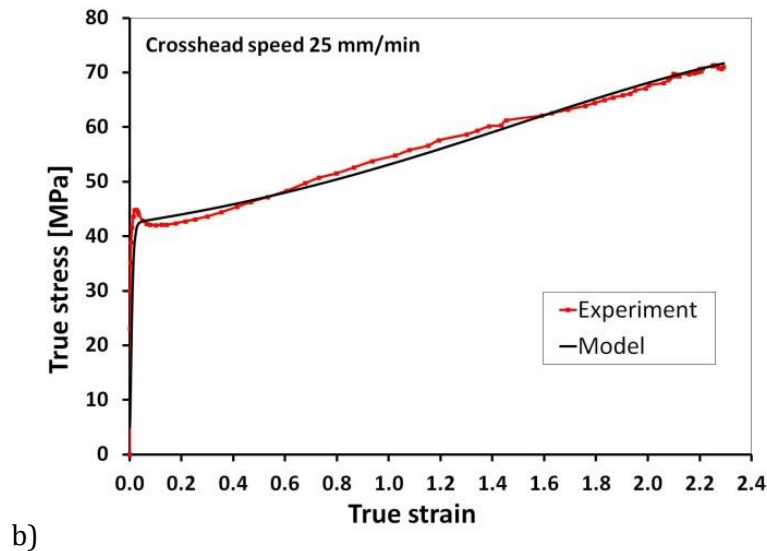


Fig. 2.5.22. Experimental and phenomenological constitutive model for the true strain-stress curve of PVC for a crosshead speed of: a) 5 mm/min and b) 25 mm/min

For investigated PVC specimens the calculated material constants values were: $A=38$, $B=164$, $\eta=0.14$, $\kappa=80$, $s=1.5$ and $\varepsilon_m=3$. The value of μ was set to 2, to reduce the model complexity[77]. The phenomenological model fits well the experimental data. Fig. 2.5.23 shows the comparative true strain-stress curves for the loading speed of 5 mm/min and 25 mm/min, respectively.

The experimental method of 3D-DIC proved to be a reliable technique to characterize the pre- and post-yielding behavior of PVC. Rate-dependent large-strain mechanical proprieties of thermoplastic polymers were investigated by DIC, the method allowing the measurement of local strains variation and analysis of local strain rates on deformation performance of PVC.

The limitations of the measuring system are given on one hand by the frame rate of the cameras and on the other hand by the method accuracy in case of small displacements as that characterizing elastic region measurement. High speed cameras are necessary to investigate the material behavior at higher strain rates.

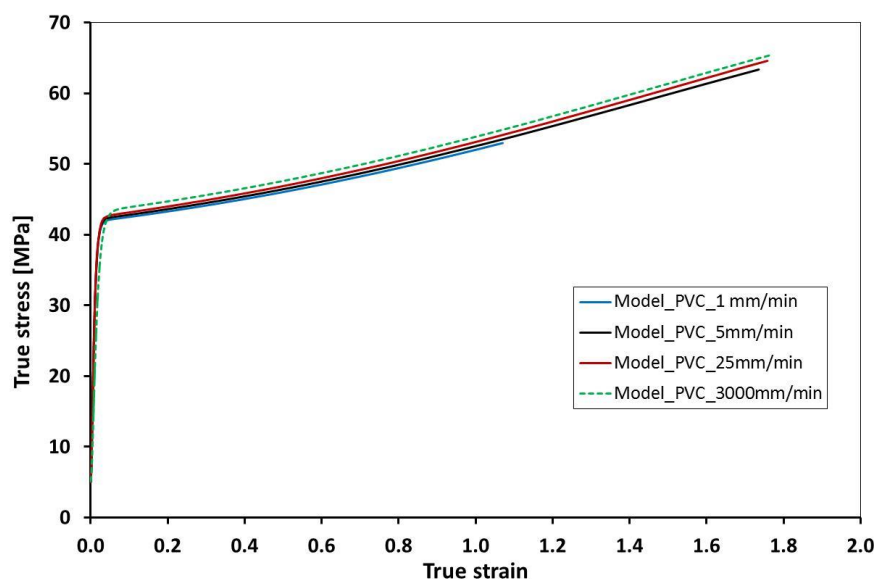


Fig. 2.5.22. Comparative true strain-stress curves for different crosshead speeds

The true strain-stress curves of PVC tested with different loading speeds are experimentally obtained and based on these a phenomenological constitutive model was implemented. The theoretical phenomenological model describes the experimental results well and shows that the effect of the strain rate on the true stress –strain curves is small for lower strain rates but must be taken into account for higher strain rates.

THERMAL EXPANSION COEFFICIENT DETERMINATION OF POLYMERIC MATERIALS USING DIGITAL IMAGE CORRELATION

Knowledge of real material parameters is nowadays a condition for numerical simulations, widely used in industry to design quality components in very short time. The value of the thermal expansion coefficient (CTE) plays a key role in components design, in structure response or in the final decision-related materials selection. It is also desirable to be able to visualize mechanical behavior of materials or components under thermal loads. In the case of plastics these needs are particularly great because of the rapid change within the industry. The plastics in use today are very often not precisely the same as in the past, even if the polymer is basically the same, and there are continuing refinements in processing. Also, plastics are being used in more and more new applications, and frequently more critical applications, than before.

Conventional experimental procedures relying on dilatometers to measure CTE require a set of standard bars. Strain gauge technique can also accurately measure the thermal strain [78] but the measurements are limited to temperatures up to about 120°C with standard strain gauges and free expansion of samples are affected by the wires, disturbing the measurement. In some applications [34] these are not a reliable or easy to apply solutions. Full-field optical techniques like Electronic Speckle Pattern Interferometry (ESPI) proved to be well suited to analyses the thermal expansion behavior and to determine the coefficients of thermal expansion (CTE) for thermally isotropic as well as anisotropic solid materials[34]. The overall accuracy of the CTE measurement by the ESPI method was estimated at $\approx 0.1 \times 10^{-6}$ [1/K]. The drawbacks of ESPI methods consist in its high sensitivity to environmental conditions such as vibrations, thermal convection currents flowing around the specimen and complexity of the measurement set-up.

The digital image correlation technique (DIC) has proven to be a useful tool for contour and deformations analysis of polymeric materials[76], [79] and found in the last years widespread use and acceptance. In the field of thermal properties of materials DIC was used to determine and the CTE of thin films [80], power electronics packaging [81] or tubular steel specimens[82]. A study regarding thermal deformations at high temperature measured by DIC and determination of chromium nickel stainless steel CTE in the temperature range 20°-550° is presented in[83]. The method of DIC is demonstrated to be capable of providing accurate measurements up to 1100 °C, and the potential to monitor strains to 1400 °C was identified[84]. The capability of the method was demonstrated by measuring the Young's modulus and coefficient of thermal expansion of a nickel-base superalloy at temperatures from ambient to 1000 °C[84]. Compared to other methods the DIC enjoys besides of advantages being non-contact and full-field measurement method, to have a simple set-up, low sensibility to environmental conditions, easy post-processing of the measured data, no limits on the temperatures and strains than can be reached.

In this study it is investigated the possibility and accuracy of CTE measurement using a 3D digital image correlation system for two commercial plastics: polypropylene (PP) and

polyvinylchloride (PVC) [85]. The work discusses the CTE calculation of isotropic and anisotropic materials, influence of a small rigid body rotation and analyses the accuracy of strain calculation procedure. In the first part the DIC procedure is explained and the experimental set-up is outlined. The noise contained in the calculated displacements, especially when small displacements are measured, will be amplified if the strains are calculated by numerical differentiation of the displacement field. The possibilities to get more precise and reliable strain results are discussed in the paper and comparative values in case of an aluminum sample are presented. An assessment of the error on the obtained CTE is made at the end of the paper.

The method of DIC is known to reconstruct displacements with subpixel accuracy and tangential surface strains in the $m\epsilon$ range. Accuracy of strain measurement using DIC is presented in a large number of publications, but cannot be generalized for a particular experiment. Comparison with other measuring techniques point out that the strain uncertainty measured by DIC [86], [87], are between 100 $\mu\text{m}/\text{mm}$ and 400 $\mu\text{m}/\text{mm}$. A general agreement is reached for large deformations ($>1\%$) where DIC is especially suitable. According to the tests performed by the producer of Q400 system [88] the displacement errors are present in the order of less than 0.02 pixels, strain errors are limited to 0.2 $m\epsilon$ when using a lens with 17 mm focal length. If present displacements are small (lower than 50 pixels), the errors scale linearly. Relative displacement errors are in the order of 0.01-0.05%, strain errors typically count 1-5 $\mu\epsilon/\text{pixel}$, related to the existent displacements [88].

In the applications presented here, measured strains are in the range of 100-2000 $\mu\text{m}/\text{m}$ which is typically accompanied by a large quantity of noise. If the strains are calculated by differentiating the displacement field the numerical differentiation will amplify the noise contained in the calculated displacements. One possibility to deal with this problem is to average the measured strains over a large area where the strain distribution is supposed to be homogeneous. A better result can be obtained calculating in-plane Green-Lagrange strain components by the analysis of the distortion of each local facet as mentioned above [65] or simply use linear planes to approximate the computed displacement field [80]

$$u_x(x, y) = A_0 + A_1x + A_2y, \quad u_y(x, y) = B_0 + B_1x + B_2y \quad (2.5.9)$$

where A_0, \dots, B_2 are the desired coefficients, $u_x(x, y)$, $u_y(x, y)$ are the discrete displacements component at coordinates (x, y) . The least square method can be applied to determine the A_0, \dots, B_2 coefficients. The strain components can be calculated as

$$\epsilon_{xx} = \frac{\partial u_x}{\partial x} = A_1, \quad \epsilon_{yy} = \frac{\partial u_y}{\partial y} = B_2. \quad (2.5.10)$$

Measurement of the CTE relies on two aspects: accuracy measurement of the thermal displacements by DIC and accuracy of the temperature measurement of the specimen. It is essential for the experimentally determining the CTE that the strain field within the sample to be caused only by the thermal loads and no mechanical restraints on the sample, either external or internal, such that no stresses arise in the body during thermal expansion or contraction. The CTE can be computed when the strain value and temperature change are known. Using the DIC measuring technique, this presumes recording of gray patterns at two different temperatures T_1 and T_2 . Using specific image processing software one can determine the full-field distributions of displacement and strain belonging to ΔT . The CTE is thus given by

$$\alpha = \frac{\epsilon}{\Delta T}. \quad (2.5.11)$$

Anisotropic materials do not undergo a uniform thermal strain if temperature changes. For the composite materials, this effect is formed by the mismatch between thermal behavior of fibers and matrix. In this case the thermal expansion is described by a symmetrical tensor, which has the in-plane components:

$$\alpha_{xx} = \frac{\varepsilon_{xx}}{\Delta T}, \quad \alpha_{yy} = \frac{\varepsilon_{yy}}{\Delta T}, \quad \alpha_{xy} = \frac{\varepsilon_{xy}}{\Delta T}. \quad (2.5.12)$$

Comparable with the properties of the strain tensor the CTE corresponding to a certain direction can be expressed using coordinate transformation equations. Thus, terms as principal thermal expansion coefficients or coefficient of thermal shear can be considered. For example, if the two principal CTE's α_1 and α_2 are known, the CTE at an angle of 45° with respect to the principal directions is given by[34]:

$$\alpha_{45^\circ} = \frac{\alpha_1 + \alpha_2}{2}. \quad (2.5.13)$$

Another known aspect that should be taken into account is the temperature dependence of the CTE $\alpha = \alpha(T)$. Thus, the thermal strain can be expressed as a function of temperature

$$d\varepsilon = \alpha(T) \cdot dT. \quad (2.5.14)$$

Equation (2.5.14), taking account of $\varepsilon(T) = \int_{T_0}^T \alpha(T') dT'$, $\varepsilon(T_0) = 0$, leads to

$$\alpha(T) = \frac{d\varepsilon(T)}{dT}. \quad (2.5.15)$$

Although the CTE is a function of temperature for most materials it can be considered a constant in a large temperature range.

During the thermal expansion an arbitrarily small rigid body rotation of the specimen can occur, the displacement values in x-axis direction become then

$$u_x^r(x, y) = \Delta T [x(\alpha_1 \cos^2 \xi + \alpha_2 \sin^2 \xi) + y(\alpha_1 - \alpha_2) \sin \xi \cos \xi] - y \cdot \Delta \xi, \quad (2.5.16)$$

where α_1 and α_2 are the principal CTE's and $\Delta \xi$ is the rigid body rotation angle (Fig. 2.5.23).

For the measuring direction y , the above equations can be obtained in a similar manner, the expression of displacement $u_y(x, y)$ due to the thermal stress and small rigid body rotation can be written as:

$$u_y^r(x, y) = \Delta T [x(\alpha_1 - \alpha_2) \sin \xi \cos \xi + y(\alpha_1 \sin^2 \xi + \alpha_2 \cos^2 \xi)] + x \cdot \Delta \xi. \quad (2.5.17)$$

In case of isotropic materials $\alpha_1 = \alpha_2 = \alpha$ the displacement components can be rewritten as

$$u_x(x, y) = \Delta T \cdot x \cdot \alpha - y \cdot \Delta \xi \quad (2.5.18)$$

$$u_y(x, y) = \Delta T \cdot y \cdot \alpha + x \cdot \Delta \xi$$

For small deformations, the rigid body rotation angle $\Delta \xi$ can be calculated with the known formula

$$\Delta \xi = \frac{1}{2} \left(\frac{\partial u_y}{\partial x} - \frac{\partial u_x}{\partial y} \right) \quad (2.5.19)$$

The rigid body motions are assumed to be small and they can be easily removed from the DIC procedure by subtracting the displacements of the calculation area centre points.

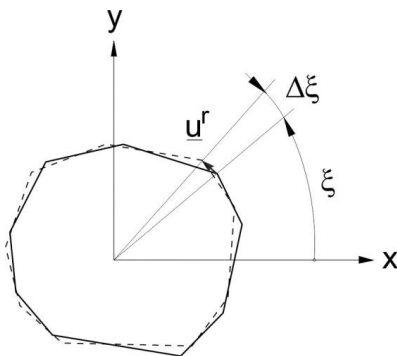


Fig. 2.5.23. Influence of a small rigid body rotation

The measurement of the CTE-tensor by DIC and the validation of the above described theory about the thermal expansion have been performed for a commercial polypropylene (PP) and polyvinylchloride (PVC). The flat specimens were cut out by milling from an office chair (PP) and a windows profile (PVC) of two local producers. Their size was 27 x 27 mm with a thickness of 3 mm (PVC) and 2 mm (PP) respectively.

Accuracy of the method was investigated on a reference flat sample made of aluminum alloy (EN AW 5754) with the same dimensions (27x27mm) and 3 mm thickness. For measurements a random speckle pattern on the surface of the target specimens is necessary. The pattern was produced by black spray applied on an initial painted matt white grounding specimen surface.

Figure 2.5.24 shows the experimental set-up developed to measure in-plane thermal strain of the above mentioned specimens. It consists of three main parts: 3D-DIC measuring system, heating device and temperature monitoring (thermal imaging camera and temperature sensors).

Instrumentation for the 3D digital image correlation consist of the Q400 system from Dantec Dynamics (www.dantecdynamics.com) that includes two CCD cameras, 1/8", 1624x1234 pixel resolution, frame rate up to 30 Hz, control electronic, lenses with 17 mm focal length and patented cold light system HILIS (High Intensity LED Illumination System) for very homogenous illumination of the specimen. Accurate temperature measurement was performed simultaneously by a resistance thermometer type PT 100 connected with HBM–Spider8 data acquisition system and mounted near the test sample and with the thermal imaging camera (FLIR, model T400) for monitoring the temperature value and distribution on the top surface of the specimens.

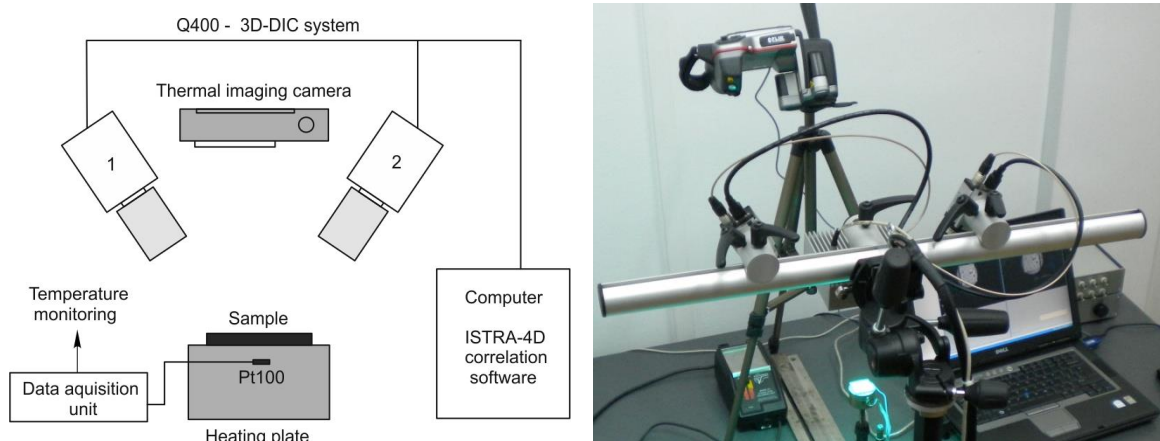


Fig. 2.5.24. Experimental set-up for in-plane thermal strain measurement

Heating of the test samples was achieved with a temperature-controlled soldering station having attached a massive copper cylinder and operating between room temperature and 200°C. In-plane deformations due to thermal expansion at different temperatures were measured by 3D-DIC. Measurements were carried out during heating-up periods, in the interval 20°C to 120°C for aluminum and 20°C to 90°C for plastics (PP & PVC) with a temperature steps of 10°C. Temperature at the measurement step was recorded both with a thermo-resistance and the thermal imaging camera.

Uniform heating of the specimen and precise determination of its temperature at the measurement time proved to be a critical point in connection with computation accuracy of the CTE. There are certain parameters which have to be taken into consideration, such as thermal conductivity and the heat transfer from the heating device to the specimen. Several tests with a thermal imaging system demonstrated that a uniform temperature field can be assumed in the test samples during heating periods (Fig. 2.5.25A). Even for thicker specimens there is a small temperature difference between the bottom surface of the specimen and the top surface of the specimen the temperature difference ΔT is not affected. The effect can be easily removed by keeping the specimen a certain time at constant temperature but the probability that relative movements between the measuring system and sample get also higher. This temperature difference between specimen faces can cause an out-of-plane bending effect that introduces errors in correct evaluation of the in-plane thermal strain field in case of 2D DIC measurement system. The advantage of 3D-DIC is computation of the specimen contours and considering it for accurate strain calculation. In this study the temperature indicated by the thermal imaging camera was used for calculation of temperature difference, ΔT .

From the software adjustable parameters of a DIC system, the most important one affecting the result accuracy is the size of the subsets[89]. Based on previous experience and tests an evaluation grid of 12 pixels with a facet size of 19 pixels and a bi-cubic spline interpolation of the gray values were chosen for evaluation. As expected, in the ideal case of no rigid body rotations, the isolines of x displacements are parallel with y-axis and those corresponding to y displacements with x-axis. Figure 4B shows the total displacement field of one measuring step with removed rigid body rotation. In the background the perspective view of one camera was superimposed. Possibility to automatically remove the rigid body movements given by the measurement software proved to be a very useful tool, most of the measurements being affected by a small specimen rotation or motion.

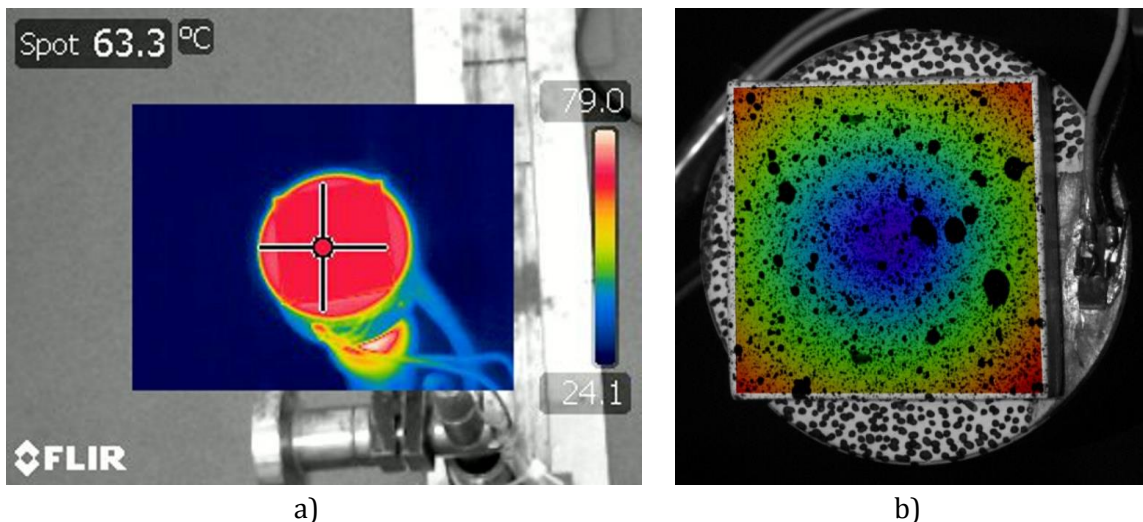
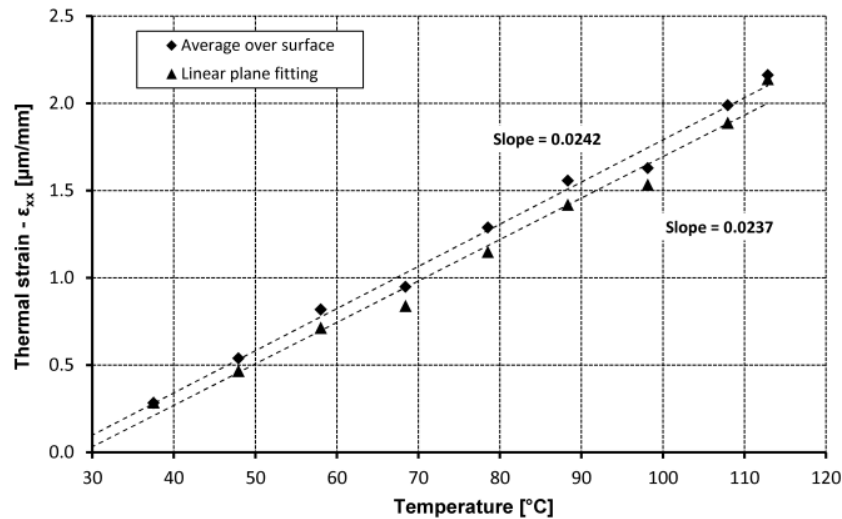


Fig. 2.5.25. Thermal behavior of aluminum sample: a) Temperature distribution acquired with the thermal imaging camera, b) Thermal displacement field

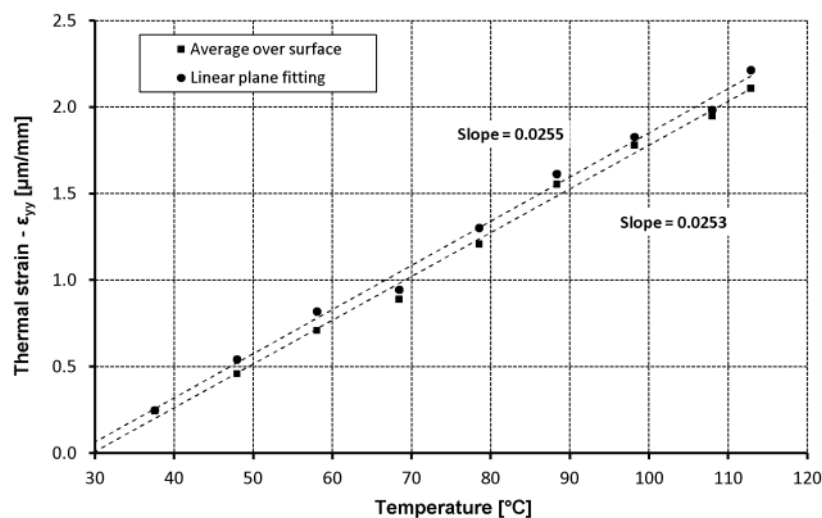
These rigid body motions are assumed to be small, but, in any case, they are removed from the DIC procedure when calculated the strains from the measured displacements field.

As mentioned in the introduction measurement of small displacements using DIC are accompanied by a significant quantity of noise and implicit a decreased accuracy related the calculated strain. One possibility to overcome noise influence in calculating the thermal strains

is to average strains (derived by the analysis of the distortion of each local facet) over a large area or to use a simplified procedure consisting of linear fitting of the measured displacements as presented in [80]. Both procedures to get the thermal strains were compared on an aluminum test sample and presented in Fig. 2.5.26. Analysed area was the entire specimen surface as can be noticed analysing the Fig. 2.5.25B.



a)



b)

Fig. 2.5.26. Variation with temperature of the thermal strains calculated by average over the surface and a linear plane fitting for aluminum sample: a) x direction; b) y direction

Comparing the two thermal strain calculation methods, in case of aluminum sample, the average relative deviation was 9% for x-direction and 7% for y-direction, which is a good agreement. Both methods can be successfully used. A small advantage has strain average over the area because the measuring software have a rigid body removal option and also a so called “gauge” function to get values over a defined polygonal area. The method proposed by Bing [80] requiring manual rigid body rotation removal and successive manual data fitting, being influenced by the plane position. The average of the slopes of the fitting lines is $23.95 \times 10^{-6} / ^\circ\text{C}$ in the x-direction and $25.4 \times 10^{-6} / ^\circ\text{C}$ in the y-direction, respectively. By comparison with the

existed recommended data [15] of $23.7 \times 10^{-6} / ^\circ\text{C}$ ($25 \times 10^{-6} / ^\circ\text{C}$ at 100°C [90]) it is proven that the method of 3D-DIC to get the thermal strain is valid and can be successfully applied on materials undergoing large thermal expansion such as the most of polymeric materials.

The displacement of the aluminum sample corresponding to one measurement step ($\Delta T = 10^\circ\text{C}$) was about $7.2 \mu\text{m}$ but the uncertainty of the measured values decrease from 11% for the first step related to the reference step to 1.1% for the last step with respect to the same reference step. This confirms that for small displacements the accuracy of DIC system is lower but, for materials undergoing large thermal expansion the necessary measurement confidence can be obtained. Measured thermal strains corresponding to a temperature difference of 10°C was about $2.20 \mu\text{m}/\text{mm}$ the strain calculation uncertainty according to the algorithm implemented in the measurement software [88] varying from almost 20% in case of the first step with respect to the reference step to 1.3% for the last step corresponding to a temperature difference $\Delta T = 90^\circ\text{C}$.

It is observed that CTE values in x and y directions are close and also the calculation method by linear plane fitting methods agreed with the average over the area of interest. Both methods can be applied for thermal strain computation, average over the area being easier to be applied in the case of the commercial Dantec Dynamics Q400 measurement system due to its software implementation and reliable strain calculation algorithm. Measured CTE data of polymeric materials are presented in Table 2.5.2. The results are in good agreement with the reported CTE by different producers or literature: for polypropylene ($100 \dots 150 \times 10^{-6} / ^\circ\text{C}$) and polyvinylchloride ($70 \dots 80 \times 10^{-6} / ^\circ\text{C}$).

Table 2.5.2. Measured CTE values of polymeric materials

Polymeric material	CTE - x direction [$\times 10^{-6} / ^\circ\text{C}$]	CTE - y direction [$\times 10^{-6} / ^\circ\text{C}$]	CTE - average [$\times 10^{-6} / ^\circ\text{C}$]
Polypropylene (PP)	136.8	138.1	137.5
Polyvinylchloride (PVC)	73.7	75.3	74.5

In this example it has been shown that the full-field and real time technique of 3D-DIC is suited to analyses the thermal expansion behavior and to determine the coefficients of thermal expansion (CTE) for polymeric materials. The method is recommended to be applied for materials that undergo large thermal expansion, such as polymeric materials. For these materials the precision of CTE determination corresponding to a temperature variation of 70°C is about $2 \times 10^{-6} / ^\circ\text{C}$. A first condition for such a high accuracy is the precise measurement of the thermal strain. There was presented a comparative determination of thermal strain, one based on averaging over the area of interest of the in-plane Green-Lagrange strain components and another by a linear plane fitting of the displacement field. Accuracy of the above strain calculation methods was investigated on a reference flat sample made of aluminum alloy and revealed that both methods can be successfully applied. The second condition for a reliable CTE determination is the precise temperature measurement and control. The temperature monitoring set-up performed simultaneously by a resistance thermometer connected at a data acquisition system and mounted near the test sample and with a thermal imaging camera satisfied the high requirements of temperature measurement of the sample.

Even the accuracy is lower than that measured by interferometric techniques, the DIC enjoys besides of advantages being non-contact and full-field measurement method, to have a simple set-up, low sensibility to environmental conditions, easy post-processing of the measured data, no limits on the temperatures and strains than can be reached[84].

Validating the application of a commercial 3D-DIC measurement system to CTE determination proved to be a good start point to future determination in situ of the thermal behavior of complex polymeric parts used in the industry.

DIGITAL IMAGE CORRELATION FOR THERMAL SENSOR ANALYSIS

An experimental set-up consisting of an image acquisition system for DIC, a temperature measuring unit and a heating source was designed for this study[91, 92]. The block diagram of the experimental set-up is shown in Fig. 2.5.27. The heating of the V-beam sensor is done by the means of a source of hot air flow. The cooling phase is nothing else than free convection to the environmental laboratory conditions. The pictures out of which the deflection is extracted are taken on the downward slope of the sensor's temperature in order to assure thermal equilibrium of the support assembly and a smooth comeback of the sensor to the original, load free, position. The temperature is monitored in real time using a thermal imaging camera and, at certain thresholds, pictures of the deformed sensor are taken with a high resolution camera. The deflection of the sensor is then extracted using VEDDAC 6.0 (<http://www.cwm-chemnitz.de/>) DIC software on the sequence of pictures showing the sensor in the initial, final and intermediate states of deformation (Fig. 2.5.28).

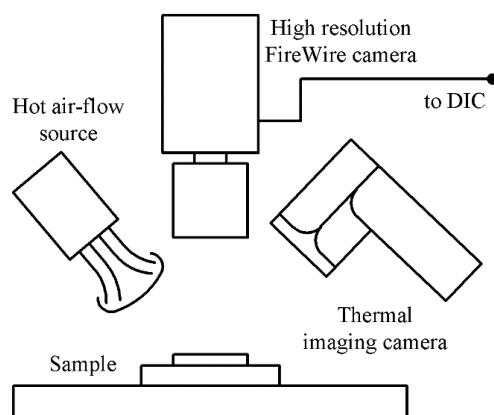


Fig. 2.5.27. Block diagram of the experimental set-up

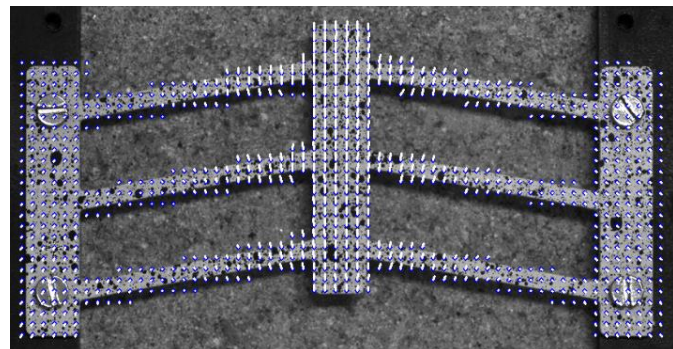


Fig. 2.5.28. Full field displacement of the V-beam thermal sensor

Prior to the measurement of the sensors, a 20x20mm square sample, made of the same aluminium alloy as the rest of the V-beam geometrical types, was tested in order to get the actual coefficient of thermal expansion (CTE) - α . The problems like rigid body movement and rigid body rotation elimination were done for the square and for all the other samples taking into account the method in[85]. The grey scale pattern of raw aluminium was good enough for DIC software to identify the deformation of the predefined points of interest but the thermal imaging camera readings were inaccurate due to the unknown emissivity of the surface. The solution was to cover the samples with two thin layers of matt paint: a base white layer with a stochastic black dots pattern on top. The thickness of the layers of paint has to be reduced as much as possible in order to prevent the appearance of surface flow phenomena due to heating. This preparation of the samples can be avoided if the images are recorded inside a controlled temperature chamber or by attaching a small thermistor to one of the anchors. The latter of the

suggestions creates a small thermal bridge between the sample and the measuring system which affects the heat flow inside the sensor and so it is to be avoided whenever possible. Taking into account all the details described above, the determined CTE was $\alpha = 23.04 \cdot 10^{-6}/^{\circ}\text{C}$. This value was defined in the FE analysis software as a material constant and it was taken into consideration for all the future simulations that were performed.

The experimental results are in good agreement with the FE calculations and the analytical model which proves the reliability of the method. The relative errors between the analytical and the numerical results are less than 6%, while the relative errors between the analytical and the experimental results are less than 8%. These results can also be used in the future design of V-beam sensors as they can facilitate the making of an informed decision when it comes to determining the geometry that would lead to a desired response.

2.6. Matlab Scientific Toolbox for Strain-Stress Analysis

2.6.1. Introduction

Determination of the strain and stress states in machine parts is an essential condition in their reliability and design. Experimental methods in solid mechanics together with analytical and numerical concepts have a well-known importance. Development in the last decades of the computers has led in this field to numerous contributions in the direction of strain - stress analysis based on images processing. Most of so called optical methods of engineering analysis are today widely used due to the high speed computation, full-field information, enhanced calculus accuracy and friendly computer software. Among these, it should be reminded Moiré technique, ESPI (Electronic Speckle Pattern Interferometry), or grey correlation techniques, which provide full-field information about the in-plane or out-of-plane deformations. In most cases, to carry out the component design, a subsequent data processing is necessary to get strain or stress distribution. Full-field information reveals rapidly the hot spots and contributes to phenomena understanding.

To complete a complex strain-stress investigation using optical methods sophisticated equipment controlled by dedicated computer software is needed. Interaction of the researcher in the measuring process or data manipulation is restricted by system parameters. Development of commercial applications adapted to the research objectives is time consuming and very expensive. The difficulties to find a universal tool convince the researcher to create specific applications that can offer higher flexibility and are fully verifiable. Mathwork's MATLAB® is a software packet designed among other to image and data processing. Worldwide used in technical computing and data processing and having a high numbers of predefined numerical algorithms is the ideal instrument for software development by researchers and engineers.

In experimental mechanics, especially in optical methods, achievement of a MATLAB Scientific Toolbox to calculate full-field strain and stress distribution in components based on measured values of the deformation is a low cost solution, easy to use and control and having fully flexibility to different application or research. Developing of a Scientific Toolbox involves of course advanced MATLAB programming knowledge but the major difficulty is to define the calculation algorithms, to implement them according to the testing conditions or component characteristics and finally to interpret the results. All of these requirements presume experience in multidisciplinary fields such as mechanics of materials, experimental stress analysis, and image processing and software development [93, 94].

The intention was to develop using MATLAB software a scientific toolbox for strain-stress analysis having as input data the full-field deformations of the specimen surface obtained by experimental optical methods. Calculations algorithms were defined to fulfil automatically the following steps:

- Selection and read of the experimental data (full-field deformations) corresponding to different measuring systems and different file formats;
- Computation of full-field strains and stresses according to different theoretical algorithms;
- Interactive and intuitive visualisation of the results – 2D & 3D graphical plots;
- Easy data storage and reports generation;
- Capabilities for further development.

Based on presented ideas the author was supported by the European Commission with a Marie-Curie European Reintegration Grant, research grant financed within 6th Framework Program (FP6), Research Directorate General Human Resources and Mobility (contract no. MERG-CT-2004-510256), period 2004-2005 entitled *MATLAB Scientific Toolbox for Strain-Stress Analysis*. The results were disseminated by publication of the following articles in the proceedings of international conferences or Romanian journals:

1. **Dudescu, M.** (2003): Processing of the experimental data using MATLAB. Proceedings of the 2nd Youth Symposium on Experimental Solid Mechanics, Milano Maritima, Italy, 7-10 May 2003, pp. 105-107, ISBN 88-901080-0-2.
2. **Dudescu, M.**, (2004): Matlab Scientific Toolbox for Strain-Stress Analysis. Acta Technica Napocensis, nr. 47/2004, pag. 31-40, Editura U.T.Press Cluj-Napoca, ISSN 1224-9106.
3. **Dudescu, M.** Păstrav, I. (2004): *Full-field processing of experimental data using MATLAB*. Al X-lea Simpozion internațional de analiză experimentală a tensiunilor și încercarea materialelor, 22-23 Oct. 2004, Sibiu, România, pp. 4.13-4.16, ISBN 973-651-918-X.
4. **Dudescu, M.** (2006): *Post-processing of experimental data using Matlab*. International Workshop "Advanced Researches in Computational Mechanics and Virtual Engineering" 18-20 October 2006, Brașov, Romania, ISBN 973-635-823-2.
5. **Dudescu, M.**, (2006): *MATLAB Scientific Toolbox for Full-field Strain and Stress Computation*. Acta Universitatis Cibiniensis a Universității Lucian Blaga din Sibiu, vol.54, pag. 31-36, ISSN 1583-7149.

2.6.2. MATLAB Graphical User Interface

In Fig. 2.6.1 is presented a complex MATLAB Graphical User Interface (GUI) designed to compute different experimental data in order to get strains, stresses and their directions. The GUI is structured in two different frames ("Input data" and "Results") according to the calculation flow. The results are presented in the plot area. Pull-down menus (Fig. 2.5.2) that accompany the graphical interface facilitate the user to access some extra features such as file operations (*Open, Copy, Save, Print, Close*), graphics (*Profile, Point value*) and settings (*Filter parameters, Reset input data*) [29, 95].

The input data can be read directly from the measurement output files through an interactive menu, and three proprietary file types are automatically recognized: Ombré v. 2.1[27], having file extension "REL" or "DFO" (Laboratoire Mecanique de Solides, Poitiers, France), ISTR v.2.2[96], having file extension "TFD", (Dantec-Emtemeyer GmbH, Ulm, Germany) and ASCII format (extension "TXT"). After selection of input file containing in plane or out of plane experimentally measured object deformations and its dimensions respectively, the user can choose the corresponding problem solver: *1D strain, 2D plane stress, 2D plane strain, plates of constant thickness and torsion of bars using membrane analogy*. According to the selected analysis type the object deformation can be displayed in the plot area. Median and smooth filter having adjustable parameters can be applied to the deformation images (data) before the calculation if these are noise. If wrong parameters are chosen or extensive filtering is applied, the data values can be affected, an "Undo" command is available through pull-down menus. Material parameters necessary to calculate stresses (E-modulus, Poisson ratio and plate thickness in case of plate calculation) are necessary to fulfil the computation.

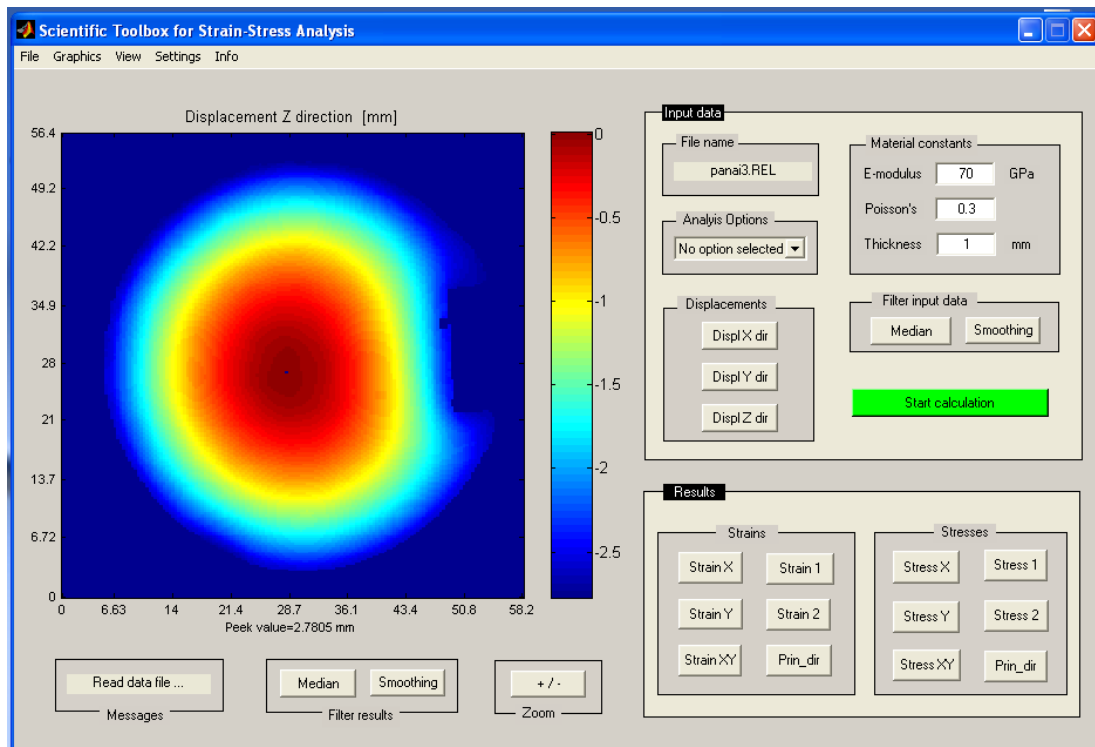


Fig.2.6.1. MATLAB Graphical User Interface of the Scientific Toolbox for Strain-Stress Analysis

Calculation is done in seconds and then the results visualisation module becomes active. The results in terms of strain and stresses are graphically presented as color coded images, color contour levels or 3D plots. Visualisation mode can be chose by user and “Zoom” and “Rotate” functions increase the interface capabilities. All data displayed in the plot area can be printed, saved or copied. Two types of image filters - median and smoothing - with adjustable parameters were also included to reduce noise quantity and to improve data quality. Further analyses are possible using profile and point value functions.

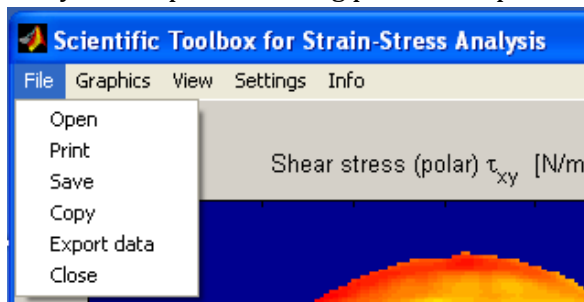


Fig. 2.6.2. File pull-down menu with the following items:

- *Open* – (see fig. 3)
- *Print* – standard print menu
- *Save* – save current figure
- *Copy* – copy current figure to Clipboard
- *Export data* – export current data as TXT files
- *Close* – close the GUI

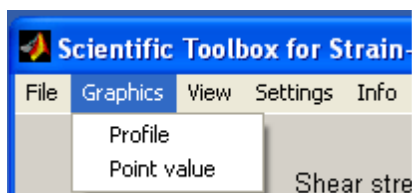


Fig. 2.6.3. Graphics menu

- *Profile* – draw a profile of the current data set along a user selected straight line.
- *Point value* – display single value and the point coordinates dynamically by mouse selection.

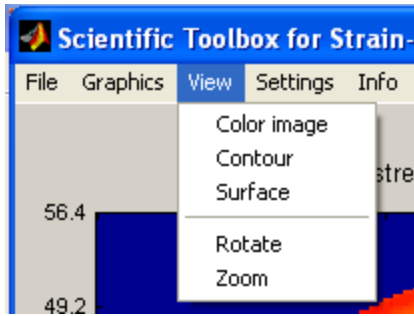


Fig. 2.6.4. View menu

- *Color Image* – display data (measured values or results) as color code images
- *Contour* - display data (measured values or results) as contour lines
- *Surface* - display data (measured values or results) as a 3D surface
- *Rotate* – valid only for surfaces representation of data, produce rotation by mouse of the 3D representation.
- *Zoom* – zoom function

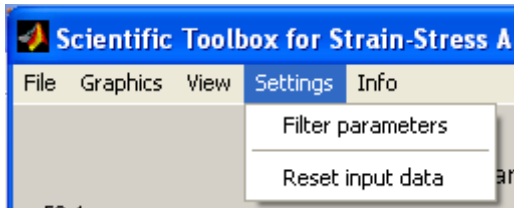


Fig. 2.6.5. Settings menu

- *Filter parameters* – settings for filtering areas
- *Reset input data* – undo command in order to get original unfiltered data

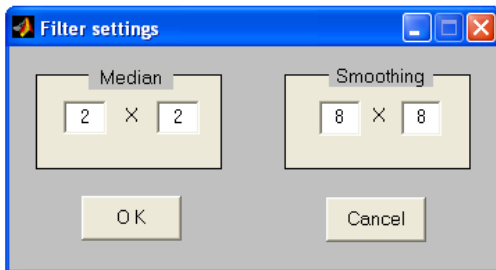


Fig.2.5.11. Filter settings menu

- *Median* filter
- *Smooth* filter

First filter is a median filter and the second one an adaptive filter, both being implemented in MATLAB Image Processing Toolbox.

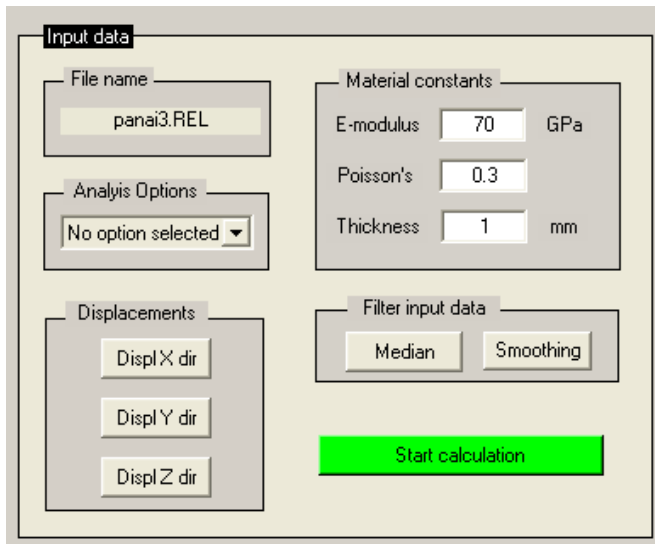


Fig. 2.6.7. Input data frame

- *File name* – show current loaded file
- *Analysis options* – selection of problem type
- *Displacements* – show the displacements values as color code images according to data type and selected problem
- *Material constants* – Input data fields for Young modulus, Poisson’s ratio and plate thickness
- *Filter input data* – median and smooth filter of data



Fig. 2.6.8. Other functions: Messages (display current operation and processing step), Filters (median and smooth filter applied for results only) and Zoom function.

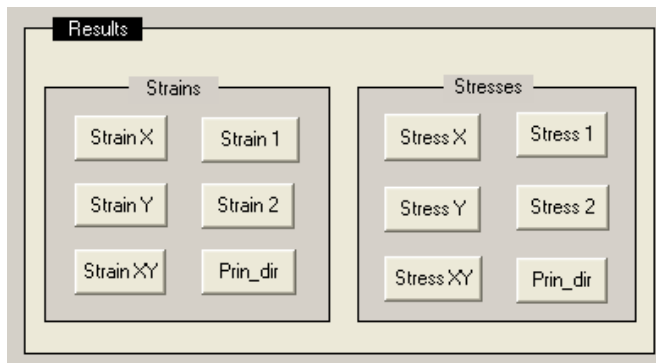


Fig. 2.6.9. Results

- Strains – normal and shear strains, principal strains and principal directions of strains
- Stresses – normal and shear stresses, principal stresses and direction of principal stresses

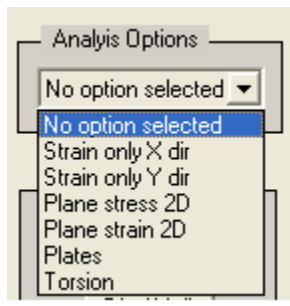


Fig.2.6.10. Analysis options:

- *No option selected* – default value
- *Strain only X direction* – calculate only 1D strain
- *Strain only Y direction* - calculate only 1D strain
- *Plane stress 2D* – plane stress model, both in plane displacements (x & Y direction) are needed for calculation
- *Plane stress 2D* – plane stress model, both in plane displacements (x & Y direction) are needed for calculation
- *Plates* – calculation based on plates theory, plates thickness and out-of-plane displacements are needed
- *Torsion* – shear stress calculation based on membrane analogy, only membrane shape are needed

Median filtering is a nonlinear operation often used in image processing to reduce "salt and pepper" noise. Median filtering is more effective than convolution when the goal is to simultaneously reduce noise and preserve edges. Each output pixel contains the median value in the m -by- n neighbourhood around the corresponding pixel in the input image. Median filter pads the image with zeros on the edges, so the median values for the points within $[m\ n]/2$ of the edges may appear distorted.

Smooth filter low-pass filters an intensity image that has been degraded by constant power additive noise. Smooth filter uses a pixel-wise adaptive Wiener method based on statistics estimated from a local neighbourhood of size m -by- n of each pixel. The additive noise (Gaussian white noise) power is assumed to be noise.

2.6.3. Toolbox modules and computation algorithms

Computation algorithm behind the developed MATLAB Scientific Toolbox for Strain-Stress Analysis is based on displacement data derivation along selected direction. The derivation is performed in every data point by finite differences method between successive elements of the measured data. As is known this method is an approximate derivative. The calculation error is very small if the number of calculation points is big enough. In case of optical methods usually the obtained image representing the displacements values are given by the CCD camera resolution, which means minimum of 512×512 pixels (points). At this number of points is not necessary to use other complicated numerical methods to get the derivative (such as interpolation, Taylor series, etc). Future Scientific Tolbox applications using generated data sets (synthetic data) will be analysed in order to prove the derivation algorithm reliability.

A simple example is presented in order to understand the derivation algorithm (Fig. 2.6.11). The data are obtained by Electronic Speckle Pattern Interferometry and are demo data of the ISTRA [96] software.

$$\epsilon_x = \frac{\partial u}{\partial x} = \frac{\text{diff}(u)}{\text{diff}(x)}$$

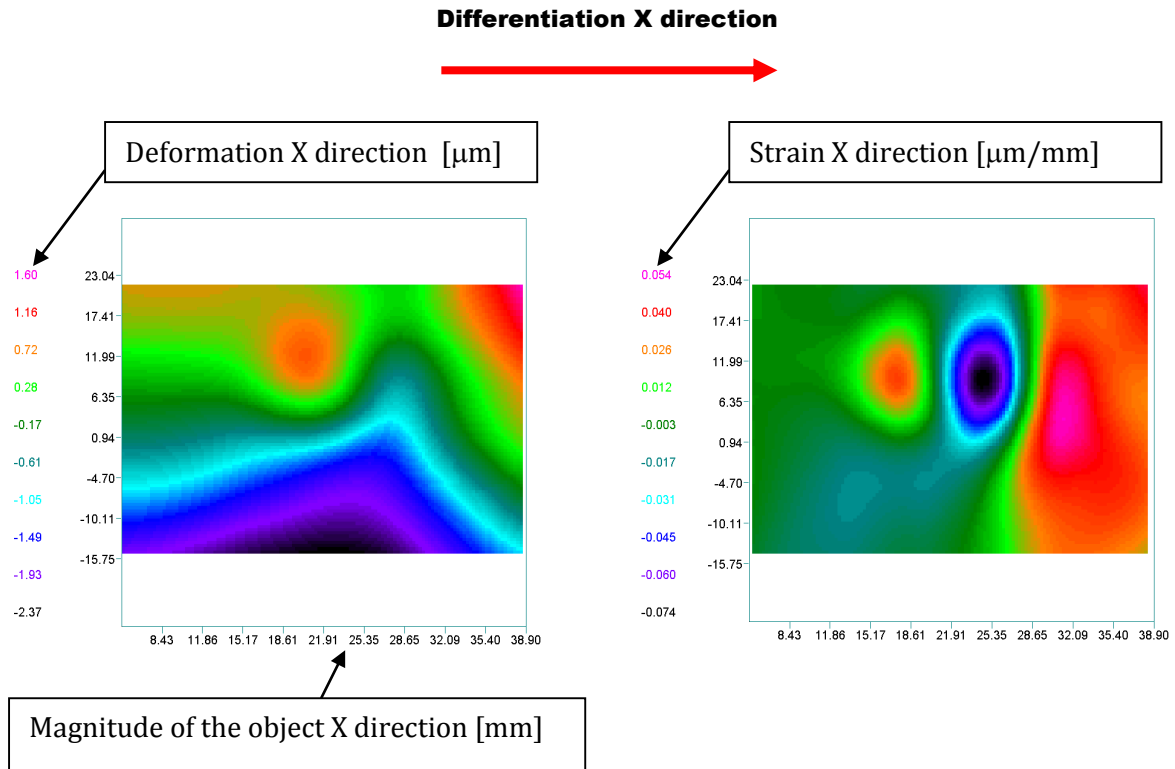


Fig. 2.6.11. Calculation example of strain in X direction based on experimental data

It has to be noticed that *strain calculation do not require information about object material or any theoretical models (plane strain or plane stress).*

To calculate all components of strains are necessary in-plane and out-of plane displacements and all three dimensions of the measuring object.

$$\epsilon_x = \frac{\partial u}{\partial x}, \quad \epsilon_y = \frac{\partial v}{\partial y}, \quad \epsilon_z = \frac{\partial w}{\partial z} \tag{2.6.1}$$

$$\gamma_{xy} = \frac{\partial u}{\partial y} + \frac{\partial v}{\partial x}, \quad \gamma_{yz} = \frac{\partial v}{\partial z} + \frac{\partial w}{\partial y}, \quad \gamma_{zx} = \frac{\partial w}{\partial z} + \frac{\partial u}{\partial z} \tag{2.6.2}$$

For used optical methods only 3 independent strain components can be calculated: normal strain in X direction ϵ_x , normal strain in Y direction ϵ_y and shear strain γ_{xy} .

Principal strain and its direction can be calculated with the formulas:

$$\epsilon_{1,2} = \frac{\epsilon_x + \epsilon_y}{2} \pm \sqrt{\left(\frac{\epsilon_x - \epsilon_y}{2}\right)^2 + \left(\frac{\gamma_{xy}}{2}\right)^2} \tag{2.6.3}$$

$$\tan 2\theta = \frac{2\epsilon_{xy}}{\epsilon_x - \epsilon_y} \tag{2.6.4}$$

According to the appropriate theoretical model can be computed stresses, principal stresses and its directions.

PLANE STRESS MODEL

Stresses in a thin plate or on the free surface of a structural element, such as the surfaces of thin-walled pressure vessels under external or internal pressure, the free surfaces of shafts in torsion and beams under transverse load, have one principal stress that is much smaller than the other two. By assuming that this small principal stress is zero, the three-dimensional stress state can be reduced to two dimensions, and the part is said experience **plane stress**.

Examples of plane stress: free surface of a structural element i.e. beams, shafts in torsion, thin plates, pressure vessels, etc.

Remarks:

- $\sigma_n = 0$ or $\sigma_{3(n)} \ll \sigma_1, \sigma_2$
- $\varepsilon_n = -\nu/E(\varepsilon_x + \varepsilon_y) \neq 0$
- Presence of a plane state of stresses implies a tri-dimensional state of deformations

Formulas for stresses become:

$$\sigma_x = \frac{E}{1-\nu^2}(\varepsilon_x - \nu\varepsilon_y), \sigma_y = \frac{E}{1-\nu^2}(\varepsilon_y - \nu\varepsilon_x), \tau_{xy} = G \cdot \gamma_{xy} \quad (2.6.5)$$

where $G = \frac{E}{2(1+\nu)}$.

Principal stresses and principal directions of stresses have significant importance in components design, giving the necessary state of stress in one point. It should be noticed that for isotropic materials the principal strains occur in the same directions as the principal stresses

Calculation formulas:

- Principal stresses

$$\sigma_{1,2} = \frac{\sigma_x + \sigma_y}{2} \pm \sqrt{\left(\frac{\sigma_x - \sigma_y}{2}\right)^2 + \tau_{xy}^2} \quad (2.6.6)$$

- Principal direction

$$\tan 2\theta = \frac{2\tau_{xy}}{\sigma_x - \sigma_y} \quad (2.6.7)$$

$$\theta_{p2} = \theta_{p1} + \frac{\pi}{2} \quad (2.6.8)$$

Calculation of principal directions implies 2 steps:

1. Computation of principal angles θ_p
2. Identification of the individual principal angles θ_{p1}, θ_{p2} .

PLANE STRAIN MODEL

A dam subjected to water loading, a tunnel under external pressure, a pipe under internal pressure, and a cylindrical roller bearing compressed by force in a diametric plane, have significant strain only in a plane; that is, the strain in one direction is much less than the strain in the two other orthogonal directions. If small enough, the smallest strain can be ignored and the part is said to experience **plane strain**.

In case of optical methods only the object surface are investigated, and the question is when it experiences plane strain state? To have such a state an out of plane stress (normal

stress) is required to maintain plane strain. This can occur only in special testing condition ($\varepsilon_n = 0$) or by crack propagation studies.

The formulas for stresses in this case are:

$$\sigma_x = \frac{E(1-\nu)}{(1-2\nu)(1+\nu)} \left(\varepsilon_x - \frac{\nu}{1-\nu} \varepsilon_y \right) \quad (2.6.9)$$

$$\sigma_y = \frac{E(1-\nu)}{(1-2\nu)(1+\nu)} \left(\varepsilon_y - \frac{\nu}{1-\nu} \varepsilon_x \right) \quad (2.6.10)$$

$$\tau_{xy} = G \cdot \gamma_{xy} \quad (2.6.11)$$

$$\sigma_{1,2} = \frac{\sigma_x + \sigma_y}{2} \pm \sqrt{\left(\frac{\sigma_x - \sigma_y}{2} \right)^2 + \tau_{xy}^2} \quad (2.6.12)$$

Plate model

If only out-of-plane deformation is available after optical measurement the problem of strain and stress calculation can be solved for one particular case. This is the case of plane plates having constant thickness.

Some work and calculation hypotheses have to be considered for the calculation:

- small deflections - the deflection is small comparatively with the thickness of the plate
- thin plates - the thickness and the span or diameter of the plate are related $t \leq l/10$
- Kirchhoff hypothesis - a normal and straight segment to the median plane do not bend
- In the median plane there are no deformations - neutral plane
- Each layer parallel with the median plane is in a plane stress state
- Stresses are calculated according to the plane stress model
- $\varepsilon_z = \frac{\partial w}{\partial z} = 0, \gamma_{xy} = \frac{\partial u}{\partial y} + \frac{\partial v}{\partial x} = 0, \gamma_{zx} = \frac{\partial w}{\partial z} + \frac{\partial u}{\partial x} = 0$

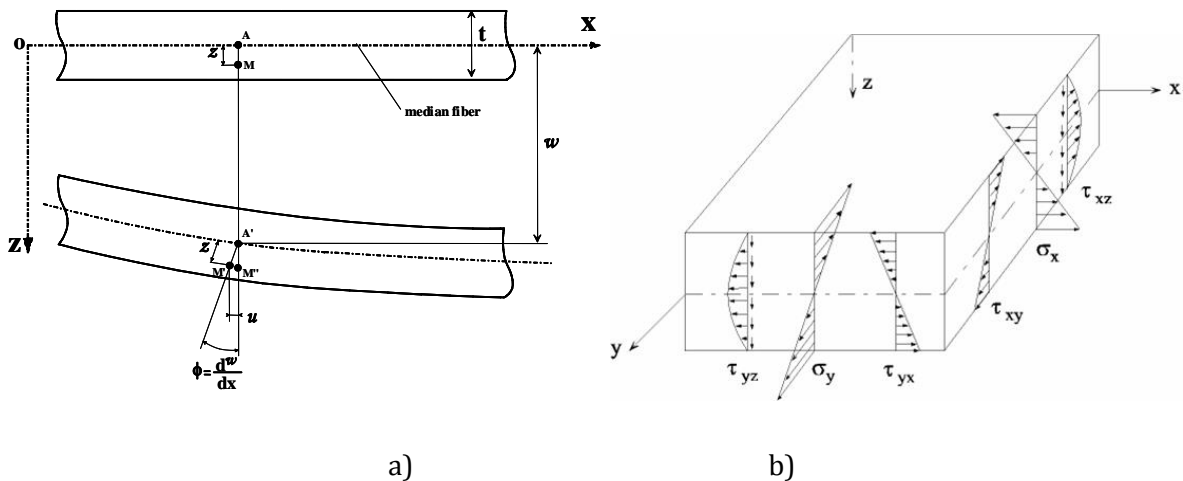


Fig. 2.6.12. Plates deformation (a) and stresses distribution (b)

Computation of strains is done based on the second derivative of the out-of-plane deformation of plate, considering known the plate constant thickness z .

$$\varepsilon_x = \frac{\partial u}{\partial x} = -z \frac{\partial^2 w}{\partial x^2}; \varepsilon_y = \frac{\partial v}{\partial x} = -z \frac{\partial^2 w}{\partial y^2}; \gamma_{xy} = \frac{\partial u}{\partial y} + \frac{\partial v}{\partial x} = -2z \frac{\partial^2 w}{\partial x \partial y} \quad (2.6.13)$$

$$\sigma_x = \frac{E}{1-\nu^2}(\varepsilon_x - \nu\varepsilon_y); \sigma_y = \frac{E}{1-\nu^2}(\varepsilon_y - \nu\varepsilon_x); \tau_{xy} = G \cdot \gamma_{xy} \quad (2.6.14)$$

It can be noticed that there are no restrictions imposed to the supporting system or distribution law of the load.

2.6.4. Applications in experimental mechanics

DETERMINATION OF STRESS CONCENTRATION IN A TENSILE SPECIMEN

For a rectangular bar subjected to tension, investigation of strain along tensile direction (axis of bar) can be realized by ESPI using dual illumination method[38]. The experimental set-up is presented in figure 2.6.13.



Fig. 2.6.13. ESPI measuring set-up for in-plane determination of a tensile specimen displacements

Phase map of the correlation fringes and measurement results (displacements in X direction) are presented in figures 2.6.14 and 2.6.15.

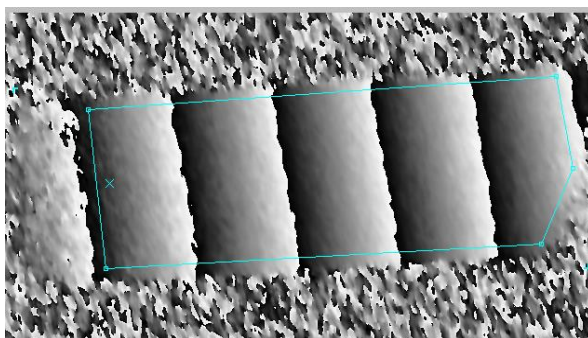


Fig. 2.5.14. Phase map of the correlation fringes and analysed area (line)

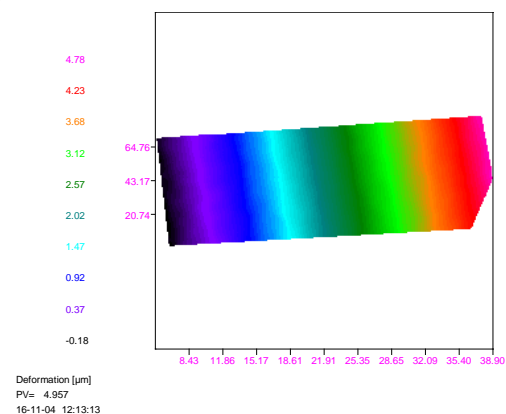


Fig. 2.5.15. In plane displacements of the bar

Using MATLAB Scientific Toolbox the value of normal strain along direction X can be computed (Fig. 2.6.16). It can be noticed the constant strain in case of simple tension specimen and the measurement data quality that was affected by noise (Fig. 2.6.17) [97].

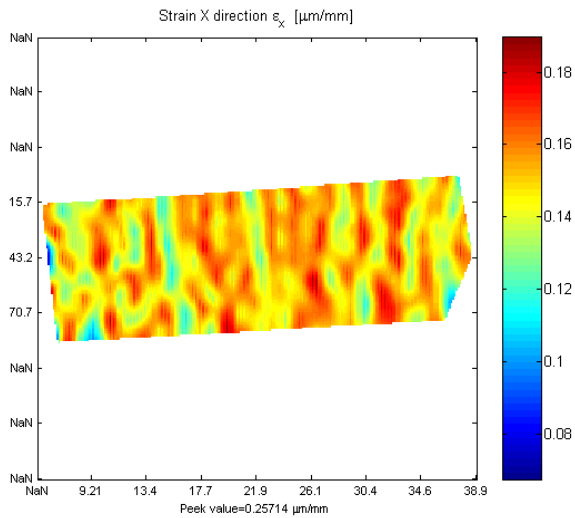


Fig.2.6.16. Strain distribution along X axis

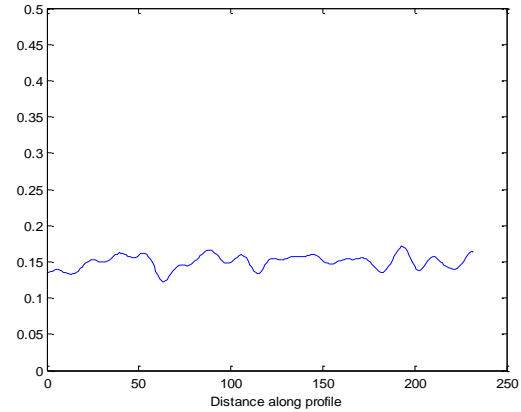


Fig.2.6.17. Profile along axis of bar reveals constant normal strain and noise level

In order to analyse simultaneously two in-plane directions (horizontal and vertical) a complex set-up is needed. The results are in this case in terms of normal and shear strains and stresses. The principal directions of strain and stress can be also computed. For example, a tensile specimen having two symmetrical notches (stress concentrators) was measured with the Ettemeyer 3D-ESPI sensor (Q300) and displacements values are presented in Fig. 2.6.18.

Using Scientific Toolbox for Strain-Stress Analysis quick calculation is possible, full-field distribution of normal and shear strains and stresses (Fig. 2.6.19 and 2.6.20a) obtained after calculation have revealed the strain-stress concentration at the notch tip. Very meaningful are in this case the directions of principal strains and stresses shown in figure 2.6.20b).

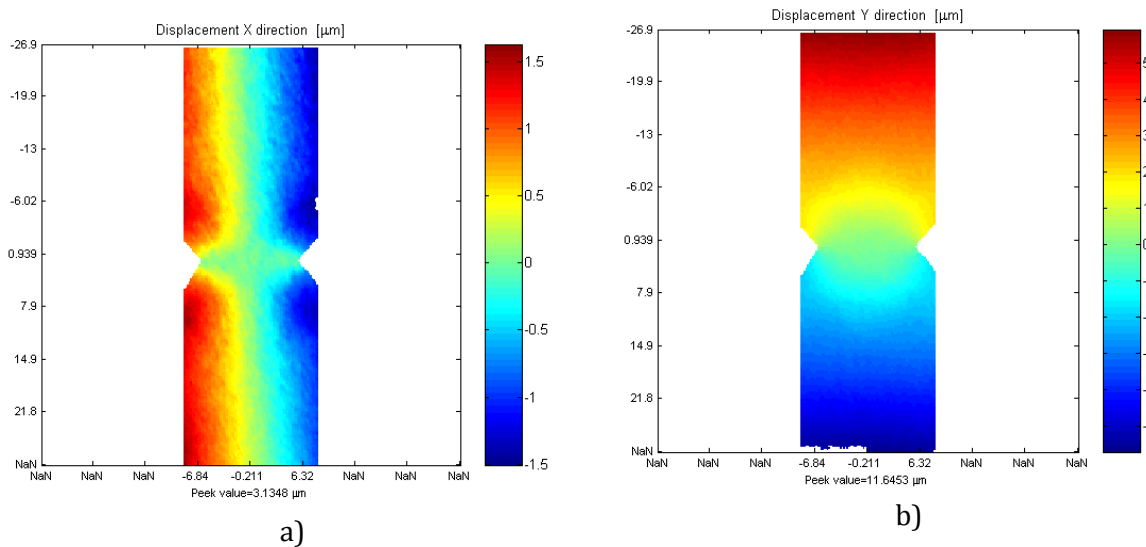


Fig. 2.6.18. In-plane measured displacements of a tensile specimen having a stress concentrator
a) horizontal and b) vertical direction

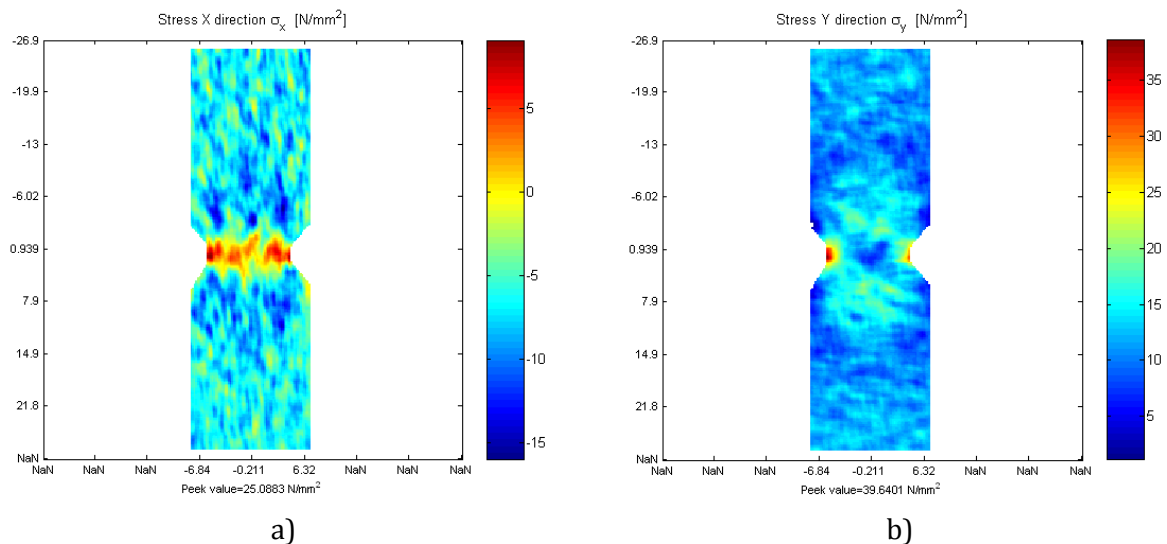


Fig. 2.6.19. Normal stress distribution [N/mm²] calculated using developed Scientific Toolbox for Strain-Stress Analysis a) σ_x and b) σ_y

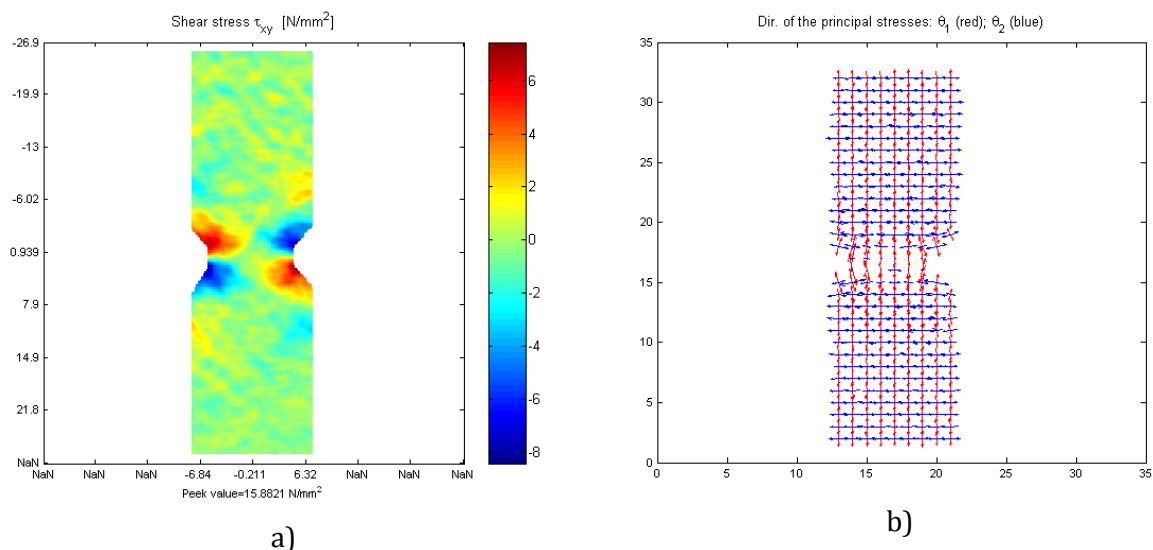


Fig. 2.6.20. a) Shear stress distribution τ_{xy} [N/mm²] and b) Direction of principal stresses calculated using developed Scientific Toolbox

DETERMINATION OF STRAIN-STRESS VALUES IN A CLAMPED PLATE LOADED BY A CENTRAL CONCENTRATED FORCE

Determination of strain and stresses in plates based on out-of-plane displacements was stated out in previous paragraph. The algorithm was implemented in the MATLAB Scientific Toolbox and its reliability was checked by generating synthetic data corresponding to a circular plate clamped and uniformly loads [98]. The results compared with those obtained from equilibrium equations of plates [99] revealed a very good convergence (Table 2.6.1) and validate the Scientific Toolbox.

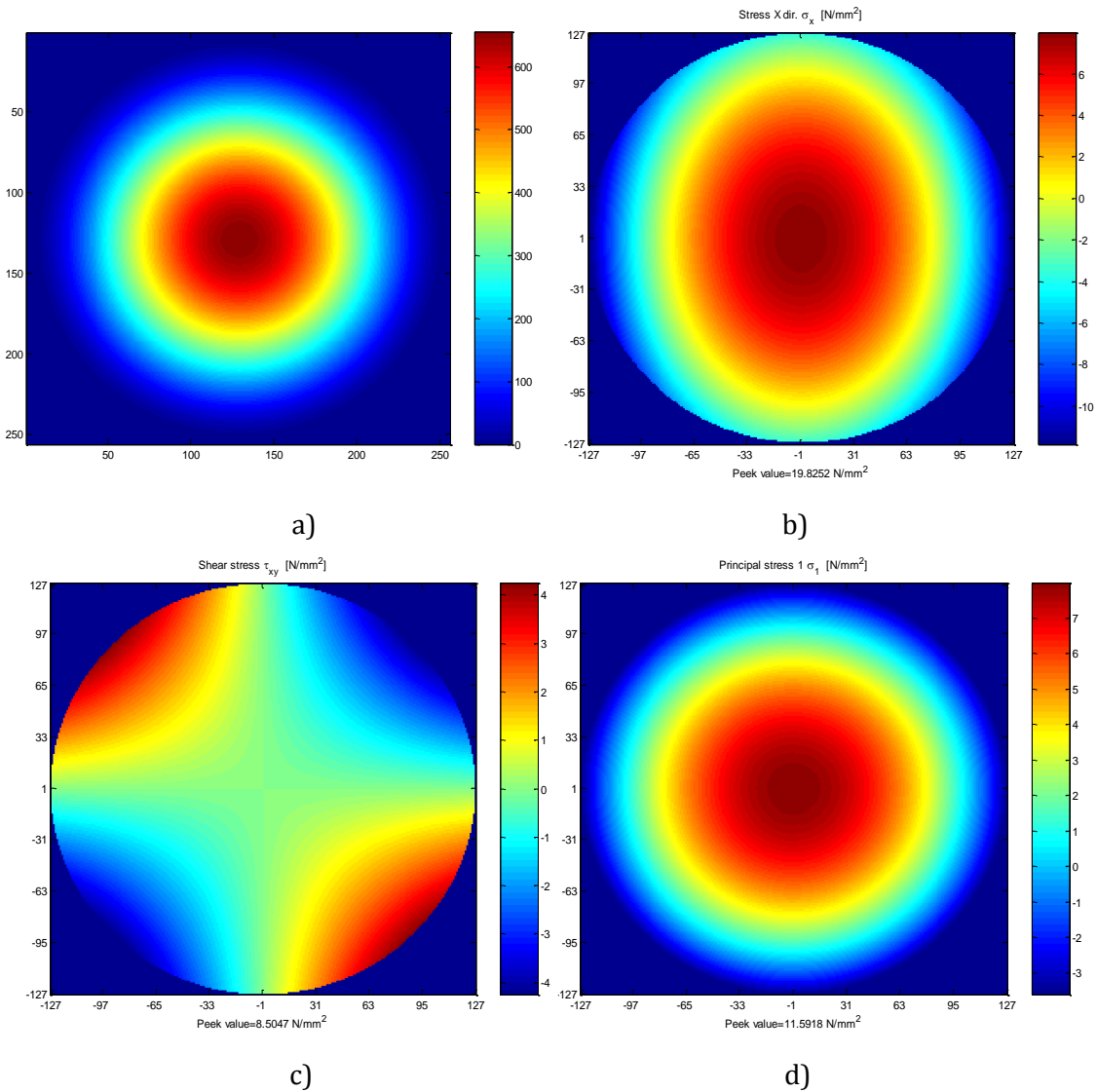
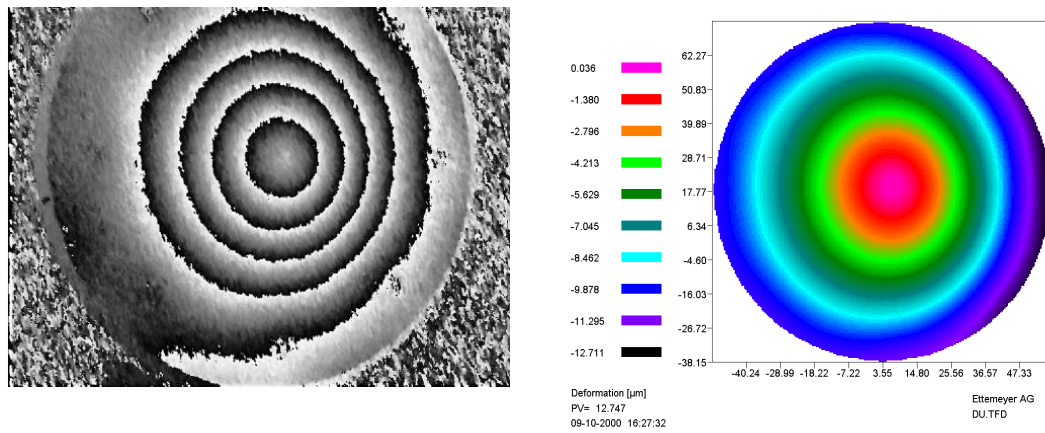


Fig. 2.6.21. Synthetic data for a clamped plate uniformly load.
 a) out of plane displacement [μm]; b) stress in horizontal direction (X),
 c) shear stress [N/mm^2]; d) principal stress σ_1 , [N/mm^2].

Table 2.6.1. Comparison of the results for a clamped plate

Stresses [N/mm^2]	$\sigma_\theta = \sigma_1$		$\sigma_r = \sigma_2$	
	Max	Min	Max	Min
Analytic	7,987	-3,595	7,987	-12,096
MATLAB	7,987	-3,605	7,986	-12,086
Deviation	0 %	0,2 %	0,01 %	0,08 %

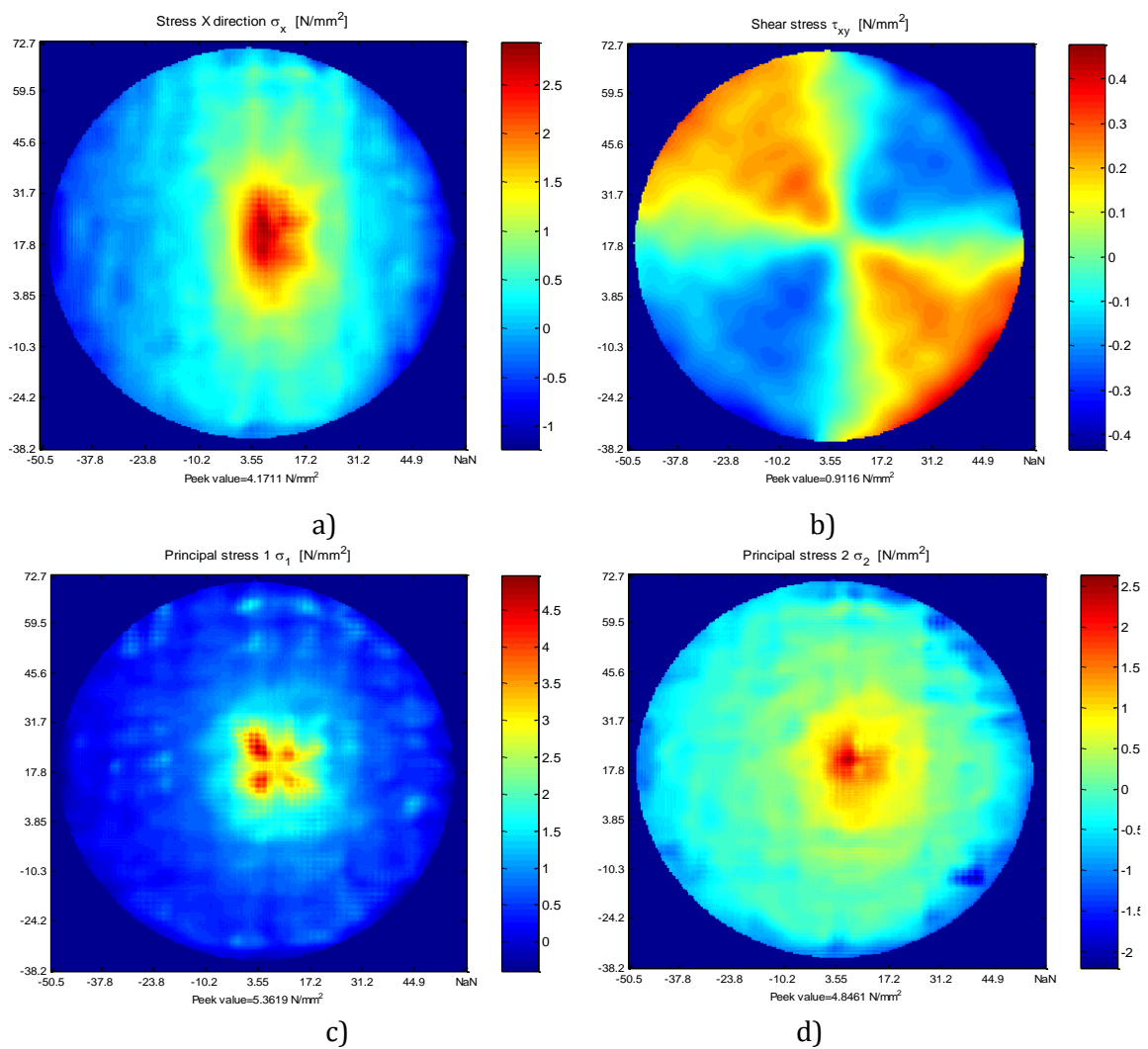
The input data for MATLAB Scientific Toolbox, as it was mention before, consists of out of plane measured displacements and plate’s dimensions. The user should introduce material constants (Young’s modulus, Poisson’s ratio) and the plate thickness in order to get the stresses. The results are presented graphically as color coded images and include normal and shear strains & stresses, principal strains, principal stresses and principal directions.



a)

b)

Fig.2.6.22. Experimental measurement (ESPI): a) phase map, b) out of plane displacement [μm].



a)

b)

c)

d)

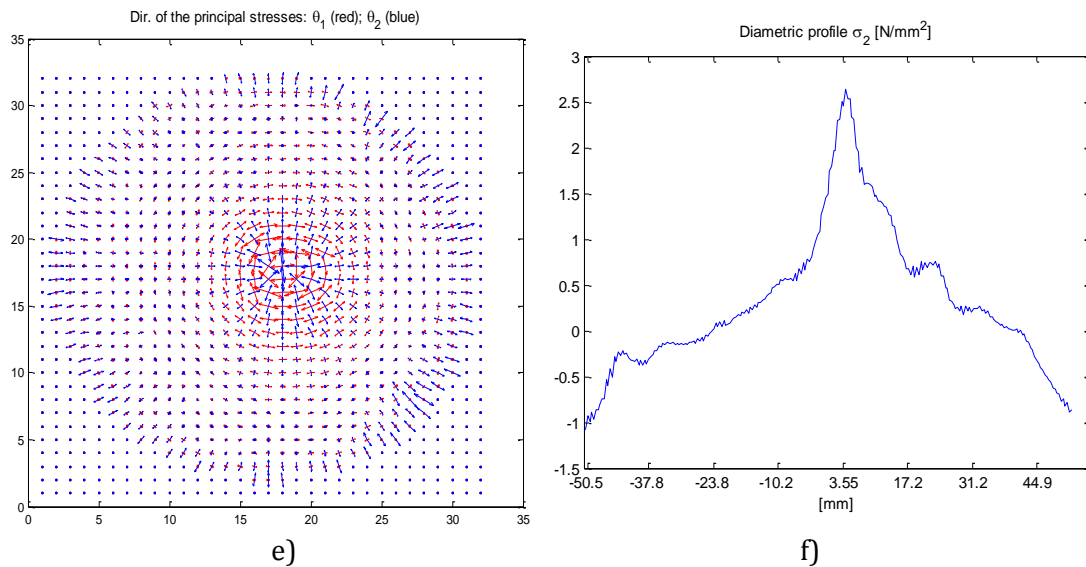


Fig.2.6.23. Experimental results [N/mm²]. a) Stress X direction; b) Shear stress; c), d) Principal stresses; e) Direction of the principal stresses; f) Horizontal profile – principal stress σ_2 (radial direction).

For above case the classical plates theory offer only an approximate solution in the vicinity of the force application point and calculation is done using the hypothesis of ideal border conditions, which are not achieved under experimental conditions.

The MATLAB Scientific Toolbox, based on the measured deformation, compute full-field strain and stress distribution. Figure 2.6.23 shows only few values - normal & shear stress and principal stresses – of the complete calculation. Examining principal directions (Fig.2.6.23e) we get the expected orientation – radial and circumferential. It is visible the high strain/stress gradient in the middle of the plate due to the punctual application of the force (Fig.2.6.23f).

DETERMINATION OF SHEAR STRESSES IN BARS SUBJECTED TO TORSION USING MEMBRANE ANALOGY AND SHADOW MOIRÉ

The Saint-Venant method to solve problem of torsion for bars having arbitrarily cross-section has been extensively described in the paragraph 2.3. Membrane analogy method to solve the problem of twisting of prismatic bars is limited by the difficulty to reconstruct the membrane's deformed surface, which represents the stress function in Saint-Venant's solution. The shadow Moiré method proved to be the most suitable to solve the problem [28]. The investigated membranes presented in paragraph 2.3.5 have circular shape without and with a key slot.

To check the validity of the developed MATLAB algorithm was generated, according to analytical equation, an ideal membrane shape corresponding to a bar having circular cross-section (Fig. 2.6.24a). These data have the important advantage to be noise free. The shear stress distribution (Fig.2.6.24b) compared with that calculated using classical formulas for a circular bar subjected to torsion revealed a very good convergence.

Based on shape information experimentally determined [28] and using developed MATLAB Scientific Toolbox, full-field shear stress distribution was computed for a bar subjected to torsion having circular cross-section without and with key slot.

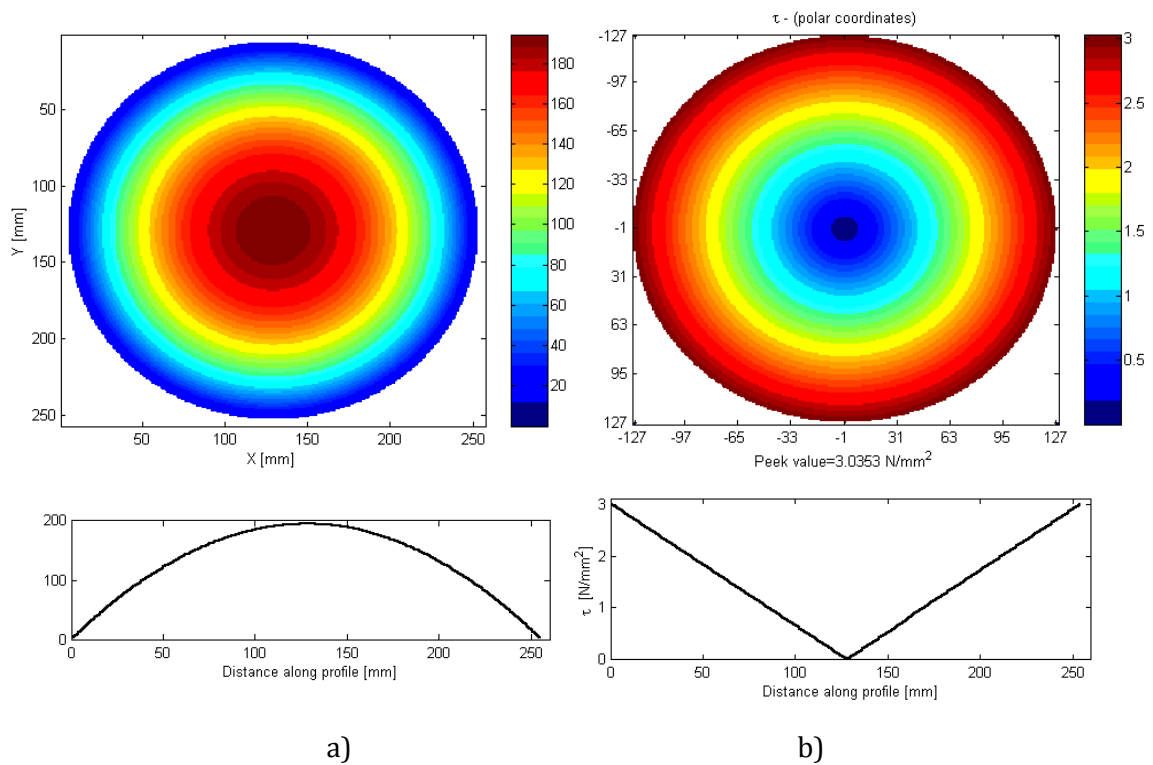


Fig.2.6.24. Synthetic data used to validate the MATLAB computation algorithm.

a) Ideal membrane shape and b) Shear stress distribution

In Fig. 2.6.25a is presented deformed membrane surface obtained by optical measurement method. The result is presented as color coded image accompanied by a color bar graded in millimetres similar to a FEM presentation. On the figure axes are given real dimensions (mm) of the measured membrane.

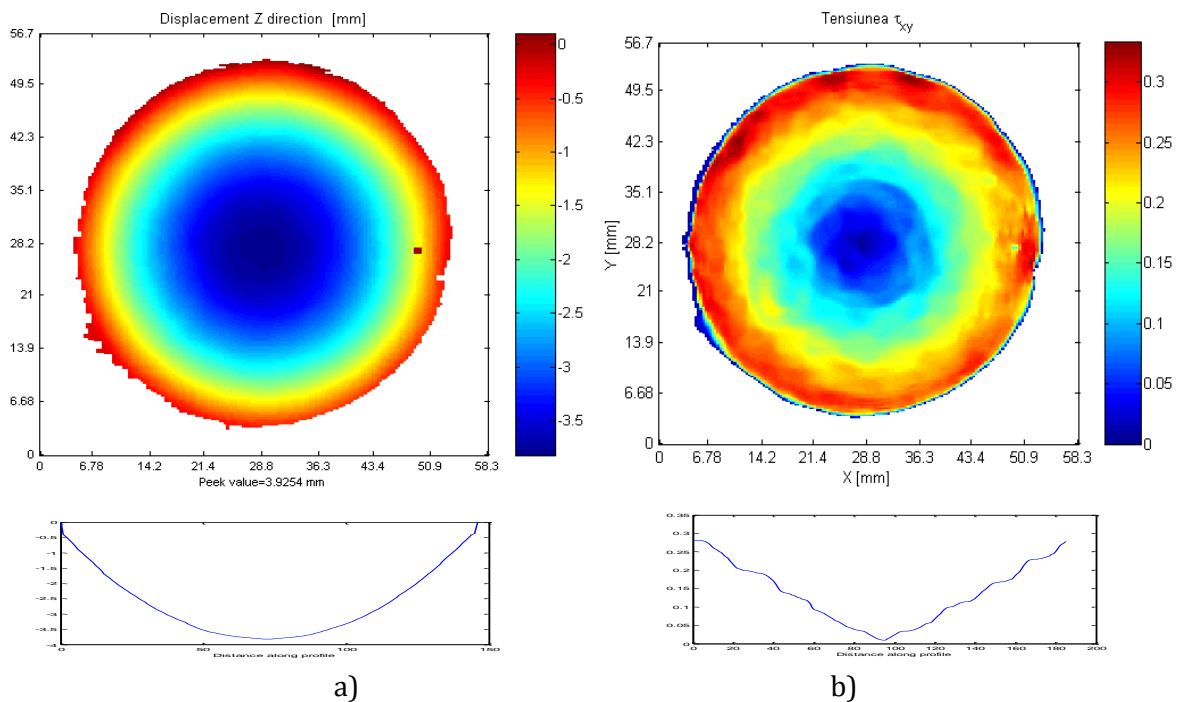


Fig.2.6.25. Computed results using MATLAB Scientific toolbox for a bar having circular cross section and subjected to torsion a) Measured membrane shape, b) Shear stress distribution

A diametric profile (not at scale) shows the experimental data quality. Full-field computation of shear stress based on membrane deformed shape is presented in Fig. 2.6.26b. The diametric profile shows a linear variation of shear stress that is in agreement with theory.

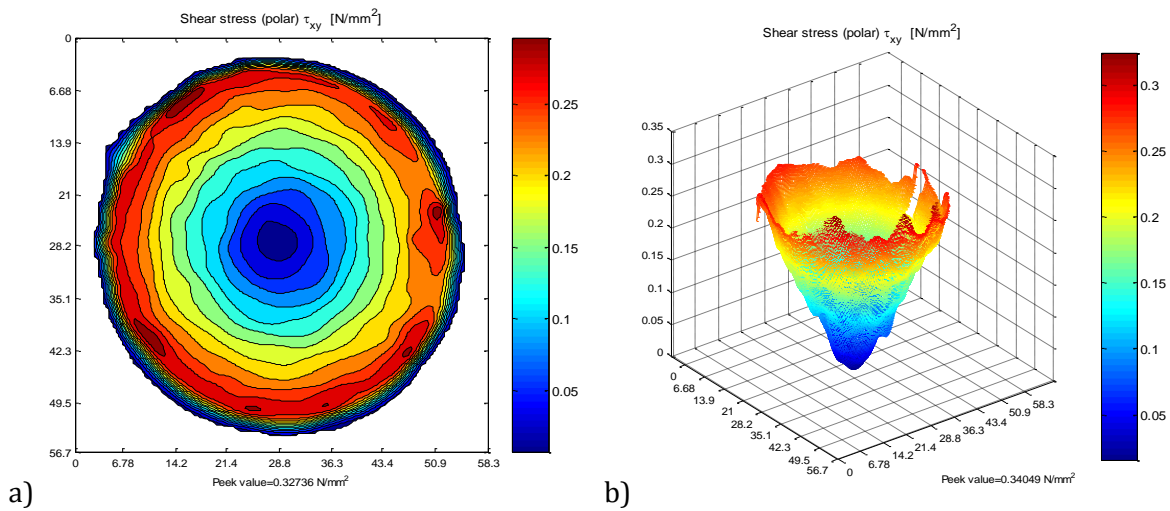


Fig.2.6.26. Possible results presentations for shear stress distribution
 a) color lines and b)3D surface

In Fig. 2.6.27a is presented deformed membrane surface in case of a bar having circular cross-section and a key slot. The example is very common in practice and a precise theoretical solution to describe the shear stress distribution doesn't exist. Full-field stress computation (Fig.2.6.27b) using MATLAB toolbox reveals the stress distribution in this case and gives the possibility to quickly identify the stress gradients. Profile and point value functions implemented in the toolbox graphical user interface permit further analysis of calculated data.

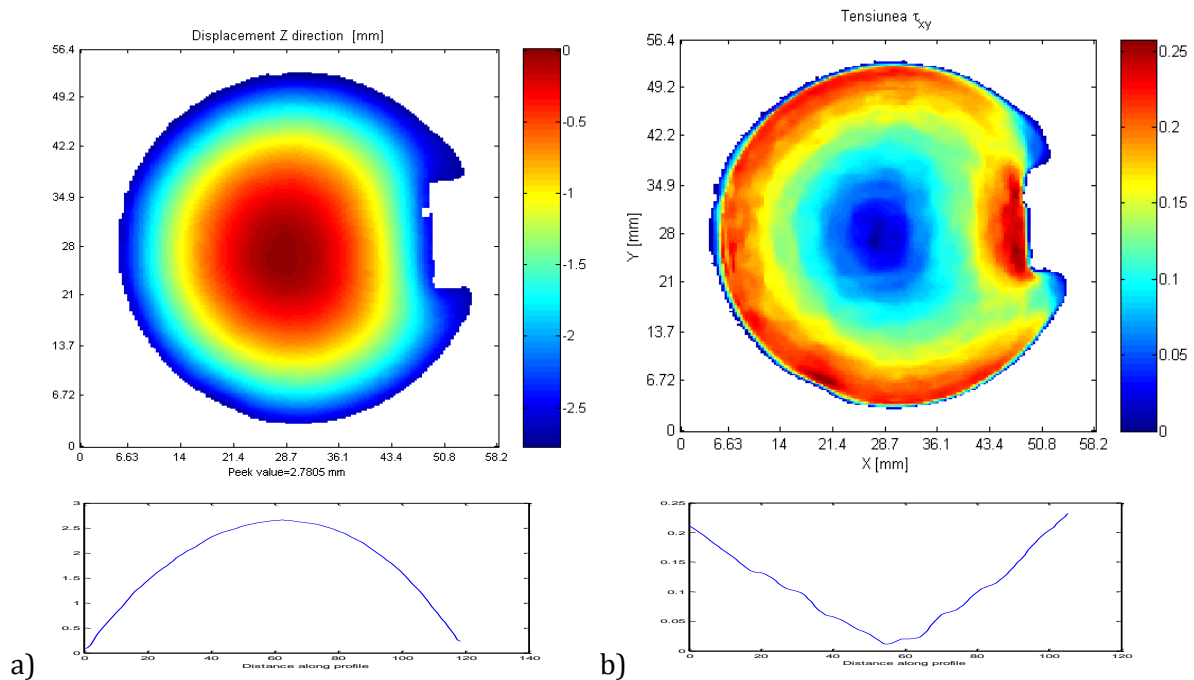


Fig.2.6.27. Computed results using MATLAB Scientific toolbox for a bar having circular cross section with a key slot and subjected to torsion.
 a) Measured membrane shape, b) Shear stress distribution

b-ii. DIDACTIC SKILLS AND PROFESSIONAL ACHIEVEMENTS

In the Technical University of Cluj-Napoca, Faculty of Mechanical Engineering, Department of Mechanical Engineering I have taught the courses, seminars and laboratories of Strength of Materials and Finite Element Method. At the moment I am charged to teach Strength of Materials course at specializations Robotics and Industrial Economics Faculty of Mechanical Engineering and also the courses of Numerical Methods in mechanical Engineering at Thermal Equipment Systems specialization (Bachelor - Alba Iulia) and Biosystems Engineering for Agriculture and Food Industry (master). In 2005-2006, as a postdoctoral researcher, I led the laboratory works on the theme of electronic speckle pattern interferometry (ESPI) at the Department of Experimental Mechanics, Technical University of Chemnitz, Germany.

I have been guiding for a several years the diploma works (bachelor) at Industrial Economics Engineering specialization. I constantly participate as a tutor to the student scientific activities of the Faculty of Mechanical Engineering and other professional competitions in the field of strength of materials (C.C. Teodorescu student contest). Under a partnership with Ei.CESI (École d'Ingénieurs) France I guided the summer practice (internship training abroad) of French students from this university.

I have been actively involved in adapting and updating the teaching activities in accordance with current requirements and international models, trying to permanently combine the classical teaching methods with modern techniques. I had contributed to the introduction in the laboratory works and seminars of Strength of Materials of computer-based calculation program MDSolids, a widely used software by US universities and awarded as the best educational software for Mechanics of Materials. The proposed lab works and seminars have a strong practical components, being the result of observations and experience with different generations of students.

I have had a major contribution to Optical Methods, Material Testing and Finite Element Laboratories, both in terms of acquisition and maintenance of equipment and also in solving numerous test and studies. The labs are used for teaching and research by teachers and PhD students. I have tried to offer, especially to PhD students and young researchers, all the necessary information on how to work with the equipment, to use their capabilities and to support various tests and measurements. The fruitful collaborations with different PhD students has been materialized in numerous scientific publications.

Recognition of scientific and professional achievements has been materialized in the last 5 years in invitations for participating as official referent at twelve doctoral theses, both in technical and medical (dentistry) field at different universities (Politehnica University of Timisoara, Politehnica University of Bucharest, Technical University of Cluj-Napoca, University of Medicine and Pharmacy "Iuliu Hatieganu" Cluj-Napoca, University of Medicine and Pharmacy of Targu-Mures). Also I have been also member of the Guidance Doctoral Committee for numerous PhD students from TU, having through this type of activity the possibility to acquire the necessary skills to be able to coordinate my own PhD students.

At institutional level I have been involved as short term expert in the project "Increasing attractiveness and performance of training programmes for postdoctoral researchers and PhD in engineering sciences - ATTRACTING" supported by European Social Fund (POSDRU). In this project I have been co-organizer of the thematic workshop entitled "Modern Methods of Numerical and Experimental Analysis of Structures".

My involvement in the teaching and learning environment development is carried on beside already listed issues but also by participating in numerous committees in the interest of education. I was a member of commissions for admission to bachelor's and master, responsible for quality in the former Chair of Strength of Materials, responsible (2010) for organizing student scientific session of the Faculty of Mechanical Engineering, responsible for organizing various didactic activities (visits to labs team presentations at schools, etc.). I am a member of the Board of the Faculty of Mechanical Engineering (2008) and vice-dean of the Faculty of Mechanical Engineering (2012) with tasks related to the master, research and connections with industrial environment. In the period of 2011 and 2012 I have been member of Commission "Mechanical Engineering, Mechatronics and Robotics at CNATDCU (The National Council for Attestation of University Titles, Diplomas and Certificates), in charge with evaluation of numerous doctoral thesis.

b-iii. FUTURE SCIENTIFIC, PROFESSIONAL AND ACADEMIC DEVELOPMENT PLAN

CAREER DEVELOPMENT PROPOSALS IN TERMS OF SCIENTIFIC RESEARCH

Scientific research is an academic activity which requires highly demand in well ranked universities. The tradition of the Strength of Materials group of disciplines, through its qualified professors that work here has excelled at national level in the development and implementation of various experimental methods in measuring of strain and stress, particularly in the use of optical methods. The available and valuable equipment that currently exists makes this research area to remain challenging and with perspectives. The traditional methods of optical techniques (photoelasticity and geometrical moiré) have encountered a stagnation, most applications being solved by digital image correlation method. In the field of experimental methods there are two main research directions, on the one hand the development/improvement of new techniques/equipment and on the other hand to develop more applications required by the industrial environment. These two developments should be complementary and define the key to publish in top research journals or to access research projects. From this point of view I will continue the research in developing new methods or implementing of existing ones within the laboratory but especially in finding new applications and domains. The field of Microsystems (MEMS) is an area that develops permanently, with high potential and I want to continue the existing collaboration and projects. Topics that I want to investigate in this area are related to the application of the experimental methods for determining displacements of optical micro-mechanical systems, temperature effect on mechanical fatigue and fracture mechanics for these elements.

Another research area will be the applications of experimental techniques and computer simulations in dental medicine. Existing collaboration and already performed studies, all materialized in ISI papers and proceedings, have revealed the increase potential of collaboration and the importance of multidisciplinary that exists between the mechanical engineers and dentists.

Another area of interest with good perspectives is the mechanical characterization of materials. The existence of a high-performance equipment (testing machines, strain-gauge technique and full-field optical methods) offers the possibility of investigating new materials with interesting mechanical properties used in medical, mechanical, and automotive industries. Proposed collaborations so far within the framework of different projects and results already accepted for publication in peer-reviewed journals is constitutes the premise of valid research directions. Extension of the classical tensile or bending tests to dynamical studies as fatigue tests (High Cycle Fatigue and Low Cycle Fatigue) is one of the short-term priorities in terms of research and employment of existing equipment.

Increasing demand in the last period from companies to conduct various mechanical tests and numerical simulations shows the necessity of Mechanical Tests Laboratory certification in order to be able to attract funds from private sources.

Attraction of funds through participation in research projects as project manager or member of existing research groups at UTC-N constitutes a very important aim in the development of academic careers. The existence of sources of funding and a certain topics need to be solved these are essential conditions for participation in the conferences and paper publication. A possibility, in the medium term after habilitation, would be application for a

research project financed by Alexander von Humboldt Foundation for establishing new contacts and areas of scientific interest between former fellows and German universities.

PROPOSALS FOR ACADEMIC CAREER DEVELOPMENT

In the context of “Strength of Materials” discipline positioning in the engineering curricula the major objectives of developing a didactical career is related to ensuring the continuity of the activities of publishing teaching materials for the students, the introduction of optional courses, participation in multidisciplinary master programmes, participation in international programmes for the exchange of students, participation in projects with educational purpose and the last but not least attracting and mentoring of young people able and willing to pursue an university career in the field of mechanics of materials.

Textbooks publishing for students will be one of my future concerns designed to contribute to the understanding and increasing the attractiveness of the discipline. I am considering editing, with my colleagues, a laboratory works in strength of materials covering the analytical as well as experimental works. I will also complete English version of the Strength of Materials course, which already exists as a manuscript.

Another priorities for teaching are the republishing and improvement of Finite Element Method laboratory works and course support. FE is the discipline of the future, required by the economic environment, for that reason I consider necessary to contribute with a manual including theory and applications with ANSYS Workbench.

All these upcoming academic purpose publications will be made to certain standards imposed by similar international publications, industrial developments and trends of the future. The presented topics should be correlated with the other disciplines from engineering curricula so that the acquired knowledge can be quickly applied, ensuring a certain character of interdisciplinarity.

I will continue to participate with students to the student's scientific contests organized by the Faculty of Mechanical Engineering and the professional contest of strength of materials "C.C. Teodorescu". Held for more than 30 years with the support of Strength of Materials groups this professional competition is an important element in the academic development of students and teachers through the exchange of ideas and information. I will get more involved more in the Community programmes related to lifelong learning, the exchange of students and staff (LEONARDO, ERASMUS, and GRUNTVIG) as well as in other educational projects financed by the Structural Funds.

b-iv. REFERENCES

1. Kobayashi, A., *Handbook on experimental mechanics*. Englewood Cliffs, NJ, Prentice-Hall, Inc., 1987.
2. Sharpe, W., *Springer Handbook of Experimental Solid Mechanics*. 2008, New-York: Springer Science+Business Media.
3. Gdoutos, E., *Nurturing today's experimentalist*, in *Experimentally Speaking*. 2013, Society for Experimental Mechanics, Inc. p. 1-2.
4. Cloud, G., *Optical methods of engineering analysis*. 1998: Cambridge University Press.
5. Cloud, G., *Optical methods in experimental mechanics*. *Experimental Techniques*, 2010. **34**(6): p. 11-14.
6. Hervé, L. and B. Wattrisse, *Editorial of the Special Issue on Photo-Mechanics*. *Strain*, 2014. **50**: p. 369.
7. Rastogi, P.K., *Photomechanics*. 2000: Springer.
8. Grediac M., H., F., *Full-Field Measurements and Identification in Solid Mechanics*. 2012: Wiley-ISTE.
9. Patterson, E.A., *Digital photoelasticity: principles, practice and potential*. *Strain*, 2002. **38**(1): p. 27-39.
10. Ramesh, K., *Digital photoelasticity*. 2000, IOP Publishing.
11. Dudescu, M., *Calculul de rezistență al tuburilor ondulate*. 2005, Cluj-Napoca: U.T.Pres.
12. Theocaris, P., Atanasiu, C., Iliescu, N., Pastrav, I., ș.a. , *Analiza experimentală a tensiunilor*. Vol. 1. 1976.
13. Păstrav, I. and M. Dudescu. *Metode optice de analiză a tensiunilor utilizate în laboratoarele UTC-N*. in *A Treia Conferință Națională a Academiei de Științe Tehnice din România*. 2008. Cluj-Napoca, 12-13 Noiembrie 2008, pag. 75 -83.
14. Axelrad, E.L., *Theory of Flexible Shell*. 1984: Springer-Verlag.
15. EJMA, *Standard of the Expansion Joint Manufacturer Association*. 1998: New York.
16. Dudescu, M. *Experimental Stress Analysis in Bellows Subjected to Axial Loads*. in *Proceedings of the 3rd Youth Symposium on Experimental Solid Mechanics*. 2004. Poreta Terme, Italy, 12-15 May, 2004.
17. Dudescu, M., Hărdău, M. *Influence of the model weight in case of photoelastic analysis of bellows subjected to axial loading*. in *Proceedings of the 21th Danubia-Adria Symposium on Experimental Methods in Solid Mechanics*. 2004. Pula, Croatia.
18. Sciammarella, C.A., Sciammarella, F.M., *Experimental Mechanics of Solids*. 2012, Chichester, UK: John Wiley & Sons, Ltd.
19. Sciammarella, C.A., *The Moiré method—a review*. *Experimental Mechanics*, 1982. **22**(11): p. 418-433.
20. Păstrav, I., Dudescu, M.C., *Lucrări de laborator de metode optice de analiză a tensiunilor*. 2009 Editura U.T.Pres., Cluj-Napoca.
21. Mauvoisin G, B.F., Lagarde A. *Shadow moiré by phase shifting method, application to 3D shape reconstruction*. . in *Conference on advanced technology in experimental mechanics*. 1993.
22. Mauvoisin, G., F. Brémand, and A. Lagarde, *Shadow moiré by phase shifting method, application to 3D shape reconstruction*., in *Conference on advanced technology in experimental mechanics*. 1993.

23. Brémand, F., *A phase unwrapping technique for object relief determination*. Opt Laser Eng, 1992(21): p. 49-60.
24. Timoshenko, S. and S. Woinowski-Krieger, *Theory of plates and shells*. 1959: McGraw-Hill.
25. Dudescu, M. *Application of shadow moiré method by phase shifting to membranes deformation measurement*. in *Proceedings of the 4th Youth Symposium on Experimental Solid Mechanics*. 2005. Costracaro Terme, Italy.
26. Dudescu, M., Şomotecan, M. *Application of shadow moiré method to determine the membrane characteristic*. in *Proceedings of the 24th Danubia-Adria Symposium on Developments in Experimental Mechanics*. 2007. Sibiu, Romania.
27. Dupré, J.C., V. Valle, and F. Brémand. *Logiciel Ombre V 2.1*. 2001.
28. Păstrav, I., C. Badea, and M. Dudescu. *Study by shadow-Moiré of the prismatic bars subjected to torsion*. in *Proceedings of the 18th Danubia-Adria Symposium on Experimental Methods in Solid Mechanics*. 2001. Steyr, Austria.
29. Dudescu, M. *Processing of the experimental data using MATLAB*. in *2nd Youth Symposium on Experimental Solid Mechanics*. 2004. Milano Maritima, Italy.
30. Jacquot, P., *Speckle Interferometry: A Review of the Principal Methods in Use for Experimental Mechanics Applications*. Strain, 2008. **44**: p. 57-69.
31. Rastogi, P.K., *Digital speckle pattern interferometry and related techniques*. Digital Speckle Pattern Interferometry and Related Techniques, by PK Rastogi (Editor), pp. 384. ISBN 0-471-49052-0. Wiley-VCH, December 2000., 2000. **1**.
32. Steinchen, W. and L. Yang, *Digital Shearography. Theory and Application of Digital Speckle Pattern Shearing Interferometry*. 2003, Bellingham, Washington USA: SPIE Press.
33. Goodman, J.W., *Speckle Phenomena in Optics: Theory and Applications*. 2007, Roberts and Company, Greenwood Village, CO USA.
34. Dudescu, M., et al., *Characterisation of Thermal Expansion Coefficient of Anisotropic Materials by ESPI*. Strain, 2006. **42**(3): p. 197-206.
35. Jones, R. and C. Wykes, *Holographic and Speckle Interferometry*. 1989, Cambridge, England: Cambridge University Press.
36. Dudescu, M.C., *Introducere în interferometria electronică granulară*. 2010, Cluj-Napoca: Editura Risoprint.
37. Eberhardsteiner, J., *Mechanisches Verhalten von Fichtenholz - Experimentelle Bestimmung der biaxialen Festigkeitseigenschaften*. 2002, Wien: Springer.
38. Dudescu, M., *Introducere în interferometria electronică granulară*. 2011, Cluj-Napoca: Risoprint.
39. Siebert, T., Ettemeyer, A., Dudescu, M. *Integration of deformation and contour measurement with 3D-ESPI*. in *Proceedings of the 19th Danubia-Adria Symposium on Experimental Methods in Solid Mechanics*. 2002. Polanica Zdrój, Poland.
40. Zou, Y., G. Pedrini, and H. Tiziani, *Contouring by Electronic Speckle Pattern Interferometry Employing Divergent Dual Beam Illumination*. Journal of Modern Optics, 1994. **41**(8): p. 1637-1652.
41. Yang, L., Ettemeyer, A., *Strain measurement by three-dimensional electronic speckle pattern interferometry: potentials, limitations, and applications*. Optical Engineering, 2003. **42**(5).

42. Naumann, J., Stockmann, M., Nebel, S., Dulescu, M. *Measurement of the thermal expansion coefficient of carbon fibre composites by ESPI*. in *24th Danubia-Adria Symposium on Developments in Experimental Mechanics*. 2007. Sibiu, Romania.
43. Höfling, R. and P. Aswelt, *Interferometric studies on thermal expansion behaviour of carbon fibre-reinforced composites*. *Measurement*, 1993. **12**: p. 85-93.
44. Gopalakrishna, K.B., *NDT Solution: Electronic Speckle Pattern Interferometry Applied to the Characterization of Materials at Elevated Temperatures*. *Material Evaluation*, 1998. **56**(36-42).
45. Dulescu, C., et al., *Investigation of Non linear Springback for High Strength Steel Sheets by ESPI*. *STRAIN*, 2011. **47**(Issue Suppl.2): p. 8-18.
46. Wong, T.E. and G.C. Johnson, *On the effects of elastic nonlinearity in metals*. . *Transactions of the ASME* 1988. **110**: p. 332-337.
47. Hart, E.W., *A micromechanical basis for constitutive equations with internal state variables*. *J. Engineering Materials and Technology* 1984. **106**: p. 322-325.
48. Ghosh, A.K., *A physically-based constitutive model for metal deformation*. . *Acta Metallurgica* 1980. **28**: p. 1443 - 1465.
49. Yamaguchi, K., H. Adachi, and N. Takakura, *Effects of plastic strain path on Young's modulus of sheet metals*. *Metals and Materials*, 1998. **4**: p. 420-425.
50. Yoshida, F., T. Uemori, and K. Fujiwara, *Elastic-plastic behavior of steel sheets under in-plane cyclic tension-compression at large strain*. *Int. J. Plasticity*, 2002. **18**: p. 633-659.
51. Cleveland, R.M. and A.K. Ghosh, *Inelastic effects on springback in metals*. *Int. J. Plasticity*, 2002. **18**: p. 769-785.
52. Mollica, F., K.R. Rajagopal, and A.R. Srinivasa, *The inelastic behavior of metals subjected to loading reversal*, . *Int. J. Plasticity*, 2001. **17**: p. 1119-1146.
53. Benzerga, A.A., et al., *The stored energy of cold work: Predictions from discrete dislocation plasticity*, . *Acta Materialia*, 2005. **53**: p. 4765-4779.
54. Dulescu, M.C., Stockmann, M., Naumann, J. *Optical measurement of the strain-stress response during unloading of metal sheets undergoing large plastic deformations*. in *11th Youth Symposium on Experimental Solid Mechanics*. 2012. Brasov, Romania.
55. Krasovskyy, A., *Verbesserte Vorhersage der Rückfederung bei der Blechumformung durch weiterentwickelte Werkstoffmodelle*. 2005, Dissertation, Universität Karlsruhe.
56. Hild, F. and S. Roux, *Digital image correlation: from displacement measurement to identification of elastic properties—a review*. *Strain*, 2006. **42**(2): p. 69-80.
57. Pan, B., et al., *Two-dimensional digital image correlation for in-plane displacement and strain measurement: a review*. *Measurement science and technology*, 2009. **20**(6): p. 062001.
58. Pan, B., *Recent progress in digital image correlation*. *Experimental Mechanics*, 2011. **51**(7): p. 1223-1235.
59. Siebert, T., et al., *High-speed digital image correlation: error estimations and applications*. *Optical Engineering*, 2007. **46**(5): p. 051004-051004-7.
60. Siebert, T. and M. Crompton, *Application of High Speed Digital Image Correlation for Vibration Mode Shape Analysis*, in *Application of Imaging Techniques to Mechanics of Materials and Structures, Volume 4*, T. Proulx, Editor. 2013, Springer New York. p. 291-298.
61. Orteu, J.-J., *3-D computer vision in experimental mechanics*. *Optics and Lasers in Engineering*, 2009. **47**(3-4): p. 282-291.

62. Dost, M., et al., *Cross correlation algorithms in digitized video images for object identification, movement evaluation and deformation analysis*. Proceedings of SPIE, 2003. **5048**.
63. Vogel, D., et al., *Deformation of Packaging Materials Properties Utilizing Image Correlation Techniques*. J. of Electronic Packaging, 2002. **124**: p. 345-351.
64. Chemnitzer Werkstoffmechanik, G., *VEDDAC 6.0, User Manual*. 2012: Chemnitz, Germany.
65. Herbst, C., Splitthof, K., *Q400 Application Note*. www.dantec-dynamics.com.
66. Becker, T., Splitthof, K., Siebert, T., Kletting, P. *Error Estimations of 3D Digital Image Correlation Measurements*. in *The International Conference Speckle06 "Speckles, From Grains to Flowers"* 2006. Nimes, France.
67. Dudescu, M., Botean, A., Hărdău, M. *E-modulus measurement of wood beams using digital image correlation principle*. in *Proceedings of the 12th International Symposium of Experimental Analysis and Testing of Materials*. 2008. Galați, Romania.
68. Dudescu, C., et al., *Aspects related direct application of strain gages on wood*. Annals of Daaam For 2009 & Proceedings of the 20th International Daaam Symposium. Vol. 20. 2009. 39-40.
69. Dudescu, M., Botean, A.I., *Deformations measurement using digital image correlation principle*. Acta Technica Napocensis, 2007. **50**: p. 21-24.
70. Dudescu, M., Botean, A., Hărdău, M. *Digital image correlation method applied to material testing*. in *26th Danubia-Adria Symposium on Advances in Experimental Mechanics*. 2009. Leoben, Austria.
71. Dudescu, M., Botean, A., Hărdău, M. *Applications of 3D digital image correlation in experimental mechanics*. in *Dantec Dynamics 15th International Conference and User Meeting*. 2008. Schloss Großlaupheim, Ulm, Germany.
72. Dudescu, C., et al., *Measurement of thermoplastics tensile proprieties using digital image correlation*. 2014. p. 33-36.
73. Parsons, E., Boyce, M.C., Parks, D.M., *An experimental investigation of the large-strain tensile behavior of neat and rubber-toughened polycarbonate*. Polymer 2004. **45**: p. 2665-2684.
74. De Almeida, O., Lagattu, F., Brillaud, J., *Analysis by a 3D DIC technique of volumetric deformation gradients: application to polypropylene/EPR/talc composites*. Composites Part A, 2008. **39**: p. 1210-1217.
75. Grytten, F., Daiyan, H., Polanco-Loria, M., Dumoulin, S., *Use of digital image correlation to measure large-strain tensile proprieties of ductile thermoplastics*. Polymer Testing. **28** p. 653-660.
76. Jarabek, M., Major, Z., Lang, R.W., *Strain determination of polymeric materials using digital image correlation*. Polymer Testing, 2010. **29**: p. 407-416.
77. Fang, Q.-Z., et al., *Rate-dependent large deformation behavior of PC/ABS*. Polymer, 2009. **50**: p. 296-304.
78. Vishay, *Measurement of thermal-expansion characteristics of metals using strain gauges. Technical note tn-513-1*, V. Inc., Editor. 2007, www.vishaymg.com.
79. Henz, S.R., Wiggins, J.S., *Uniaxial compression analysis of glassy polymer networks using digital image correlation*. Polymer Testing, 2010. **29**: p. 925-932.
80. Bing, P., Hui-min, X., Tao, H., Asundi, A., *Measurement of coefficient of thermal expansion of films using digital image correlation method*. Polymer Testing, 2009. **28**: p. 75-83.

81. Hammacher, J., et al. *Correlation based local measurement of small CTE for high temperature power electronics packaging*. in *Semiconductor Conference Dresden (SCD), 2011*. 2011. IEEE.
82. De Strycker, M., Schueremans, L., Van Paepegem, W., Debruyne, D., *Measuring the thermal expansion coefficient of tubular steel specimen with image correlation techniques*. *Optics and Lasers in Engineering*, 2010 **48**: p. 978-986.
83. Pan, B., Wu, D., Gao, Z., *A non-contact high-temperature deformation measuring system based on digital image correlation technique*. *Hangkong Xuebao / Acta Aeronautica et Astronautica Sinica*, 2010. **31**(10): p. 1960-1967.
84. Grant, B.M.B., Stone, H.J., Withers, P.J., Preuss, M., *High-temperature strain field measurement using digital image correlation*. *Journal of Strain Analysis for Engineering Design*, 2009. **44**(4): p. 263-271.
85. Dudescu, C., Botean, A., Hardau, M., *Thermal expansion coefficient determination of polymeric materials using digital image correlation*. *Materiale Plastice*, 2013. **50**(1): p. 55-59.
86. Fayolle, X., Calloch, S., Hild, F., *Controlling testing machines with digital image correlation*. *Experimental Techniques*, 2007. **31**(3): p. 57-63.
87. Tung S-H, S.M.-H., Kuo J-C., *Application of digital image correlation for anisotropic plastic deformation during tension testing*. *Optics and Lasers in Engineering*, 2010. **48**(5): p. 636-641.
88. Siebert, T., Becker, T., Spiltthof, K., Neumann, I., Krupka, R., *Error estimations in digital image correlation technique*. *Applied Mechanics and Materials*, 2007. **7-8**: p. 265-270.
89. Pan, B., Xie, H., Wang, K., Qian, K., Wang, Z., *Study on subset size selection in digital image correlation for speckle patterns*. *Opt. Express*, 2008. **16**: p. 7037-7048.
90. Wilson, A.J.C., *The thermal expansion of aluminum from 0° to 650° C*. *Proc. Phys. Soc.*, 1941. **53**: p. 235.
91. Chiorean, R., Dudescu, C., Pustan, M., Hardau, M., *Deflection determination of V-beam thermal sensors using Digital Image Correlation*. *Key Engineering Materials*, 2014. **601**: p. 41-44.
92. Chiorean, R.D., M. C.; Pustan, M.; Hărdău M. , *V-Beam Thermal Actuator's Performance Analysis Using Digital Image Correlation*. *Applied Mechanics and Materials*, 2014. **658**: p. 173-176.
93. Zhang, Y. and K. Wang, *Application of Labview and MATLAB in ESPI image processing*. *Laser Technology*, 2009. **33**(6): p. 582-585.
94. Gao, W. and Q. Kema, *Parallel computing in experimental mechanics and optical measurement: a review*. *Optics and Lasers in Engineering*, 2012. **50**(4): p. 608-617.
95. Dudescu, M., *Matlab Scientific Toolbox for Strain-Stress Analysis*. *Acta Technica Napocensis*, 2004. **47**: p. 31-40.
96. Etemeyer, A.G., *ISTRA MicroStar v.2.6*, in *User Manual*. 2000, Etemeyer AG.
97. Dudescu, M., *Post-processing of experimental data using Matlab*, in *International Workshop "Advanced Researches in Computational Mechanics and Virtual Engineering"*. 2006: Braşov, Romania.
98. Dudescu, M., Păstrav, I. *Full-field processing of experimental data using MATLAB*. in *Al X-lea Simpozion internațional de analiză experimentală a tensiunilor și încercarea materialelor*. 2004. Sibiu, România.
99. Gere, J.M. and S.P. Timoshenko, *Mechanics of Materials, 2nd ed*. 1984, CA: Brooks/Cole Monterey.